A numerical investigation into Southern Ocean sea ice using CICE version 4.0

by

Roger P. Stevens
Master of Philosophy
Bachelor of Engineering

Submitted in fulfilment of the requirements for the Degree of

Doctor of Philosophy in Quantitative Marine Science
(A joint CSIRO and UTAS PhD program in quantitative marine science)

University of Tasmania

October, 2013

Declarations

I hereby declare that this thesis contains no material which has been accepted for the award of any other degree or diploma in any tertiary institution, and to the best of my knowledge contains no copy or paraphrase of material previously published or written by any other person, except where due reference is made in the text of the thesis.

Signed: .....
Roger P. Stevens

Date: .....

Authority of access

This thesis may be available for loan and limited copying in accordance with the *Copyright Act* 1968.

Signed: .....
Roger P. Stevens

Date: .....

Acknowledgements

I would like to thank:

My wife Stella. This PhD was one of her many good ideas. She not only put up with my sea ice obsession but supported me in every way during my candidature. Thank you for enabling the best years of my working life, so far.

My supervisors Petra Heil, Kelvin Michael, and Steve Rintoul. Particular thanks go to Petra, who was so generous with her time and full of useful suggestions. Thank you for providing a rich and rewarding student experience.

The Los Alamos National Laboratory for developing CICE4 and making it available.

Neil Adams for supplying the grid, the land mask, and the atmospheric forcing data and for his help in reprocessing and understanding this data.

Simon Marsland for supplying the ocean forcing and for his suggestions concerning model configuration.

National Computing Infrastructure (NCI) for hosting my computations and for help with using their systems. This research was undertaken with the assistance of resources provided at the NCI through the National Computational Merit Allocation Scheme supported by the Australian Government.

Joe Comiso for passive microwave-derived ice concentration data.

National Centers for Environmental Prediction (NCEP) for reanalysis air temperature and wind speed.

National Aeronautics and Space Administration (NASA) for the figure of Antarctica.

My son David O'Donohue and also Simon Wotherspoon for their assistance with statistics.

Also my daughter Kate Stevens, who, when she was only six, created one of the section headings.

This thesis is dedicated to the memory of the late Dr Neil Adams, whose very premature demise has been a great loss to the Antarctic science community.

Abstract

Numerical simulations of Southern Ocean sea ice were conducted using the Los Alamos numerical sea ice model CICE version 4 (CICE4) which was configured in stand-alone mode on a moderately high-resolution Southern Ocean grid. The atmospheric forcing was derived from the hemispheric forecasting model Polar Limited Area Prediction Systems and ocean forcing from the global ocean general circulation model Australian Climate Ocean Model. An eleven-year simulation was carried out for the interval from 1998 to 2008. Results show that the meridional position of the sea ice edge follows an annual cycle of northward (southward) movement during ice growth (decay). This cycle is largely driven by thermodynamics but ice advection also contributes. Once a mature winter ice pack has formed, ice advection exceeds thermodynamic expansion in providing impetus for northward ice edge movement, most prominently in regions such as north of Prydz Bay and the western Weddell Sea. These zones are characterized by persistent southerly winds. With progressing seasons there is an increase in the size and number of longitudinal zones where ice advection out-paces the thermodynamic advance of the ice edge. This is caused by a slowing in the thermodynamically-driven expansion, while ice advection remains fairly constant over monthly intervals. Eventually there is a time interval when the zonal average northward ice velocity is greater than the zonal average northward expansion of the ice edge and so ice advection is dominant in determining the ice edge position. This is not sustainable due to a lack of thermodynamic growth in austral spring, consequently the ice retreats poleward. We examined the relationship between total ice area and total ice volume. There exists a correlation which is best in February. This correlation deteriorates as the year progresses so that July fails at 90% confidence. During November and December the correlation becomes significant at 95% confidence level. Simulations were also conducted using forcing adjusted by amounts that are compatible with the A1B scenario for IPCC Fourth Assessment Report projected changes in climate for the year 2100. These simulations showed a dramatic reduction in summer total ice area (to about 2% of the control simulation) and total ice volume (to about 5% of the control simulation) but a less dramatic reduction from April to October (to about 80% for total ice area and about 70% for total ice volume compared to the control simulation). In summer most ice was confined to the southern Weddell Sea and to the up-stream sides of the East Antarctic coastal protrusions, especially the fast ice over the Ninnis Bank. Even in climates warmer than that of the A1B projections ice remained east of the Ninnis Bank because the large thickness of ice here does not have time to melt before freezing conditions return. Whether fast ice over the Bank could remain trapped by the many grounded icebergs is such a warm climate is uncertain.

Contents

List of Figures

List of Tables

1. Introduction and Background

1.1 Introduction

Sea ice is subject to dynamic and thermodynamic processes, driven by atmospheric and oceanic forcing and thus may be an indicator of climate change (Lei et al., 2012). It has been proposed that the Earth has left the Holocene and entered a new geologic epoch, the Anthropocene. This new epoch is characterised by climate change due to human activity (Steffen et al., 2007). In order to demonstrate that change is occurring it is necessary to identify which parameters are changing and have methods developed by which they can be measured. Only then can other indicators of climate change be integrated to infer the consequences of climate change on local and global systems. In the northern hemisphere, warming has seen dramatic reductions in sea ice area (Stroeve et al., 2007) and thickness (Rothrock et al., 1999). However, in the southern hemisphere, the signal is less clear. Satellite-based observations have shown that Southern Ocean sea ice extent has actually increased slightly since the 1970s (Zwally et al., 2002; Curran et al., 2003). Estimates of changes in thickness of Southern Ocean sea ice are sparse compared to that of Arctic Ocean sea ice. Therefore, numerical models are likely to increase our understanding of the physical processes driving sea ice mass balance, and help fill gaps where observations are sparse. The research presented here uses the Los Alamos Community Ice CodE version 4 model (CICE4) (Hunke and Lipscomb, 2008) to investigate the physical processes of Southern Ocean sea ice.

1.2 Antarctica

Antarctica was part of the supercontinent Gondwana, along with South America, Africa, India, Australia and New Zealand. About 183 million years ago Gondwana began to break up, and about 40 million years ago Australia separated from Antarctica. Drake Passage opened between South America and the Antarctic Peninsula about 23 million years ago, allowing strong circulation of the ACC to become established, which isolated waters around Antarctica from the warmer waters further north (Stewart, 1990). Antarctica is a large continent of about 13,200,000 km^2 (Nybakken et al., 2003) with a roughly circular shape, two large embayments, the Weddell and Ross seas, and the Antarctic Peninsula extending north towards South America (Fig. 1.1). The South Geographic Pole is situated near the centre of the continent. Most of the land area is covered by a thick ice sheet with an average thickness of ≈2,000 m and a maximum thickness of ≈4,000 m (Nybakken et al., 2003). Even though the great weight of the ice sheet depresses the land by an estimated 370 to 490 m, Antarctica is the highest continent on Earth with an average height of about 2,300 m (Nybakken et al., 2003). The combination of Antarctica's isolation from warm subtropical waters, its polar location with low incident

radiation, its large land area and its height means that Antarctica is very cold. The record for the lowest land surface temperature of -89.2° C was recorded at Vostok Station on 21.07.1983.

The continental interior has very low precipitation which mostly falls as ice. Ice has accumulated to a great depth forming an ice sheet, which flows under gravity towards the coast. Nearer the coast the flow of ice forms into glaciers which can extend into the ocean as floating ice shelves and ice tongues (Rignot and Jacobs, 2002). Ice shelves and ice tongues interact with sea ice in a number of ways. Ice tongues intercept sea ice moving in the Coastal Current (Massom et al., 2003). Thick sea ice forms on the upstream (eastern) side of the glacial ice tongues through dynamic ice growth processes in the convergent conditions encountered there. On the down-stream side the sea ice is thin because the ice that is advected out is not replaced by up-stream sea ice but must be grown thermodynamically so forming a latent heat polynya (Massom et al., 2003). The glacial valleys concentrate the katabatic winds from the higher continent (Adams, 2004) and once unconstrained over the sea ice the winds gain a westward component due to the Coriolis effect. These strong winds quickly remove ice formed within the polynya (Adolphs and Wendler, 1995) exposing the ocean to the cold atmosphere and fostering sustained high rates of ice production (Tamura et al., 2008). Polynyas often form near ice shelves for similar reasons. At times continental ice from ice sheets and ice tongues detaches to become icebergs. These are likely to ground in shallow waters and to provide stable anchor points for the formation of land-fast ice. The iceberg/fast ice system also blocks the westward movement of pack ice along the coast and allows the formation of a polynya to the leeward side of the system.

The Antarctic continent is also a source of fresh water to the Southern Ocean. Under the ice sheet there is a fresh water drainage system which eventually discharges to the ocean (Stearns et al., 2008). But there are other sources of fresh water from the Antarctic Continent. Ice shelves melt particularly rapidly near their grounding line (Rignot and Jacobs, 2002). Some of this melt is re-frozen under the shelf itself (Oerter et al., 1992), but some is discharged as freshwater into the surrounding ocean. Adding fresh water lowers the salinity of the ocean and lower salinity in surface waters promotes sea ice growth by raising the temperature at which the ocean freezes. Sea ice production increases the rate of melting of ice shelves at their grounding line (Rignot and Jacobs, 2002). Cold, high salinity water produced under growing sea ice can sink to the depth of the grounding line where it is the source of sensible heat to the ice shelf due to change in freezing temperature caused by higher pressure at depth (Joughin and Alley, 2011).

1.3 The Southern Ocean

The Southern Ocean is the most southerly of Earth's oceans and extends across all longitude bands. The northern limits can be defined in different ways but a practical oceanographic definition is from the Antarctic Coast to the Antarctic Convergence at about 50-55 °S (Nybakken et al., 2003). The Southern Ocean connects the Earth's oceans and allows the so-called "ocean conveyer belt" to operate in all the major oceans other than the Arctic Ocean. The Southern Ocean includes the Antarctic Circumpolar Current (ACC) and contains a number of seas including the Weddell Sea, King Haakon VII Sea, Cosmonaut Sea, Dumont D'Urville Sea, Ross Sea, Amundsen Sea, and Bellingshausen Sea. The Southern Ocean is not landlocked to the north as the Arctic Ocean is to its south, so Antarctic sea ice is less constrained in

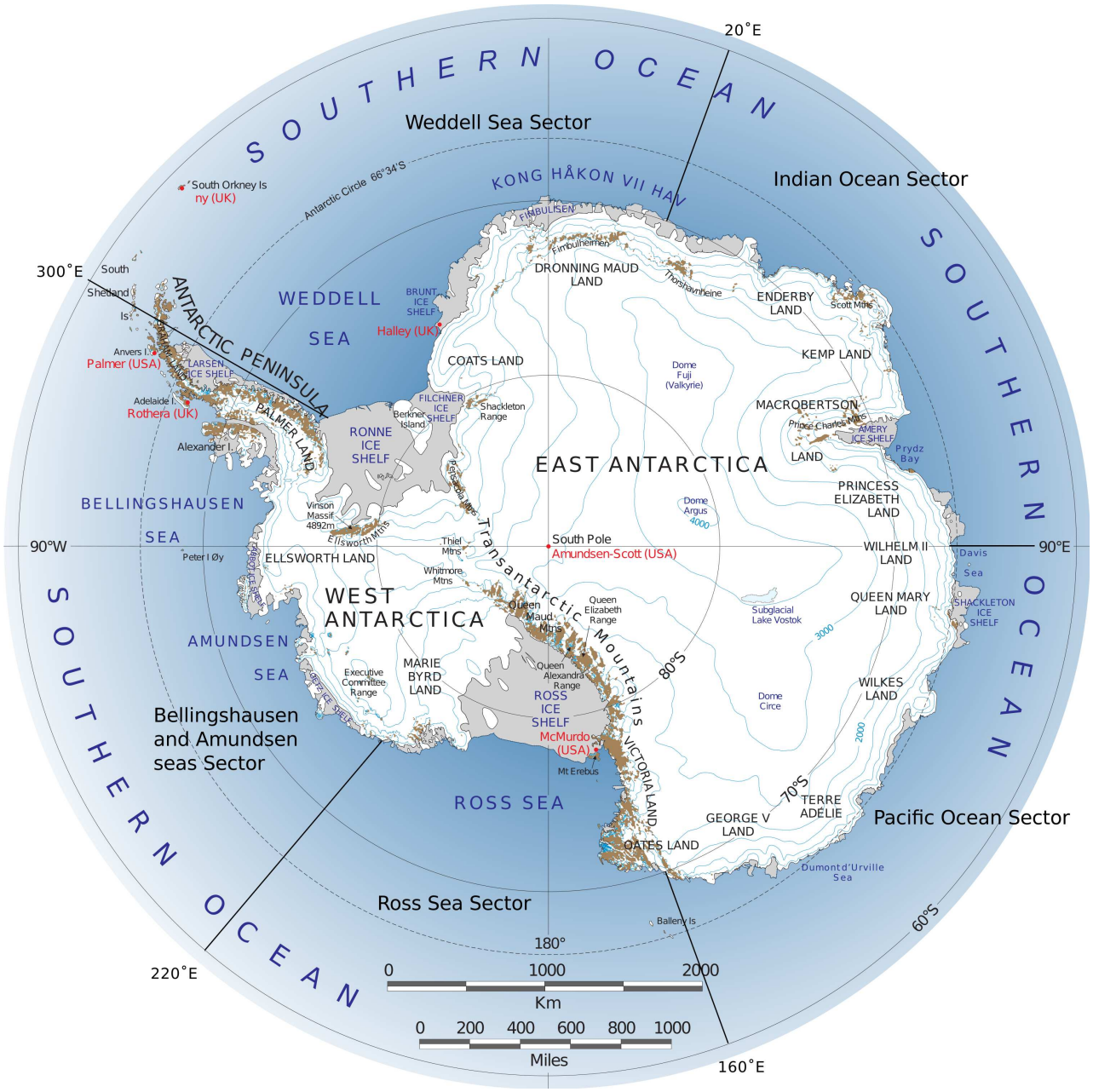

Figure 1.1: Antarctic continent with major features named. Following Zwally *et al.* (1983) we have divided the Antarctic sea ice zone into the following sectors: Weddell Sea (60 °W – 20 °E), Indian Ocean (20 ° – 90 °E), Pacific Ocean (90 ° – 160 °E), Ross Sea (160 ° – 220 °E), Bellinghausen and Amundsen seas (220 ° – 300 °E). Figure modified from NASA.

its movement. In the northern hemisphere, the Arctic Ocean extends to the Pole, but the Southern Ocean reaches no further south than 77 °S.

The Southern Ocean surface water temperatures are low, ranging from the ocean freezing temperature (about -1.8 °C) to about 10 °C . The surface winds that occur in this region are, on average, the strongest to be found anywhere on Earth. Near sea ice maximum, the winds near the ice edge predominantly travel from west to east and drive the ACC in the same direction. While it is not a particularly fast current, i.e. 0.03 to 0.09 m sec^{-1} (Nybakken et al., 2003) it is wide and extends to great depth so the volume of transported water is large, i.e. 137 Sv ($\pm$8) (Rintoul, 2009).

The Southern Ocean contains three continuous, circumpolar fronts. From north to south they are the Subantarctic Front (SAF), the Polar Front (PF), and the Southern ACC Front (Orsi et al., 1995). Near the Antarctic Coast the Coastal Current moves from east to west, driven by easterly winds formed from very cold air that flows off the Antarctic Continent then turns to the west under the influence of the Coriolis effect. Between the Coastal Current and the ACC is a region of upwelling Circumpolar Deep Water (CDW) known as the Antarctic Divergence (AD). Compared to the surface water, the CDW is warm and saline. The surface water, Antarctic Surface Water (AASW), extends with fairly uniform properties from the Antarctic Continent to the Polar Front, and is the water mass which interacts most with sea ice. Near the Antarctic Coast the sea ice moves westward with the prevailing currents and winds. A little further north, sea ice often has a northward component to its trajectory enabling it to cross the AD and turn to the east as it becomes entrained into the ACC and exposed to westerly winds. The AD is not a continuous band within the Southern Ocean. Instead, it is disjointed where large gyres extend far north to connect into the ACC. The largest of these gyres are found in the Weddell and Ross seas. Sea ice within these gyres may advect south in the eastern arm of the gyre and return to travel westward in the Coastal Current. There are smaller gyres as well, for instance in Prydz Bay (centred on 75 °E), one in the Indian Ocean sector centred on 40 °E, and another in the Pacific Ocean sector centred on 110 °E.

It is common to subdivide the Southern Ocean into five regions (Zwally et al., 1983) (Fig. 1.1). Sea ice trends may differ in different regions. For instance, the Ross Sea sector has experienced an increase in sea ice area and extent over the past 30 years (Comiso et al., 2011). In the Bellingshausen and Amundsen seas sector the trends are the opposite where sea ice area and extent have declined since the 1970s (Jacobs and Comiso, 1997).

1.4 Sea Ice

Sea ice is an important component of the climate system of the Earth. While most sea ice is frozen ocean water, some sea ice forms by metamorphoses of overlying snow and some forms from other sources. Water ice is an unusual solid in that it is less dense in its solid phase than in its liquid phase. This means that ice formed within the water column will rise towards the surface due to buoyancy forces. When ice formed at the surface is pushed below the waterline by ridging or rafting processes, these buoyancy forces will maintain contact between the upper and lower layers, forming a new thicker ice profile. Sea ice therefore forms a layer separating the ocean from the atmosphere. Sea ice is important to climate because it greatly alters the energy and mass fluxes between ocean and atmosphere.

An important feature of sea ice is that it has a very high albedo, i.e. $\approx$0.67 in visible

wavelengths for snow-free first year ice and ≈0.96 if covered by >0.03 m of snow (Brandt et al., 2005). This compares to the ocean which has a very low albedo of ≈0.07 (Brandt et al., 2005; Allison et al., 1993). Once sea ice has formed it reflects back into the atmosphere much of the downward shortwave radiation that would otherwise heat the ocean. This effect tends to maintain the ice cover, i.e. it is a positive feedback. However, ice is a good thermal insulator, especially if covered by dry snow. As the ice grows in thickness, its insulating properties reduce the rate at which ice can grow thermodynamically (Ebert and Curry, 1993).

Sea ice acts as a physical barrier to gas exchange and largely decouples the momentum exchange between ocean and atmosphere (Raphael, 2003). Therefore, the air above sea ice is much drier and colder than air that can interact with the ocean. When moist air moves into the sea ice zone it is likely to form low-level ice cloud, which reduces the amount of shortwave radiation that reaches the sea ice. Atmospheric properties (temperature and humidity) change rapidly over relatively short distances at the ice edge and the instabilities associated with this can promote the formation of cold air mesocyclones (Carleton and Fitch, 1993; McMurdie et al., 1997). These systems subsequently influence the movement of sea ice, and hence the position of the ice edge.

Sea ice exists in many forms. Ice crystals formed within the water column are called frazil ice and they can collect under existing ice or can form a layer of grease ice at an ice-free ocean surface. Grease ice is a mixture of ice crystals and sea water and its physical properties are between those of solid ice and sea water (Smedsrud, 2011). In calm conditions the grease ice fuses into thin sheets of ice called nilas (Allison et al., 1993). If the ocean surface is agitated by waves then the grease ice forms into pancake ice (de la Rosa et al., 2011). Thermodynamic ice growth rates can be large when ice is thin but are slower as thickness increases (Allison, 1979). In the Southern Ocean, ice thicker than ≈0.4 m is usually the result of ridging and rafting of thin ice (Allison and Worby, 1994).

In coastal polynyas, sea ice is constantly being removed to expose open water so polynyas are sites of high frazil ice production (Allison and Worby, 1994; Gow et al., 1987). While the wind is favourable to polynya activity the average ice thickness in the polynya remains low and ice production is high. The Antarctic coastal polynyas are primarily latent heat polynyas with latent heat fluxes of 174 W m^{-2} reported for the Adélie Depression compared to transported sensible heat fluxes of 30 W m^{-2} (Williams and Bindoff, 2003). They are called latent heat polynyas because the latent heat of fusion of water to ice largely balances the heat flux from ocean to atmosphere (Adolphs and Wendler, 1995).

While ocean waves can influence how sea ice forms and the distribution of floe sizes, sea ice also affects waves. Shortwave ocean waves are quickly attenuated during their interactions with the ice floes and do not penetrate past the marginal ice zone (Vaughan et al., 2009; Kohout and Meylan, 2008). Longwave ocean waves, on the other hand, can penetrate deep into the pack ice where they can cause large floes to break (Bennetts et al., 2010).

Early in the ice growth season, the ocean is stratified with relatively cold, fresh, surface shelf water overlying warmer, more saline Circumpolar Deep Water (CDW). In the process of ice crystal formation the salt in the ocean water is expelled, forming a network of brine pockets in the sea ice, which may connect into brine channels. The formation of interconnecting brine channels is temperature-dependent (Golden, 2001; Golden et al., 2007) with cold ice (<-5 °C) being impermeable due to a lack of interconnections. Brine rejected during ice growth is colder and more saline than the water below, and therefore of higher density so it sinks. The sinking brine increases the depth of the mixed layer. When the relatively warm, deeper water

is incorporated into the surface mixed layer, any heat it contains can come into contact with the sea ice above. This may slow ice growth (Allison, 1979). On the other hand, ice growth may continue in shallow waters near the coast, where the full water column may be cooled to freezing point, especially in the high ice production regions of the coastal polynyas. High salinity shelf water from these regions spills over the shelf break, entraining the overlying Lower CDW as it sinks, becoming Antarctic Bottom Water (AABW). AABW ventilates the deep ocean and is an important driver of the meridional overturning circulation (Orsi et al., 1999).

Sea ice is also biologically important. On the small scale, plankton may become incorporated into sea ice as it freezes, and live in the brine channels. The rafting process will often introduce ocean water with its plankton into the layer separating the ice layers. Plankton may also be carried into the interface between the ice and the snow during flooding, for example, due to snow loading. Plankton becomes biologically active in spring and is released into the surface layer of the ocean as the sea ice first becomes porous and then melts. The plankton finds itself in optimal conditions for growth and multiplication due to the long hours of sunlight, surface water stratification (Williams et al., 2011a) and the injection of micronutrients such as iron that have accumulated on the sea ice (Lannuzel et al., 2008). The plankton bloom that follows the retreating ice edge supplies food for primary consumers such as krill that can swarm in their millions. Krill, in turn, are food for many predators including fish, squid, penguins, seals, and baleen whales.

The Weddell seal's life history is tied to fast ice and during the height of the last interglacial its distribution was reduced to the deep embayments, where sea ice survived (Younger, 2010). Similarly, Emperor Penguins breed on fast ice and depend on it surviving until the chicks have fledged. So in years when the fast ice breaks-up early, which can be associated with a reduced sea ice barrier, breeding success is low (Massom et al., 2009). Other penguins such as the Adélie breed on land but feed in sea ice and their breeding success depends on having sea ice near to their breeding colonies. There appears to be an optimum amount of sea ice for successful breeding of Adélie penguins but the relationship is complex with important factors being the timing of the occurrence of sea ice and the type of sea ice. For instance, if the penguins have to cross a large distance of land fast sea ice to feed when they are in the "guard phase" of the breeding cycle then breeding success is low (Emmerson and Southwell, 2008). During the last 26 years there has been a decrease in sea ice extent west of the Antarctic Peninsula and Adélie and chinstrap penguins on the South Orkney Islands have suffered reductions in numbers while less ice adapted species like gentoo penguins have increased their population (Forcada et al., 2006).

1.5 The known, the unknown, and contributions of this research

1.5.1 Research questions

This section addresses the research questions examined in this thesis and attempts to relate published research to each topic. It begins with the three research questions, followed by a little background and then proceeds to each question in turn.

1. What is the relationship between variability in sea ice volume and that of sea ice area?

2. In the current climate state, how much do thermodynamic and dynamic processes contribute to the position of the sea ice edge around the Antarctic?

3. High-latitude signature of climate change is strongest in the atmospheric circulation. What changes in Southern Ocean sea ice can be expected from the projections of future climate?

1.5.2 General background

While there are some historical records of Antarctic sea ice (i.e. de la Mare, 1997), the study of Antarctic sea ice has benefitted greatly from the deployment of satellites with passive microwave sensors. Scanning Multichannel Microwave Radiometer, Special Sensor Microwave Imager, Advanced Microwave Scanning Radiometer based observations are available from 1979 onwards. These sensors have been deployed on polar orbiting satellites leaving a polar-centred area about a 2.4 ° wide area void of data. A number of algorithms have been developed to derive sea ice concentrations from measurements of microwave brightness temperatures. Inter-comparisons of the algorithms show that these give slightly different estimates of ice area and extent (Comiso and Parkinson, 2008). Various datasets have been derived from ice concentration including sea ice extent, sea ice area, and sea ice duration (Bjørgo et al., 1997; Parkinson et al., 1999; Cavalieri et al., 2003; Cavalieri and Parkinson, 2008).

The Arctic and Antarctic display very different trends over the interval of satellite-based passive microwave observations. Over the last 33 years, sea ice extent in the Arctic has experienced a dramatic decline of up to -5% per decade, and averaging -3.4% per decade (Comiso and Nishio, 2008). In the Antarctic, sea ice extent has actually increased slightly, at a rate of about +1% per decade (Zwally et al., 2002; Cavalieri and Parkinson, 2008; Comiso and Nishio, 2008). Circum-Antarctic average extent does not tell the full story because it integrates over regions where there have been significant decreases as well as over regions where there have been significant increases. For instance, the Bellingshausen-Amundsen seas sector exhibits a decline of almost 10% in the 20 years after 1979 but the Ross Sea sector had an almost 7% increase in the same period (Zwally et al., 2002).

The increasing trend in sea ice in the Ross Sea and the decreasing trend in the Bellingshausen-Amundsen seas are primarily associated with changes in the Southern Annular Mode (SAM) (Comiso et al., 2011). Annular modes exist in both hemispheres and are large scale patterns of climate variability which exist because of internal atmospheric dynamics in the middle latitudes. They are characterized by latitudinal changes in the position of air masses and in winds at 55–60 ° and 30–35 °. While the mechanism for producing the large-scale atmospheric pressure and wind patterns is well understood the fundamentals of low-frequency variability (annular modes) are still being determined (Jin, 2009). Positive SAM is associated with an increased probability of low sea level pressure in the Bellingshausen-Amundsen seas sector (Stammerjohn et al., 2008). The atmospheric circulation around these low pressure systems produces winds with a northerly component west of the Antarctic Peninsula and a southerly flow over the Ross Sea. Northerly winds bring warm air into the sea ice region, therefore suppressing thermodynamic sea ice production as well as driving sea ice towards the coast. On the other hand, the southerly winds over the Ross Sea bring cold continental air into the sea ice region promoting thermodynamic ice growth and advecting ice north.

In the Arctic, there has been an average thinning of sea ice compounded by the loss of multi-

year ice (Maslanik et al., 2007). The Arctic sea ice appears to become more like that of the Antarctic, where most of it is first-year ice, because less ice survives summer to become second-year ice. There are more measurements of sea ice thickness in the Arctic than in the Antarctic, including estimates obtained from upward-looking sonar on submarines (Tucker III et al., 1998). Falling well short of such a data set, the Southern Ocean sea ice thickness is documented in the ASPeCt database which estimates ice thickness from ship-based visual observations (Worby et al., 2008). Additionally, passive microwave measurements of brightness/temperature can be used to estimate ice thickness in latent heat polynyas for ice thicknesses less than 0.2 m (Tamura et al., 2007). Satellite- or aircraft-based measurements of ice thickness are becoming available (Farrell et al., 2009). Lidar-based systems can be used to measure freeboard and then estimate ice thickness using the Archimedes principle plus some assumptions about ice and snow density and snow loading (Várnai and Cahalan, 2007; Xie et al., 2010; Farrell et al., 2011). Radar has also been used to estimate freeboard (Giles et al., 2008). Such techniques work better in the Arctic where snow thickness is generally low but in the Southern Ocean the higher snow loading makes the estimates less reliable (Kwok, 2010). As a consequence less is known about trends in sea ice thickness in the Southern Ocean. Numerical sea ice models can be used to compute ice thickness in regions or at times when observations are missing or sparse. For example, the Louvain-la-Neuve sea ice model (LIM) has simulated Southern Ocean sea ice on a $2\,^\circ \times 2\,^\circ$ grid (Vancoppenolle et al., 2009). With a view to contributing to a regional sea ice forecasting system, this research uses a higher resolution $0.25\,^\circ \times 0.25\,^\circ$ grid.

1.5.3 Research question 1

"*What is the relationship between variability in sea ice volume and that of sea ice area?*"

Ice area is well established from satellite-based passive microwave measurements since the late 1970's (Comiso and Zwally, 1984). Ice thickness is less well constrained by measurements and therefore ice volume cannot be calculated with the same degree of certainty.

The surface temperature measured in satellite-based passive microwave observations can be used to estimate thin ice (<0.2m) (Tamura et al., 2007). This is very useful for mapping sea ice production in polynyas (Tamura et al., 2008; Tamura and Ohshima, 2011) but is less use in the pack generally where ice thicknesses are mostly greater than 0.2m.

There is also the ship-based estimated of snow and ice thickness (and concentration) in the ASPeCt data set (Worby et al., 2008). While this data set is very useful it is rather sparse in space and time compared to the daily passive microwave estimates of total ice area.

Dynamic ice growth in thickness is very common with rafting of thin ice and ridging of thicker ice (Worby et al., 1996). Dynamic ice thickening causes changes in surface roughness which are also reflected in the roughness of overlying snow, and this can be used to estimate ice thickness (Toyota et al., 2011b).

Recent satellite-based ice thickness estimates from ICESat combined with passive microwave ice area estimates indicate that for the time interval 2003 to 2008 Antarctic sea ice had increased in area but decreased in thickness, producing very small changes in ice volume (Kurtz and Markus, 2012). Modelling studies have shown that switching off ice advection increases ice thickness and decreases ice area (Holland et al., 2001). Given that wind strengths have increased in the Southern Ocean (Böning et al., 2008), it appears possible that Antarctic sea ice has increased in area as a consequence. This does not necessarily mean that there is more ice. The same amount of ice may be spread more thinly.

1.5.4 Research question 2

"In the current climate state, how much do thermodynamic and dynamic processes contribute to the position of the sea ice edge around the Antarctic?"

In the Southern Ocean there is normally a gradient in ice concentration from high values within the pack to zero in the open ocean to the north. This region of rapidly decreasing ice concentration is called the marginal ice zone (MIZ) and is associated with high gradients of environmental variables (Andreas et al., 1984). However, there are anomalous conditions where the ice edge is quite compact (Massom et al., 2008). Defining the ice edge can be done in different ways depending on the needs and the situation. Since passive microwave receivers have been flying in satellites in the late 1970's the conventional definition has been 15% ice concentration because this is close to the limit that these instruments can reliably detect sea ice (Comiso and Zwally, 1984). The accuracy of detecting the ice edge from space varies with season such that the accuracy is good in winter but there are confounding effects in summer which reduce accuracy (Worby and Comiso, 2004). The low ice concentration in the MIZ means that ice-ice interactions are rare and the floes are in a free drift condition (Leppäranta, 2005).

The ice edge advance and retreat correlates with the position of the -2.16 °C surface temperature isotherm (Comiso and Zwally, 1984). During the ice growth season the total ice area increases, with high concentration ice just south of the ice edge. During the ice decay season, ice area is lost by a southward movement of the ice edge plus a decrease in ice concentration within the pack (Comiso and Zwally, 1984). In many zones in spring, thin ice, such as that in coastal polynyas, will melt and form an inner ice edge that moves northward to meet the southward moving ice edge "aice_2008.gif".

For the time interval 1992-2001 there is a strong correlation between the ice drift velocity and the geostrophic wind velocity, i.e. R^2 ≈0.7 in the Weddell and Indian Ocean sectors (maximum 0.9 in the Amundsen Sea), while correlations between the northward expansion rate of the ice edge and the northward ice velocity are lower, i.e. R^2 ≈0.5 in the Weddell Sea sector and R^2 ≈0.4 in the Indian Ocean sector (maximum 0.7 in the Amundsen Sea) (Kimura, 2007). Kimura (2007) also found that, during the ice growth season, there were two distinct relationships for the short-term northward expansion rate of the ice edge to northward ice velocity: one where the ice edge is advancing and another when it was retreating. While advancing the northward expansion rate of the ice edge is greater than the northward ice velocity and while retreating the northward expansion rate of the ice edge is very similar to the northward ice velocity.

In the Weddell Sea the ice edge advances more to the east than to the north (Massom, 1992). In some years of our simulation the initial ice advance from within the Ross Sea towards the Pacific Ocean sector of East Antarctica exhibits an initial westward advancing ice edge. However, in general there is not a strong correlation between the ice edge location (extent) and the strength of the westerly winds north of the Antarctic Divergence, at least for the years 1972-1977 (Streten and Pike, 1980). The ice edge advance work for this research examines the northward component only because this is generally more important for the ice edge advance.

The advance of the ice edge in autumn and winter can be caused by thermodynamic ice growth north of the ice edge or by the advection of ice from the south. In some zones the ice edge advance is completely thermodynamic. For example, at the prime meridian there is a wide ice band south of the ice edge with thermodynamically-grown frazil and pancake ice

(Wadhams et al., 1987). At other zones ice advection determines the location of the ice edge. An extreme example is at 85 °E where wind and currents combine to produce a tongue-like extension of the ice edge (Rintoul et al., 2008).

The location of the ice edge in spring and summer is more difficult to determine from satellites due to higher water content in the atmosphere and because of wet ice and snow during the melt (Worby and Comiso, 2004). Kimura (2007) restricted his analysis to sea ice concentrations between 40-50% and to the months of May to October to define their ice edge. This was necessary to obtain ice motion from satellite observations. The analysis in this research uses a lower range of ice concentrations for calculating ice drift speeds, i.e. 1-30%, but the seasons were limited to middle autumn to early summer (April to December) because of the complexity of the ice edge in many zones from January to March. This research quantifies the thermodynamic and dynamic contributions to the maintenance of the location of the ice edge. This is achieved by comparing the northward expansion rate of the ice edge to the northward ice velocity at the ice edge. This is done at 1 ° intervals around the Southern Ocean and for the months when there is circum-Antarctic sea ice, i.e. April to December.

1.5.5 Research question 3

"*High-latitude signature of climate change is strongest in the atmospheric circulation. What changes in Southern Ocean sea ice can be expected from the projections of future climate?*"

Surface atmospheric temperatures have risen over land and oceans contributing to a global average rise of 0.74 ° in the 100 year time interval 1906 to 2005 with the land warming at about twice the rate of the oceans (0.27 ° decade^{-1} for land and 0.13 ° decade^{-1} for oceans) (Solomon et al., 2007) chapter 3. At high latitudes the changes have been greater due polar amplification such that the Arctic has warmed two to four times faster than the global average (Screen et al., 2012). The southern hemisphere also has a "hot spot" of surface warming in the Antarctic Peninsula even if warming trends over continental Antarctica are in line with the global mean increase (Vaughan et al., 2003).

The warming climate has seen changes in atmospheric circulation (Corti et al., 1999). In mid and high latitudes this is mostly seen in the Annular Mode, which accounts for the largest part of climate variability in these regions (Jones et al., 2009). The Southern Annular Mode (SAM) has tended toward more positive values (Stammerjohn et al., 2008). Positive SAM is associated with lower air pressures over Antarctica and a pole-ward intensification of the westerly winds at about 50 °S latitude (Ho et al., 2011). Positive SAM is associated with warming over the Antarctic Peninsula (Thompson and Solomon, 2002).

The most commonly used and accepted set of greenhouse gas emissions scenarios, known as the SRES emissions scenarios, comes from the IPCC. These were last updated in 2000 in the Special Report on Emissions Scenarios (SRES). They are now named the SRES emissions scenarios (Nakicenovic and Swart, 2000). The SRES emissions scenarios are divided into six families: A1FI, A2, A1B, B2, A1T and B1. The families are based on future technological and societal changes, such as population growth, and not just on a high, medium and low scale of carbon emissions.

The A1 scenario family have storylines of rapid growth in the world's economy and a population peak in the middle of the 21st century. There is rapid introduction of more efficient technologies and building of capacity associated with increased cultural and social interactions and a reduction is the disparity between rich and poor. The A1 scenario family has three

subgroups based technology: A1FI is fossil fuel intensive; A1T focuses on non-fossil energy sources; A1B has balanced set of technologies which does not rely too greatly on any particular energy source. A1B assumes that all the technologies will have similar rates of improvement in supply and end use technologies. The A1B scenario is usedas the basis of calculating adjustments that were applied to existing forcing for warm climate simulations. Economic growh and energy usage do seem to be rising rapidly, there is some evidence of new technologies being introduced but it remains to be seen if a more equitable distribution of weath will eventuate.

Projections for the Southern Ocean from climate model simulations include increases in air temperature, surface air pressure, precipitation, cloud fraction, downward long-wave radiation, air humidity, and wind speeds. The values in the next five paragraphs are taken from the IPCC Fourth Assessment Report chapter 10 (Solomon et al., 2007).

Anthropogenic green house gasses that find their way into the atmosphere cause warming of the troposphere. Estimated global average increase of air temperature by 2100 for the A1B scenario are 1.7–3.4 °C, compared to those of the time interval 1980 to 1999. The oceans are also warming but at a slower rate because they have higher thermal inertia.

Cloud fraction is important in determining the amount of shortwave radiation reaching the surface and in the amount of long-wave radiation prevented from escaping into space. The IPCC models predict an increase of 1-2% in high level cloud fraction in the sea ice zone for the A1B scenario. This reduces the model mean short-wave radiation flux reaching the surface by 0.13 $\pm$0.11 W m^{-2} and increases the long-wave radiation by 3.8 $\pm$0.33 W m^{-2}.

Global average precipitation is projected to increase by more than 3% by 2100 for the A1B scenario. In the Southern Ocean the rate of precipitation is projected to increase by +0.2 mm day^{-1} for this scenario compared to 1980-1999. The global mean precipitation increases in all scenarios because of the increased water-holding capacity of the atmosphere (Douville et al., 2002).

Sea level air pressure is projected to increase over the subtropics and decrease over the higher latitudes. This is associated with an expansion of the Hadley Circulation and a poleward shift in storm tracks. The models consistently show a positive trend in the Southern Annular Mode (SAM). Some models show an increase in cyclones and an intensification in the southern hemisphere westerly winds (Lynch et al., 2006). Associated with the higher frequency of strong storms is an increase in extreme wave height.

Some models produce a poleward shift in the surface westerly winds, accompanied by a southerly movement of the core of the Antarctic Circumpolar Current (Fyfe and Saenko, 2005; Gupta et al., 2009) but in other models the ACC moves very little (Graham et al., 2012). Some models show an increase in the strength of the ACC, associated with the stronger surface westerly winds (Fyfe and Saenko, 2005; Gupta et al., 2009), but in eddy-resolving models stronger winds produce an intensified eddy field rather than an increase in ACC volume transport (Hogg et al., 2007).

Since the 1970s there has been a small but significant increase of 0.97% decade^{-1} in total Southern Ocean sea ice extent (Zwally et al., 2002). This is puzzling when there is a warming climate trend. It has been proposed that the depletion of stratospheric ozone over Antarctica during the 20th century caused an increase in the surface winds in the sea ice zone (Gillett and Thompson, 2003), and this may be responsible for the increase in sea ice extent. However other modelling studies have cast doubt on this idea (Karpechko et al., 2010; Sigmond and Fyfe, 2010).

The thesis is divided into seven chapters:

1. "Introduction" which is this chapter, provides an introduction and overview of Antarctica, the Southern Ocean, and sea ice. It also gives some background to topics relating to the research questions.

2. "Model and Methods" which describes CICE4 and other software developed for this project. This chapter also describes the tuning of the model and the sensitivity of the model to the fields used for tuning.

3. "Forcing" which examines the external forcing used.

4. "Results" which describes the experiments used to address the research questions and the results of these experiments.

5. "Discussion" which discusses the results and how they relate to other published work.

6. "Conclusions" which gathers the main results and states how the research questions were addressed.

7. "Further work" which provides some suggestions for improvements.

2. Model and Methods

2.1 CICE4

2.1.1 Introduction to CICE4

The numerical model CICE4 (Community Ice CodE) was used to investigate the three research questions. CICE4 simulates total ice area and volume which are used in an examination of how area and volume vary for the years 1998 to 2008. CICE4 also simulates ice velocity obtained from the dynamics of the model. The northward component of ice velocity was compared to the northward speed of the ice edge to assess the importance of ice advection in maintaining the position of the ice edge. Finally, predictions can be made about the future of Southern Ocean sea ice by running the model with forcing fields compatible with climate projections for the year 2100.

This section describes CICE4 as it was configured for this research. CICE4 was developed by the Los Alamos National Laboratory as part of the Climate, Ocean and Sea Ice Modeling Project. Many individuals and groups contributed to the model but the principal developers are Elizabeth Hunke and William Lipscomb. CICE4 is written in Fortran90 and can be run on parallel computers using Message-Passing Interface (MPI) as it was for this research. Details on running CICE4 in parallel can be found in Section 2.2. CICE4 can utilize files in NetCDF (Network Common Data Form) for I/O and this is how it was configured for this research. CICE4 is designed to be run coupled to ocean and atmospheric models but can also be run standalone as was done for this research. Our standalone configuration used forcing from the regional atmospheric model Polar Limited Area Prediction Systems (PolarLAPS) and the ocean global ocean model Australian Climate Ocean Model (AusCOM).

2.1.2 Thermodynamic and dynamic processes in CICE4

CICE4 represents sea ice as a thickness distribution. The surface of the ocean is divided into grid cells and each grid cell contains an ice thickness distribution, which has zero thickness for open water. The ice thickness distribution can change by the thermodynamic processes of ice growth and decay or by ice advection and dynamic growth. The equation used to calculate changes in the ice thickness distribution is equation 3 in Thorndike *et al.* (1975):

$$\frac{\partial g}{\partial t} = - \bigtriangledown . (g\mathbf{u}) - \frac{\partial}{\partial h} (fg) + \psi \tag{2.1}$$

where $\mathbf{u}$ is the horizontal velocity, f is the rate of thermodynamic ice growth, ψ is the ridging redistribution function, and g is the ice thickness distribution function. The first term on the right hand side of the equation 2.1 is the horizontal transport of ice. The second is the change in thickness due to thermodynamic growth or melt. The third term is the dynamic ice growth from ridging and rafting.

The right hand elements of equation 2.1 are evaluated in sequence starting with the thermodynamic growth/decay then ice advection by horizontal transport and ending with dynamic growth through ridging. The continuous ice thickness distribution is approximated by ice thickness categories (refer Section 2.4). Each thickness category is treated as a uniform column of thickness $h_{in} = v_{in}/a_{in}$ where v_{in} is the volume of ice in category n and a_{in} is the fractional ice area in this category. Each column is divided into N_i layers, where $N_i = 4$ by default.

The fractional area of all ice categories is given by $a_i = \sum_1^n a_{in}$ and the ice area of each grid cell can be obtained by multiplying the fractional area by the grid cell area. Total ice area is the sum of the area of ice in each grid cell. Similarly, the volume of ice in each grid cell is the sum of the volume of ice in each category and the sum of the volume of all grid cells gives the total ice volume. Total ice area and total ice volume are used for the first research question examining how ice area and volume covary.

Snow is known to have an important influence on sea ice processes. Snow is treated in a similar manner to ice in that the snow thickness is calculated by $h_{sn} = v_{sn}/a_{in}$ where v_{sn} is the snow volume for ice category n. Snow can have multiple layers N_s, but the model default is $N_s = 1$. Snow is not created within CICE4 as ice is but is supplied externally to the model as precipitation forcing.

CICE4 calculates the grid scale ice velocities and moves ice from one grid cell to an adjacent one by a process of incremental remapping in 2-dimensional horizontal space (Dukowicz and Baumgardner, 2000). The ice is then re-arranged within the ice thickness distribution of each grid cell by another process of incremental remapping within thickness space (Lipscomb, 2001). These processes preserve ice volume and other state variables such as snow volume, internal ice and snow energy, surface temperature, and volume-weighted mean ice age. It is the ice velocity $\mathbf{u}$ that is used to investigate research question two into the contribution of ice dynamics in the form of advection to the maintenance of the position of the ice edge.

Growth or decay at the ice-ocean interface and decay at the ice-snow-atmosphere interface is determined by the energy balance at these surfaces (Maykut and Untersteiner, 1971). Energy fluxes at the top surface are long-wave radiation down from the atmosphere and clouds, short-wave radiation down, reflected short-wave radiation up, long-wave radiation up from thermal emission, sensible and latent heat exchange with the surface atmosphere, heat conduction within the ice and snow, and penetrating radiation which is absorbed within the ice and snow (Maykut and Untersteiner, 1971). Below the freezing point of fresh water the energy balance of the top surface is maintained by changes to the surface temperature and hence the upward long-wave radiation flux. At the freezing point of fresh water it is the latent heat of melting that balances excess energy fluxes into the ice. Moisture from the air can condense onto the top surface but most mass is added to the top via snow fall. Precipitation falling as rain is assumed to run-off quickly into the ocean.

At the ice-ocean interface there are only two fluxes: the heat flux from the ocean to the ice and the heat conducted through the ice. Ice grows at the ice-ocean interface if the heat flux conducted towards the upper surface is larger than the ocean heat flux. Conversely, basal melt will occur if less heat is conducted upward into the ice than arrives from the ocean. Under ice

growth or melt conditions the heat balance at the bottom surface is maintained by the latent heat of fusion. The heat conduction into the submerged sides of the floe can cause lateral melt. Arctic lateral melt rates have been estimated using the difference between sea surface temperature and the temperature of ice at the bottom of the floe Maykut and Perovich (1987) equation 12 :

$$M_r = m_1 \triangle {T_w}^{m_2} \tag{2.2}$$

where $m_1 = 1.6 \times 10^{-6}$ m s^{-1} °C$^{-1.36}$, and $m_2 = 1.36$. Lateral melt rate can be combined with floe diameter to give the fraction of ice that melts laterally (Steele, 1992):

$$rside = \frac{M_r * dt * \pi}{\alpha * \phi_{floe}} \tag{2.3}$$

where α is a constant which for the Arctic Ocean has a value 0.66 (Rothrock and Thorndike, 1984), and $\phi_{floe} = 300$ m is the average floe diameter.

CICE4 models sea ice as a plastic medium which reacts to low stresses like a nonlinear viscous compressible fluid. The rheology that describes this behaviour is called viscous-plastic (Hibler III, 1979). CICE4 uses a modification of this rheology called elastic-viscous-plastic rheology (Hunke and Dukowicz, 1997). At time scales associated with wind forcing the elastic-viscous-plastic rheology reduces to the viscous-plastic rheology but at shorter time scales the adjustment process is via the computationally more efficient mechanism of elastic waves.

The internal ice stress tensor can be obtained from the viscous-plastic constitutive law, which relates ice stress to strain rate. Internal ice stress is used in the two dimensional momentum equation (Hibler III, 1979):

$$m\frac{\partial \mathbf{u}}{\partial t} = \bigtriangledown.\sigma + \overrightarrow{\tau_a} + \overrightarrow{\tau_w} - \hat{k} \times mf\mathbf{u} - mg \bigtriangledown H_o \tag{2.4}$$

where m is the combined mass per unit area of ice and snow, $\mathbf{u}$ is the horizontal velocity, t is time, σ is internal stress, $\overrightarrow{\tau_a}$ is wind stress, $\overrightarrow{\tau_w}$ is ocean stress, the fourth term on the right is the Coriolis stress, and the fifth term is the stress due to the sea surface slope (where g is the acceleration due to gravity).

A discrete version of the momentum equation is used by the model to calculate ice velocity. The ice velocity is then used to estimate dynamic ice growth in high ice concentration regions of convergence. To ensure that closing of open water is more likely than ridging CICE4 uses a weighting function (Thorndike et al., 1975). The weighting function gives preference for the ridging of thin ice rather than to thick ice. Sufficient ridging will occur so that the ice area in the grid cell does not exceed the area of the grid cell.

2.1.3 Snow-ice in CICE4

Snow-ice production is another ice growth mechanism simulated by CICE4. Snow-ice is created if under freezing conditions the snow loading causes the snow-ice interface to be depressed below

the sea surface. A snow loading sufficient to depress the snow-ice interface to sea surface is obtained when the ratio of snow thickness to ice thickness is equal to the ratio of snow density to ice density. Both snow density and ice density are constants in CICE4 with values $\rho_{snow} = 300$ kg m^3 and $\rho_{ice} = 917$ kg m^3 giving a maximum snow thickness to ice thickness ratio of 0.33. Volume and energy is then transferred from the snow layer to the top ice layer.

2.2 Domain Decomposition and Speedup

2.2.1 Introduction

This section describes the domain decomposition and speed-up experiments. The "panantarctic" domain, containing 330×330 grid cells, can be subdivided into blocks. Each compute processor can work on one or more blocks. For rectangular blocks it is better to have more grid cells in the y-direction (less processors) than the x-direction (more processors). However, with a square grid many of the configuration options have square blocks. The number of processors and the number of blocks is set in the compile scripts. The shape and options for optimization are set in the name list.

2.2.2 Domain Decomposition

In parallel computing a speed-up in the time it takes to complete solving a problem (the elapsed time) is obtained by dividing the problem into discrete "chunks" and distributing these to the computing tasks available. In the case of simulating Southern Ocean sea ice the chunks are parts of the "panantarcitc" domain and are called "blocks". Each block contains grid cells representing land, ocean only, or ocean and sea ice. Making the blocks smaller increases the number of computing tasks that can be applied to solving the problem but it also increases the communications overhead because each block has to communicate its results to its neighbours. Increasing the communications overhead increases the computational resources needed to solve the problem (CPU time). The domain blocks should be chosen to ensure that each computing task has a similar amount of work to do and will finish in about the same time. This is called load balancing. In the case of simulations of Southern Ocean sea ice the aim is to have about the same number of sea ice containing grid cells in each block.

The less the blocks have to communicate with each other the more efficiently the model runs. Square blocks have smaller boundaries for the number of grid cells they contain, compared to thin rectangles for example, and thus minimize communications between blocks. Each block has a set of "ghost cells" around the edge which contain the values from adjacent blocks. MPI maintains the ghost cells with the current values from the adjacent blocks by passing values each time step.

There are two useful ways to decompose the domain and this is done by setting the processor shape:

- slender (slenderX1 or slenderX2)
- square (square-ice)

"slenderX1" divides the domain into thin strips-shaped blocks. On a global grid the long side of the blocks would be latitude (a rectilinear grid) so each has one end in the Arctic

Ocean and the other end in the Southern Ocean. This is not a very useful configuration on the curvilinear "panantarctic" grid because some blocks near the edge will contain only ocean. Other blocks near the middle will contain a lot more land cells than blocks between the edge and the middle of the domain. "slenderX2" is also designed for a rectilinear grid creating two sets of strip like blocks which meet at the equator so each block will have only one end in the Arctic or Southern oceans. "square-ice" divides the domain into blocks of squares and is almost equivalent in computing effort to "slenderX2" when there are 4 equal blocks each running on one processor (Fig. 2.1). Therefore "square-ice" is used in this research.

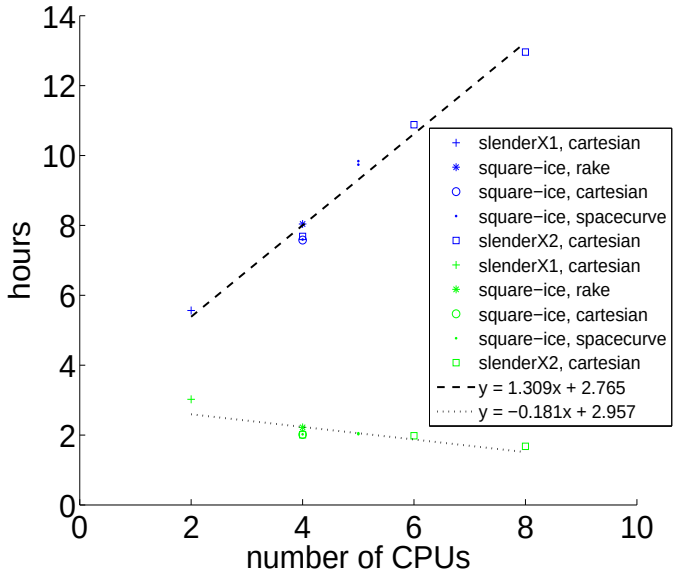

Figure 2.1: Run time as a function of the number of CPUs

2.2.3 Speed-up

In order to determine the optimum configuration for domain decomposition that gives decreased elapsed time while not requiring excessive computing resources, experiments were undertaken with various methods for domain decomposition. The CPU and elapsed time are measured for similar runs with 2, 4, 5, 6 and 8 CPUs. With an increasing number of CPUs, the elapse time (t_{elapse}) decreases at a rate of:

$$t_{elapse} = -0.181x + 2.957 \tag{2.5}$$

However, the CPU time (t_{CPU}) increases at the much faster rate of:

$$t_{CPU} = 1.309x + 2.765 \tag{2.6}$$

where x is the number of CPUs.

The combinations of "square-ice" or "slenderX2" has elapsed times for 4 CPUs that are almost the same as for 5 and 6 CPUs (Fig. 2.1). Thus there is no elapsed time benefit to running with 5 or 6 CPUs.

2.3 Model Spin-up

The model can be started from two states: a) zero ice; or b) 2 m of ice south of 60 °S. For the default ice thickness categories either option was successful. However, for the optimized ice thickness categories (Table 2.1 right hand column) it was better to start from the "zero ice" option. To obtain a stable model condition for the start of experiments beginning in January 1998, the model is run for five years using 1998 forcing. The simulation rapidly converges on a stable value, because very little Antarctic sea ice survives the spring and summer to become second-year ice. So the model almost resets itself every year. The total ice area converges rapidly towards a stable state, i.e. on 31 December the total ice area of cycle 5 is less than 0.002% different from that of cycle 4. Average ice concentration changes by only -0.00005% between cycle 4 and 5. The largest differences in ice concentration are found in the central Weddell Sea, which is one of the locations where ice survives throughout the summer. Average ice thickness changes by 0.17% between cycle 4 and 5. The largest differences in ice thickness are found in the small embayments around the coast.

2.4 Ice Thickness Categories

Experiments are undertaken to determine the optimum set of ice thickness categories. There are two parts to this, the number of categories and the maximum thickness for the categories.

2.4.1 Number of Ice Thickness Categories

In this research five ice thickness categories were used for all runs other than those investigating the impact of ice thickness categories on model performance. Five thickness categories are sufficient to allow patterns of variable thickness to develop. Adding more ice thickness categories generally increased the ice thickness and hence ice volume, but it also increased the computing effort needed to run the model. However, the increase in total ice volume when the number of ice thickness categories is increased from 5 to 7 is small.

The number of ice thickness categories, denoted in CICE4 as "ncat", was varied between 1 and 7. The following simulation fields are examined:

- ice thickness distribution in space
- total ice area
- total ice volume
- model run time

The effect of a low number of ice thickness categories is most noticeable in the ice thickness distribution. For one and two ice thickness categories, the model produces a very even thickness

distribution, lacking regions of extremely thick ice (Fig. 2.3a and 2.3b). For three ice thickness categories, most of the thick ice and thickness features are present but subdued (Fig. 2.3c). For four and five ice thickness categories, the thickness of the thickest ice increases (Fig. 2.3d and 2.4). There is very little change in increasing from five to seven ice thickness categories (Fig. 2.3e and 2.3f), i.e. seven categories increases average ice thickness by 0.01 m compared to five categories, and the maximum difference in ice thickness is 0.8 m thicker. The maximum value is located on the up-stream side of a coastal protrusion. The differences are smaller in the central pack ice, i.e. mostly less than ± 0.2 m.

The number of ice thickness categories has a small effect on total ice area, i.e. increasing from 5 to 7 categories increases the annual average total ice area by 2.7×10^4 km^2 or 0.26%. The increase in total ice area occurred between the middle of November and the end of April, with a peak of 2×10^5 km^2 in early January. For the rest of the year, increasing the number of ice categories decreases the total ice area with a maximum decrease of 2.8×10^4 km^2 in late September.

Progressing from three to seven ice thickness categories produces a small increase in ice volume from 9.51×10^{12} km^3 to 10.18×10^{12} km^3 (Fig. 2.2a). There is a step from two to three categories, i.e. ncat=2 produces an ice volume of 7.80×10^{12} km^3. Increasing ncat from 5 to 7 produces a maximum increase in ice volume in mid November and a minimum increase in mid March with an annual average increase of 1×10^{11} km^3 or 1%. For ncat > 5 there is little improvement in spatial distribution of ice thickness and, in going from 5 to 7 ice thickness categories, there was only a 0.46% increase in total ice volume. Therefore, the model was run with ncat $= 5$ for this research and presented, from this point on, in this thesis.

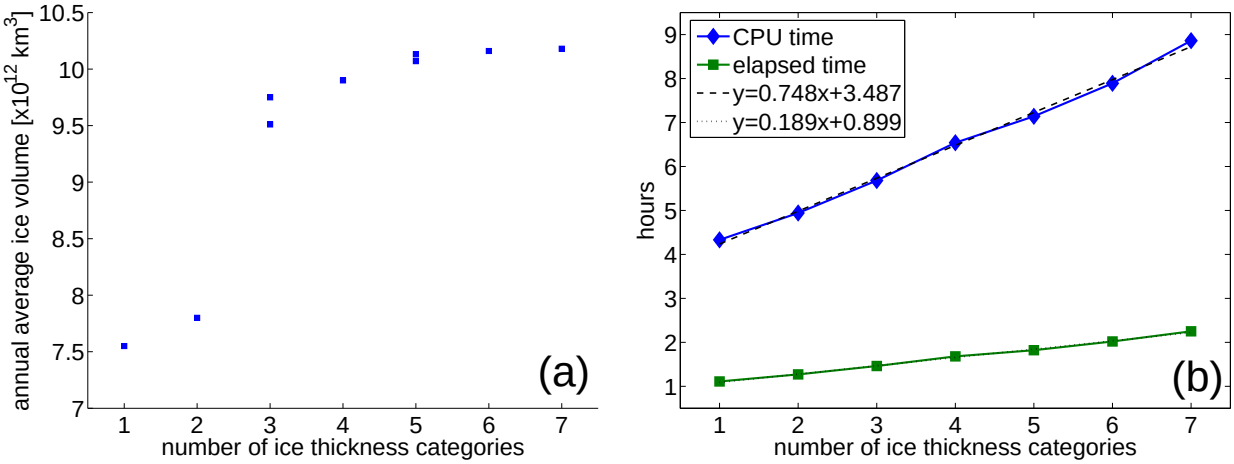

Figure 2.2: Effect of the number of ice thickness categories on: (a) Annual average ice volume vs number of ice thickness categories. For ncat $= 3$ the higher volume is for maximum ice thickness for the highest category of 8 m and maximum thickness of lowest category of 0.125 m while at the lower ice volume these are 2 m and 0.5 m. For ncat $= 5$ the higher ice volume is for highest category maximum ice thickness of 4 m and the maximum thickness of the lowest category is 0.25 m and lower ice volume has 8 m and 0.125 m; (b) Model CPU (green) and elapsed time (dark blue) as a function of number of ice thickness categories.

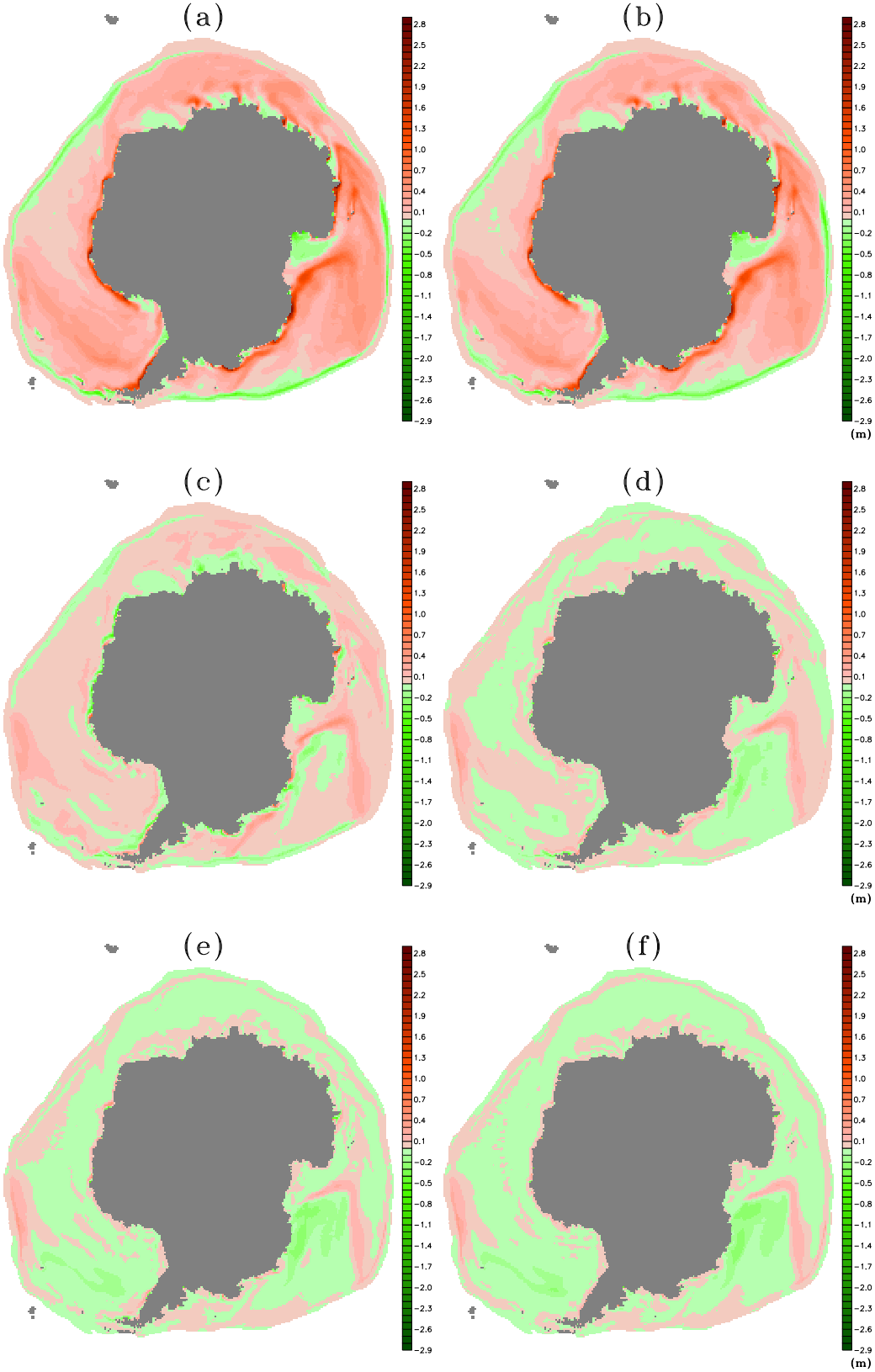

Figure 2.3: Difference in ice thickness between number of categories of 5 and number of categories = 1, 2, 3, 4, 6, and 7 (green shade less thickness and red shade more) on 8 October 1998. All sub-figures use the same scale as shown on the right-hand sub-figures. The land mask is grey.

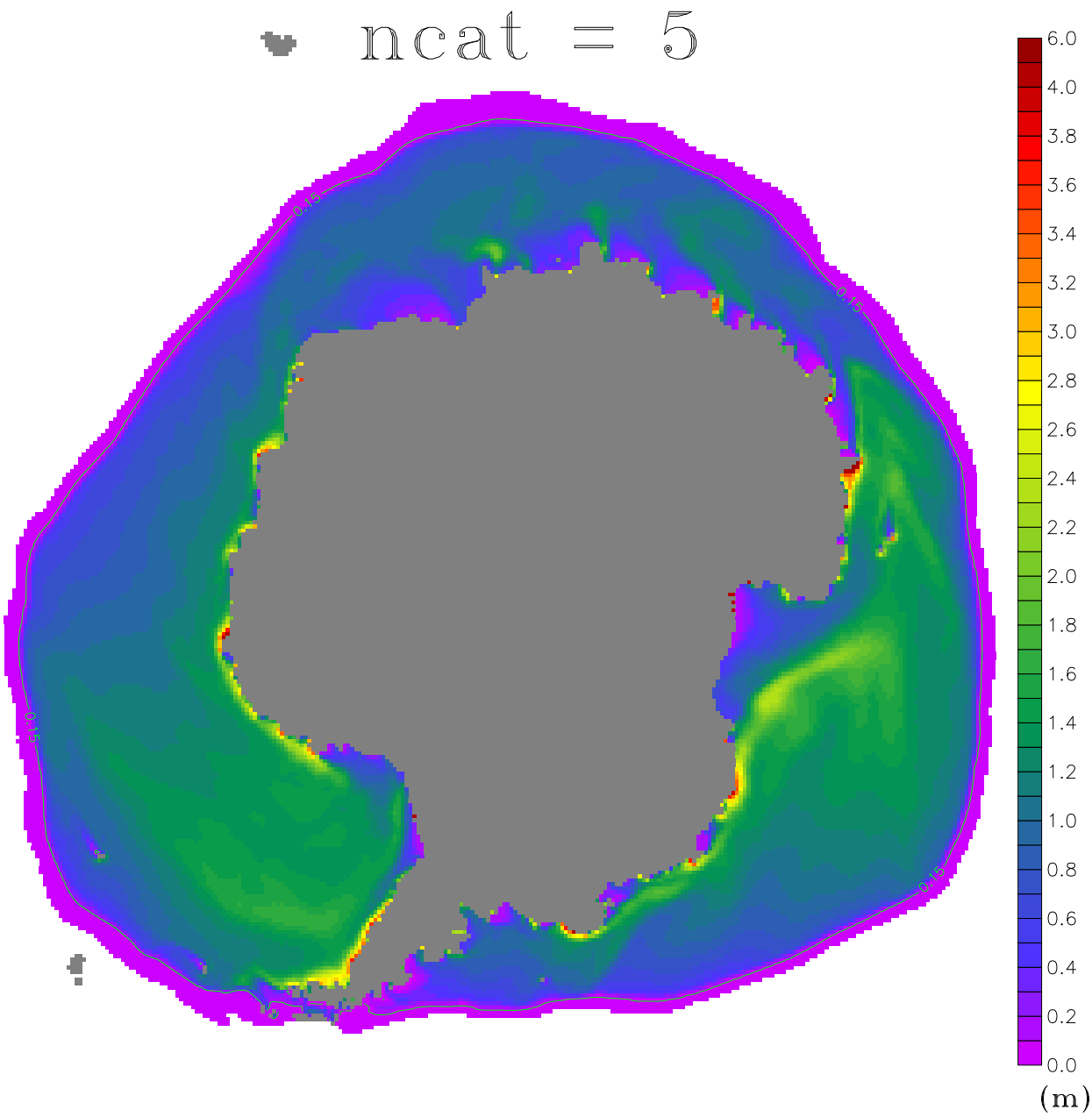

Figure 2.4: Ice thickness on 8 October 1998 for where number of categories = 5. Also shown is the 15% ice concentration contour (green) and land mask (grey). Ice thickness scale is bi-linear with 4–6 m at a lower resolution.

2.4.2 Maximum Thickness of Categories

For this research the maximum thickness of the five ice thickness categories are given in the right-hand column of Table 2.1. The maximum category thicknesses are less than those for the Arctic (left-hand column of Table 2.1) because Southern Ocean sea ice is generally not as thick as that found in the Arctic Ocean. The Arctic Ocean is almost land-locked while the Antarctic is unbounded on the north. Since 90% of the Antarctic ice area is lost in summer, most Antarctic ice is first-year ice. The Antarctic sea ice is generally divergent, with episodes

of convergence associated with weather systems (Heil et al., 1998).

	maximum thickness [m]	
category	default set	modified set
n=0	0.000	0.000
n=1	0.645	0.125
n=2	1.391	0.354
n=3	2.470	1.000
n=4	4.567	2.000
n=5	9.334	6.000

Table 2.1: Maximum thicknesses for the default ice thickness categories and modified to optimize for Antarctic sea ice for this research.

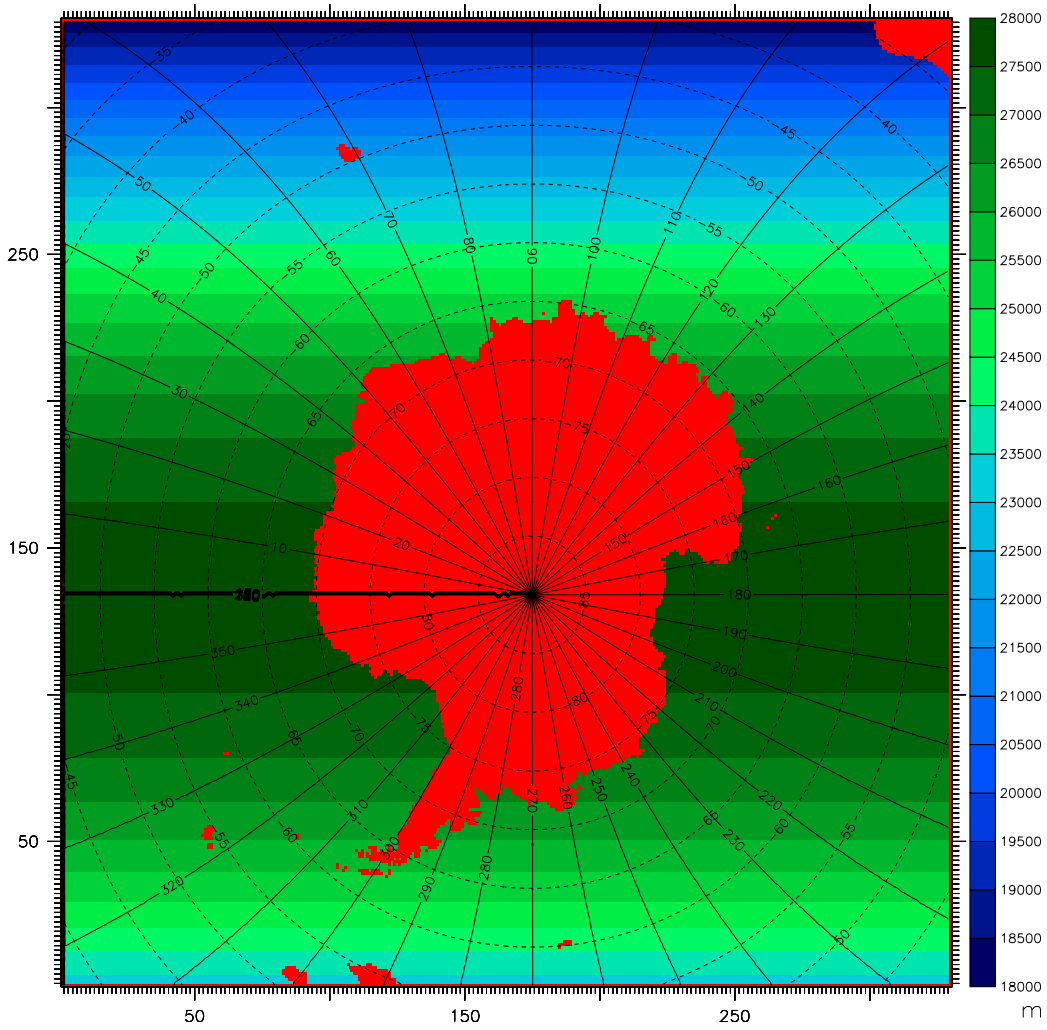

Figure 2.5: The "panantarctic" domain with land mask (red), and key indicates the grid cell dimensions in y-direction. Grid cell x-direction dimensions is 27800 m.

Configuring CICE4 ice thickness categories for the Antarctic involves having thinner maximum thickness for each category. A number of experiments have been undertaken with various maximum category thicknesses. Increasing the maximum thickness of the thinner categories, while keeping the thickest category unchanged, produced larger total ice area in summer and early autumn. For the rest of the year the total ice area is slightly less. Increasing the maximum thickness of the thickest ice category, while keeping the lower category thicknesses the same, has very little effect on total ice area. For ncat = 5 increasing the maximum thickness of the thin categories, while keeping the thickest category the same, produces a larger ice volume in mid and late summer but slightly less for the rest of the year. Increasing the maximum thickness of the thickest category while keeping the lowest category the same produces greater ice volume with a maximum in late October or early November. But the magnitude of the changes are small, i.e. less than 3% for area and less than 2% for volume.

2.5 The configuration of CICE4 for this Research

Unless specified CICE4 was run with the default parameters as specified in the user manual (Hunke and Lipscomb, 2008). For this project CICE4 is run as a moderately high resolution, regional model over the Southern Ocean. It is run on the "panantarctic" grid which includes all the sea ice regions around Antarctica (Fig. 2.5). The grid contains 330×330 grid cells and has the point of longitudinal convergence, which would normally be at the South Pole, displaced to the equator. Moving the longitudinal convergence is not important for the operation of CICE4 because it does no computation over the Antarctic Continent but it is for PolarLAPS which is used to model Antarctic weather. There is also a 90°, anticlockwise rotation of the grid so the prime meridian is horizontal and to the left. The dimensions of the grid cells vary over the domain but is ∼27 km. In the x-direction the size of the grid cell is 27.80 km and in the y-direction cells vary from 18.00 to 28.00 km (Fig. 2.5).

The model's land mask was based on the Mosaic Of Antarctica (MOA)
(URL: http://nsidc.org/data/moa/).
Modifications include the addition of landfast sea ice and sub-Antarctic islands. Islands have an effect when they interact with sea ice. Landfast sea ice acts very like land as far as pack ice is concerned. The landfast ice anchored by grounded icebergs is considered as land and included in the land mask (Fig. 2.5).

The time step of the model can be varied, but for this study it is one hour. This means that the spatial resolution is sufficiently large to avoid numerical instabilities associated with the ice dynamical calculations (Courant et al., 1928). The model is run standalone with forcing from the high resolution atmospheric model PolarLAPS and from the ocean general circulation model AusCOM.

The depth of the ocean's mixed layer has a strong influence on the amount of ice produced during the time interval when daily change in total ice area is positive. On average this is from the second half of February to the second half of September or from about day-of-year (DoY) 49 to 263. The model is modified to read in a hourly mixed layer depth (MLD).

Increasing air temperature decreases sea ice area throughout the year. Above annual average sensitivity occurs for the time interval from October to March. On average the model is most sensitive to air temperature in late February but sensitivity is also most variable at this time. November to January are months when the model is relatively insensitive to changes in

MLD and so air temperature is used to tune the model at this time of year. An adjustment value was read every time step and added to air temperatures over the model domain (Section 3.4.1). The adjustment value was added to each forcing grid cell value.

The model is modified to calculate a time-varying value for deep ocean heat entering the mixed layer based on Antarctic observations near Mawson Station (Allison, 1979). The deep ocean heat flux is greatest when ice production is greatest (25.60 W m^{-2}) early in the ice growth season (DoY 90) and has another, lesser peak value (6.97 W m^{-2}) in October (DoY 278). Outside the interval of DoY 86 to 334 the deep ocean heat was set to zero. In reality the deep ocean heat would vary in space as well as time but having a time-varying value is an improvement over the static value that is the default for the model. The annual average is about 4.5 W m^{-2} which is low compared to 16 W m^{-2} measured in the Weddell Sea (Gordon and Huber, 1990).

Running the model with a forced Sea Surface Temperature (SST) produced unrealistic spatial sea ice distributions. The solution to this is to use the slab representation of the ocean, internal to the model and thus allow natural, two-way interactions between ice and ocean. In this configuration the ocean is the mixed layer and is 1-dimensional in each grid cell. That is, water and energy are not moved between grid cells, even though the model incorporates ocean currents. These currents interact with sea ice only and do not move water within or between grid cells.

Lastly, the model is modified to calculate the surface downward radiation internally to the model (Sections 3.4.3 for short-wave and 3.4.4 for long-wave).

2.5.1 Sample simulations

This section presents simulations from a typical year compared to observations. A number of model fields can be used to do this comparison, including total ice area, concentration, and thickness.

Simulated ice concentrations (Fig. 2.6b) are compared to those estimated from the brightness temperature at microwave wavelengths (Fig. 2.6a). In July ice is growing and air temperatures are low so any open water within the pack is quickly frozen over with thin ice. Therefore the simulated ice concentration appears much higher than passive microwave estimates. The simulation could be more accurate because the algorithms used to analyse the passive microwave measurements have difficulty distinguishing thin ice from open water (Comiso and Steffen, 2001). When the thinnest simulated ice category is subtracted from the total ice concentration more structure appears within the pack (Fig. 2.6c). Despite this improvement the simulated pack ice has a much more uniform ice concentration than those derived from passive microwave.

The average of the concentrations greater than zero are calculated the passive microwave value is higher than the simulated, i.e. 86.6% (Fig. 2.6a) compared to 84.3% (Fig. 2.6b). This is due to the very low ice concentration region north of the 15% ice concentration contour, which for the simulation is wide and for the passive microwave is narrow. Subtracting category 1 from the simulated ice concentration reduces the average concentration to 80.8%.

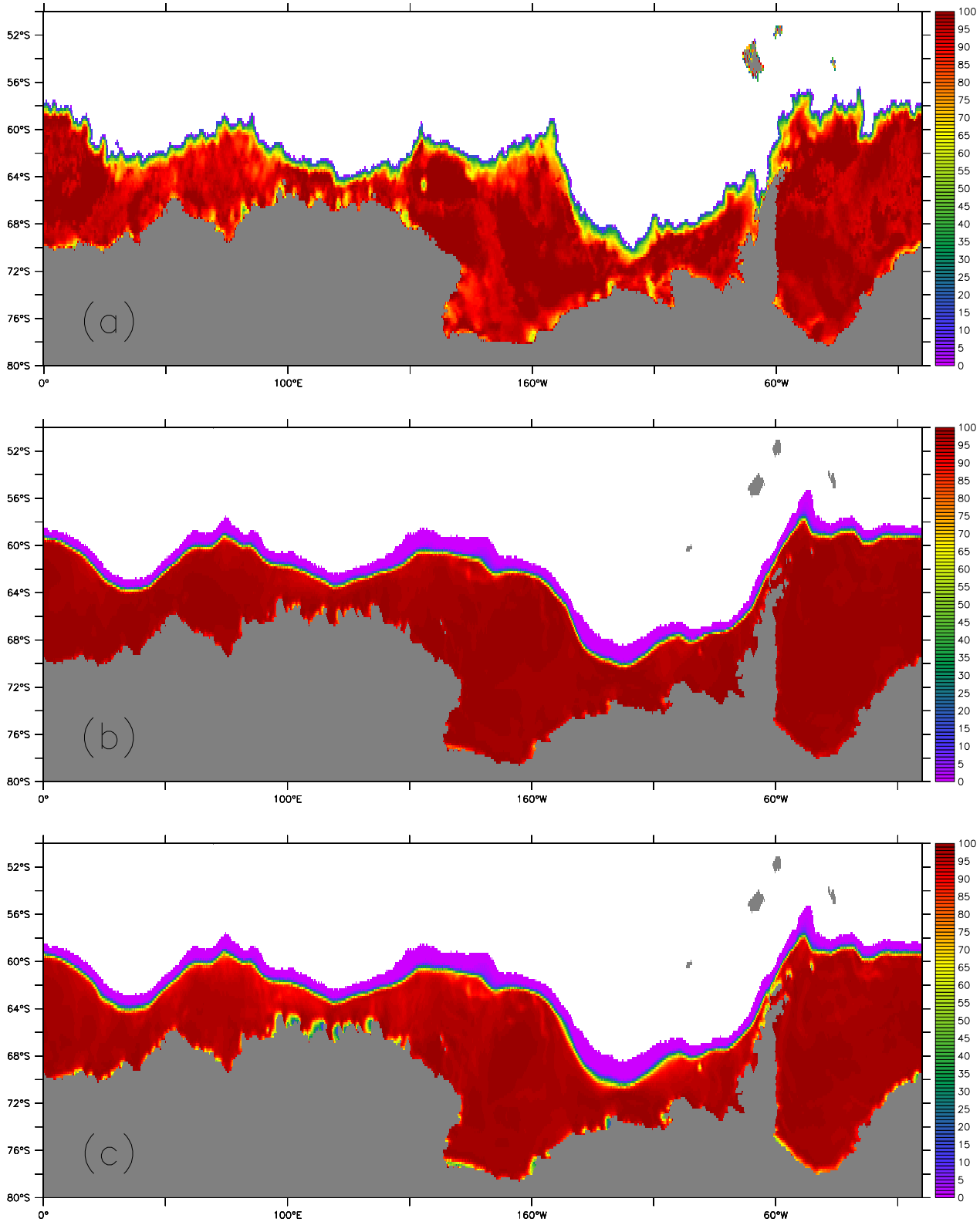

Figure 2.6: Ice concentration on 15 July 2007: (a) passive microwave; (b) total simulated; (c) total - concentration of thinnest ice category. Also shown is the land mask (grey).

Another difference between simulated and observed sea ice is that the marginal ice zone is

wider in the simulation and the simulated ice edge is smoothed. The algorithms used to analyse the passive microwave data cannot reliably detect sea ice at concentrations much below 15% while the model is able to identify ice down to very low concentrations. The relative smoothness of the simulated ice edge is more difficult to explain but is most likely caused by the averaging the model does over the grid cell.

Total ice area can easily be calculated by summing the product of the ice concentration within a grid cell by the area of the grid cell. There is a very good agreement[1] between the simulated total ice area and that derived from passive microwave (Fig. 2.8a). This is not surprising because the model was tuned to achieve this. However, the passive microwave-derived total ice area exhibits higher frequency variability. This can be highlighted by subtracting the simulated total ice area from the passive microwave-derive values (Fig. 2.7). From day 131 to day 285 there appears to be minor peaks and troughs superimposed on major peaks and troughs. The average period of the major variations is about 26 days (25.7 for peaks and 25.8 for troughs) and that of the minor variations is about 6.5 days. Synoptic weather systems have durations in the range of 6.5 days and this could be an explanation of the minor variations. The moon orbits the earth every 27.3 days (sidereal month) so a lunar cause of the major variations is not out of the question. However, 25.7 days is less close to the synodic month which is about 29.5 days which makes a lunar connection seem less certain.

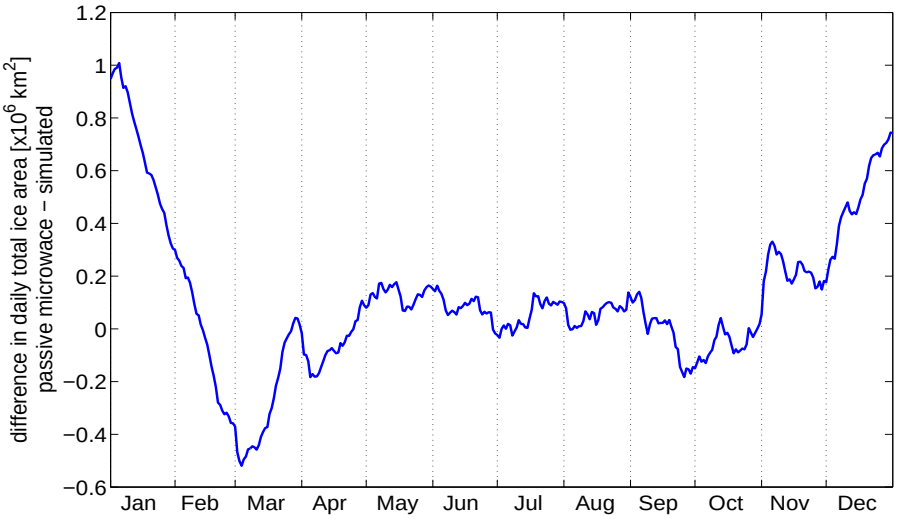

Figure 2.7: Variability over time intervals of days to a month revealed by subtracting the simulated total ice area from that derived from passive microwave averaged for 1998 to 2003.

Simulated total ice area and total ice volume are available in the log files. Average ice thickness can be calculated by dividing total ice volume by total ice area. Average ice thickness varies with season, from thinnest in early autumn and thickest in late summer (Fig. 2.8b). The explanation of this somewhat counter-intuitive behaviour is found in section 4.3.

[1]plotting the simulated against the passive microwave has a slope of 1.00 and an R^2 of 0.995 with the probability of this correlation being caused by chance being very low (2.2×10^{-16})

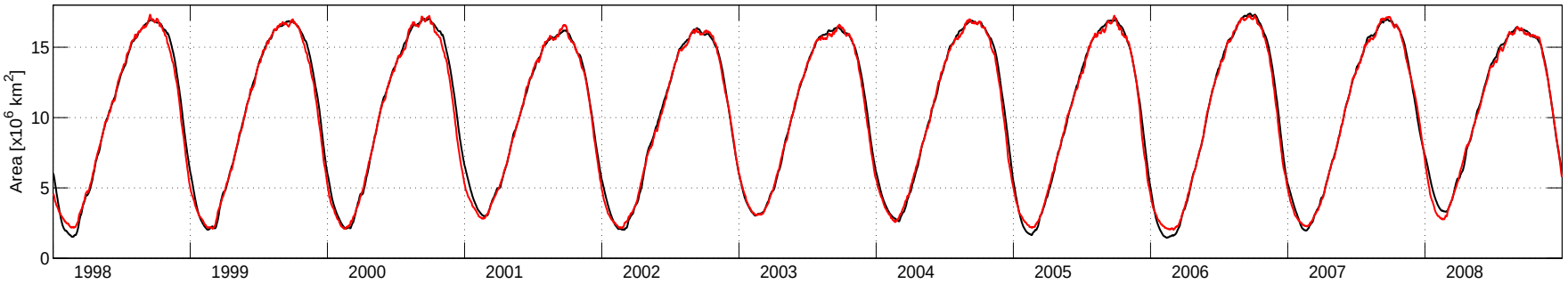

(a) Modelled total ice area (black) and passive microwave-derived total ice area (red).

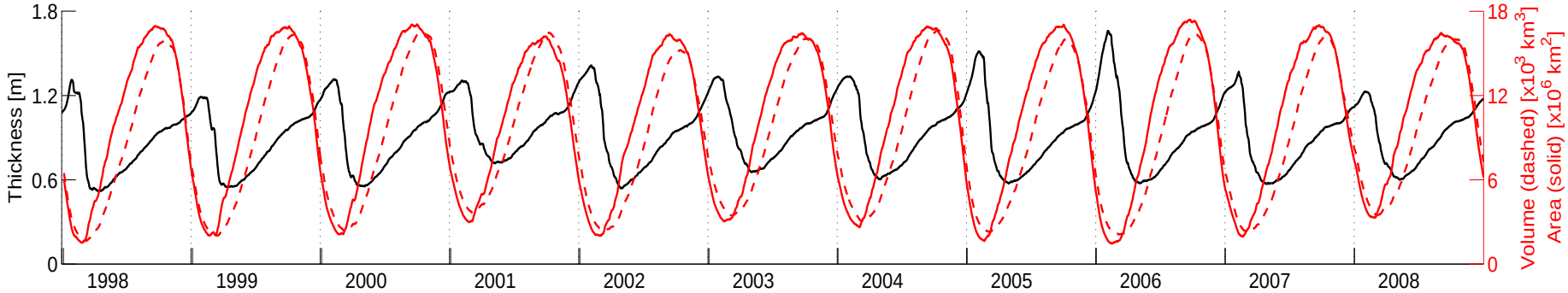

(b) Simulated average ice thickness (black), average ice area (solid red) and average ice volume (dashed red).

Figure 2.8: Eleven year simulation time series (1998–2008)

2.5.2 Model sensitivity simulations

One advantage of running the model stand-alone is that one forcing field can be varied while the others are not. The response of the model can then be quantified by comparing one or more prognostic fields between the control simulation and that with perturbed forcing. Total ice area was used at the prognostic field and the temporal resolution was daily. If the forcing was not perturbed by ±1% then the response was scaled to 1% by dividing by the percentage actually used. This makes three simulations for each forcing field studied. Model sensitivity could have been studied using two simulations but three were done to check that the model's response was linear. Sensitivity was measured by the percentage difference in total ice area for the perturbed simulation compared to the control. How closely the ±1% sensitivities corresponded is an indication of the linearity of the model's response. If they overlie each other the model's response is linear (Fig. 2.10, A.10) but if they are separate then there is some degree of non-linearity (Fig. 2.11, A.6) which indicates that the forcing perturbation was too large.

Below are the model sensitivity to the three forcing fields used to tune the model plus to ice density because of its importance to the volume of ice produced when a unit volume of sea water is frozen. Others are listed in Appendix A.

Mixed layer depth

Mixed layer depth is used to tune the model while there is net ice growth. It is easy to perturb the mixed layer depth because it is always positive, uses most of its range, i.e. greater than 10 m (maximum 180 m), and is supplied as an hourly scalar and all grid cells are set to this value. The perturbation used was ±10%.

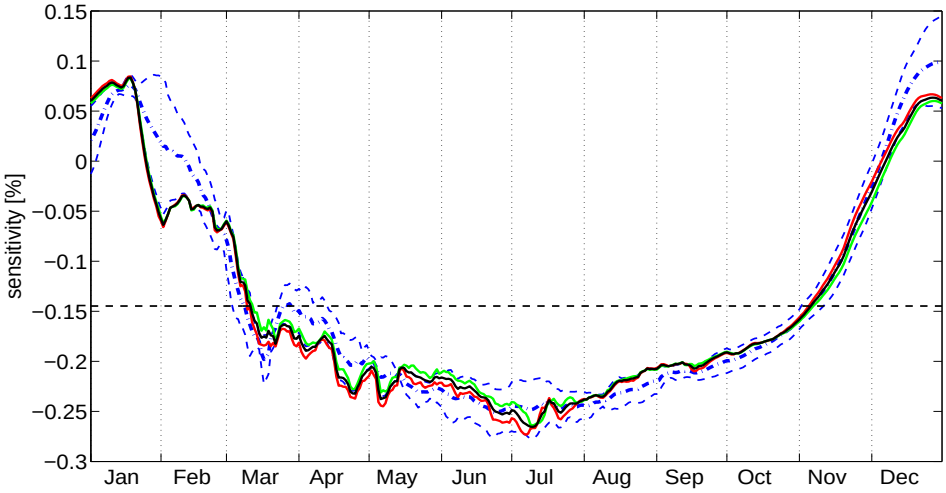

Figure 2.9: Model sensitivity to mixed layer depth for 1998 (black) with the +1% (green), -1% (red). The perturbation was ±10% of the optimal simulation values. Also shown is the average model sensitivities for the years 1998 to 2000 (thick blue dot-dashed) with ±1 sample standard deviation (thin blue dashed).

From mid February to early December an increase in mixed layer depth produces a decrease in the total ice area. The model is most sensitive to mixed layer depth in mid winter (23 June),

i.e. -0.25% (Fig. 2.9). In summer an increase in mixed layer depth has a positive influence on total ice area but to a less degree, i.e. sensitivity of +0.10%. Increasing the depth of the mixed layer in winter slows ice production because there is a greater volume of water to remove heat from. In summer, a deeper mixed layer means there is a greater volume of water to warm and so basal (and lateral) melt are less. Using the logic of the sensitivity study it would be possible to maintain more ice over summer if the mixed layer depth was allowed to continue to increase. However this was not done because it is know that the mixed layer becomes shallower as the sea ice melts and because it would be undesirable to have an abrupt shoaling of the mixed layer at the end of summer and the beginning of the ice growth season. Mixed layer depth values were manually adjusted in summer so that they were close to the minimum of 10 m when ice growth begins.

There is a some non-linearity in the 1998 sensitivity and it would have been better to use a smaller perturbation. However, the non-linearity is generally less than 1 sample standard deviation of the interannual variation in sensitivity (Fig. 2.9).

Air temperature

In summer, when mixed layer depth cannot be used for model tuning, air temperature was used for this purpose. This is less than ideal in that summer is also the season when the PolarLAPS surface air temperatures are in best agreement with the NCEP re-analysis (Fig. 3.4a). However, air temperature does have the advantage that the model is most sensitive to perturbed air temperature in summer (Fig. 2.10). Air temperature adjustment was minimized by also employing cloud fraction adjustment.

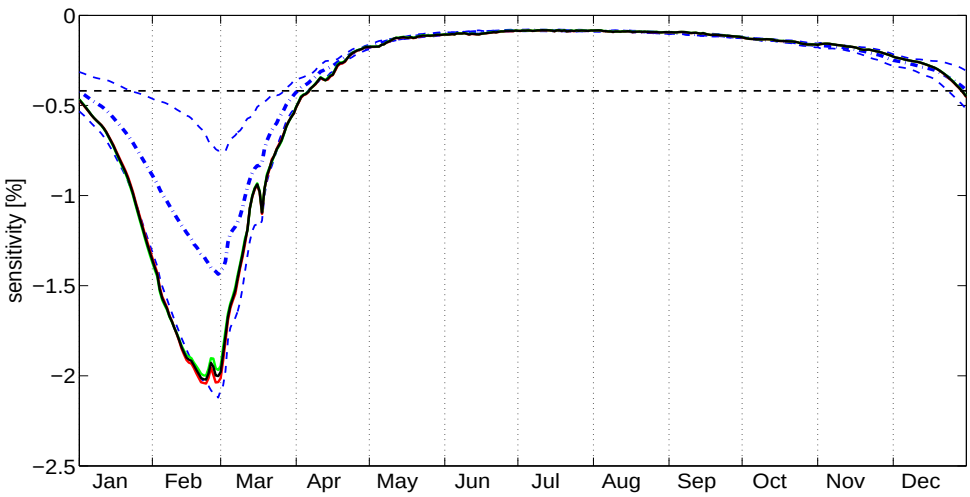

Figure 2.10: Model sensitivity to air temperature for 1998 (black) with the +1% (green), -1% (red). The perturbation was ±1% of the temperature difference between the top and the bottom surface of the ice or snow. Also shown is the average model sensitivities for the years 1998 to 2002 (thick blue dot-dashed) with ±1 sample standard deviation (thin blue dashed).

The problem with estimating the model's air temperature sensitivity is to know what to base the perturbation on. PolarLAPS supplies air temperature in units of absolute temperature. But 1% of a number that is about 270 ° above zero produces a comparatively large perturbation. If the Celsius scale is used instead of the absolute scale then the perturbation could be both

positive and negative. So what was chosen was the difference in temperature between the bottom of the ice and the top ice or snow surface. This base-line temperature could change sign because the bottom of the ice will be at the freezing temperature of the ocean (∼-1.8 °C) and the top surface can be at 0 °C. However, mostly the top surface will be colder than the bottom and the magnitude of the difference is small compared to Southern Ocean temperatures and absolute zero. 1% of the difference between the surface temperatures (bottom minus top) is a small value and gives a linear response from the model.

Increasing air temperature cause less total ice area at all times of year but the average maximum sensitivity is in late February (-1.44%) and the minimum is in early July (-0.08%). Model sensitivity is also most variable near the end of February. 1998 is a year that has high summer sensitivity (-2.02% on 22 February) while 2002 is a year when there is little (-0.58% on 26 February). In 1998 the model's sensitivity is close to one sample standard deviation away from the 1998–2002 mean.

Cloud fraction

Cloud fraction was chosen as the secondary summer tuning forcing field because in-situ cloud fraction observations are sparse in the Southern Ocean and because the model is most sensitive to changes in cloud fraction in summer. For the optimum simulation the cloud fraction was adjusted hourly over the entire domain by an amount specified in an input file and the average adjustment was most in January (+3.46%) and was zero by mid March. The sensitivity perturbation was ±1% on top of the optimum adjustment. In 1998 the model's sensitivity is close to one sample standard deviation away from the 1998–2002 mean.

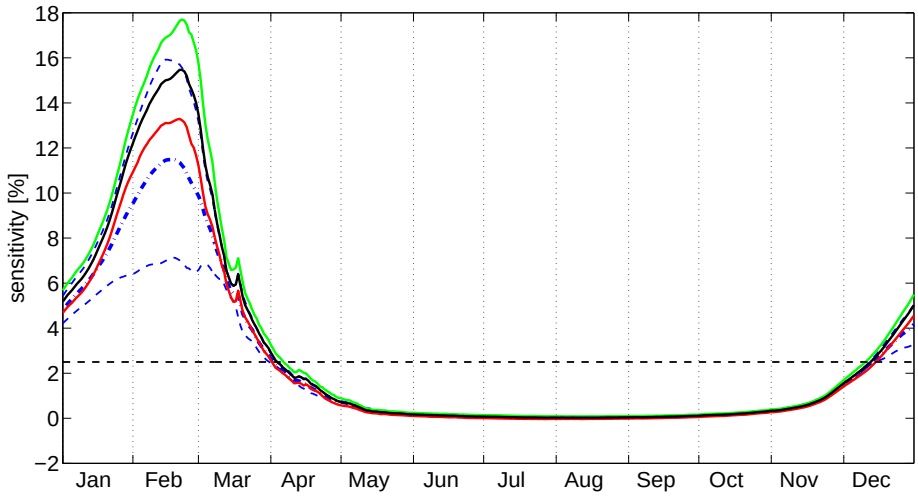

Figure 2.11: Model sensitivity to cloud fraction for 1998 (black) with the +1% (green), -1% (red). The perturbation was ±1% of the grid cell value. Also shown is the average model sensitivities for the years 1998 to 2000 (thick blue dot-dashed) with ±1 sample standard deviation (thin blue dashed).

Ice density

Ice density is a constant in CICE4 but in reality ice density will vary because of a number of factors including ice type, temperature, and salinity. A sensitivity study was conducted to

estimate the importance of ice density and to determine if the errors introduced by having a constant ice density are large. Because of its importance to ice volume calculations the sensitivity of ice volume was also analysed. Sensitivity to ice density is greatest in late summer whether calculated from changes in total ice area (2.19%) or total ice volume (5.2%). However, changes in ice density have about an order of magnitude larger impact on annual average ice volume compared to ice area, i.e. a 1% increase in ice density produces a 2.16% increase in ice volume compared to 0.22% increase for ice area. The sign of the volume sensitivity is always positive but the area response is positive in January to March and then slightly negative. The perturbation to ice density (± 40 kg m^{-3} or $\pm 4.36\%$) was sufficiently small to give a linear response for total ice area (Fig. 2.12) but too large for total ice volume (Fig. 2.13). These results should therefore be treated with caution as they may not be reliable.

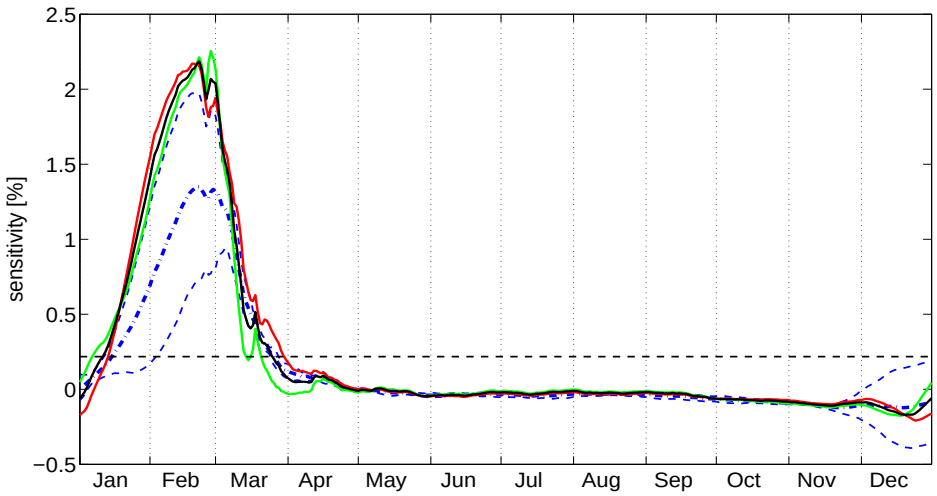

Figure 2.12: Model area sensitivity to ice density for 1998 (black) with the +1% (green), -1% (red). The perturbation was $\pm 4.36\%$ of the model constant value of 917 kg m^{-3}, i.e. ± 40 kg m^{-3}. Also shown is the average model sensitivities for the years 1998 to 2000 (thick blue dot-dashed) with ± 1 sample standard deviation (thin blue dashed).

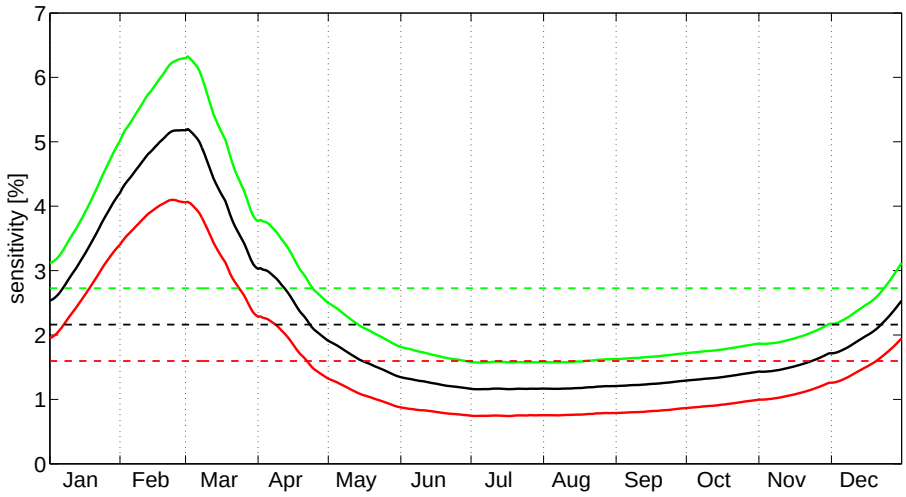

Figure 2.13: Model volume sensitivity to ice density for 1998 (black) with the +1% (green), -1% (red). The perturbation was ±4.36% of the model constant value of 917 kg m^{-3}, i.e. ±40 kg m^{-3}.

2.5.3 What's missing

A standalone implementation does not allow the types of interactions that occur in nature. For instance, in the model ocean surface currents interact with sea ice influencing ice advection but in nature sea ice movement also transfers momentum to the surface water. Other two-way interactions not present in the model include: momentum exchange from ice to atmosphere; mass exchange from ice to atmosphere; ice mediated mass exchange between ocean and atmosphere; heat flux from ice to atmosphere; ice mediated heat flux from ocean to atmosphere.

Ocean forcing has a monthly time step and a coarser spatial resolution than the model. This means that features that depend on variation of the ocean on small temporal and spatial scales will not be reproduced by the model, e.g. the 2002 sea ice tongue near 85 °E (Rintoul et al., 2008). For years 2006 to 2008, the ocean forcing used was an average of the years 1998 to 2005. The impact of using the mini-climatology were assessed by using it for simulations where ocean forcing was available and comparing the results. This was done for the years 1998–2001. If the total ice area averages of these four years are compared then there is very little difference when using the climatology, i.e. annual average of -1.4% (maximum in summer of almost 7%). However, during individual years there are differences both positive and negative and large. The differences are greatest in summer (peaks of about 6.5% for 1998, 20% for 1999 and 2000 and -54% for 2001).

While CICE4 includes frazil ice it is only produced in open water and once any ice is formed subsequent thermodynamic growth is treated as congelation ice. This means that ice types that can be important in the Southern Ocean are not represented, e.g. grease ice, pancake ice, granular ice, and platelet ice.

Tides are not part of the representation of the ocean. Tides have a large effect on sea ice movement in shallow waters of the continental shelf (Padman and Kottmeier, 2000).

Ocean waves are not represented. Short period ocean waves interact strongly with ice floes in the marginal ice zone (MIZ) but do not penetrate far into the pack (Squire, 1995; Squire et al., 1995; Squire, 2007; Vaughan et al., 2009). Long period waves can penetrate hundreds

of kilometres into the pack (Vaughan et al., 2009) and can break up large floes.

The slab ocean is essentially a one dimensional representation of the ocean. It has no bathymetry and does not move mass or energy horizontally. Other ice-ocean interactions are missing such as those affecting salinity. So the salinity of the ocean feeds into the ice production calculations but ice production/melting does not alter the salinity of the mixed layer. The mixed layer depth is constant in space when in reality it would vary. Its depth would be affected by sea ice growth and decay processes. Sea ice influences the amount of wind induced mixing that is possible.

Momentum interacts with the winds in a similar way, from wind to ice. Wind does not re-distribute snow on the sea ice.

Air temperature and humidity are unaffected by the presence or absence of ice. In reality there are strong heat and moisture fluxes over open ocean, which occur to a lesser extent over sea ice.

The deep ocean heat is a constant function for all years and is constant in space. This, in combination with no bathymetry, means that the model will not be able to simulate such phenomena as the sensible heat polynya which sometimes occurs in the vicinity of Maud Rise (Comiso and Gordon, 1987).

The model produces a set of grid cells next to land that have prescribed zero ice velocity. This amounts to prescribing fast ice in these locations and while ice can be added via advection it can only be removed by melting. Very thick ice produced by this mechanism is especially noticeable in the small embayments such as McMurdo Sound, which in the model is represented by two grid cell.

The land mask treats all non-pack ice as land and does not distinguish between fast ice, ice shelves or land. The land mask is static and so cannot adapt when things change, e.g. the break-up of the Larsen B ice shelf (Feb/Mar 2002) (NSIDC, 2002).

Even with what the model does represent there are simplifications. The density of snow and ice is constant. The salinity of snow and ice is constant. The production of frazil ice is limited to leads and ocean-only grid cells.

Icebergs can have a significant if local impact on sea ice but are not represented in the model. The giant icebergs B15 and C19 had major impacts on sea ice production in the Ross Sea during the years that they were grounded there (Martin et al., 2007). The land mask does include the grounded iceberg fields and the fast ice trapped between them but this is static and no floating bergs are included. However, modelling studies suggest that when considering all of Antarctica, floating icebergs have only a small impact of ice production (Hunke and Comeau, 2011).

2.6 The "ice_tracks" Application

2.6.1 Introduction to "ice_tracks"

Antarctic sea ice is a collection of ice floes of various sizes which fuse, break and interact with each other and with the atmosphere and ocean. Ice buoys with satellite trackers can be placed on suitable floes and so monitor the movement of the floe. Some of these ice buoys also have sensors that monitor the local environment. CICE4 represents sea ice as a thickness distribution and the only notion of sea ice floes is a prescribed diameter of 300 m which it uses in calculations of lateral melt. Therefore the CICE4 model cannot simulate the movement

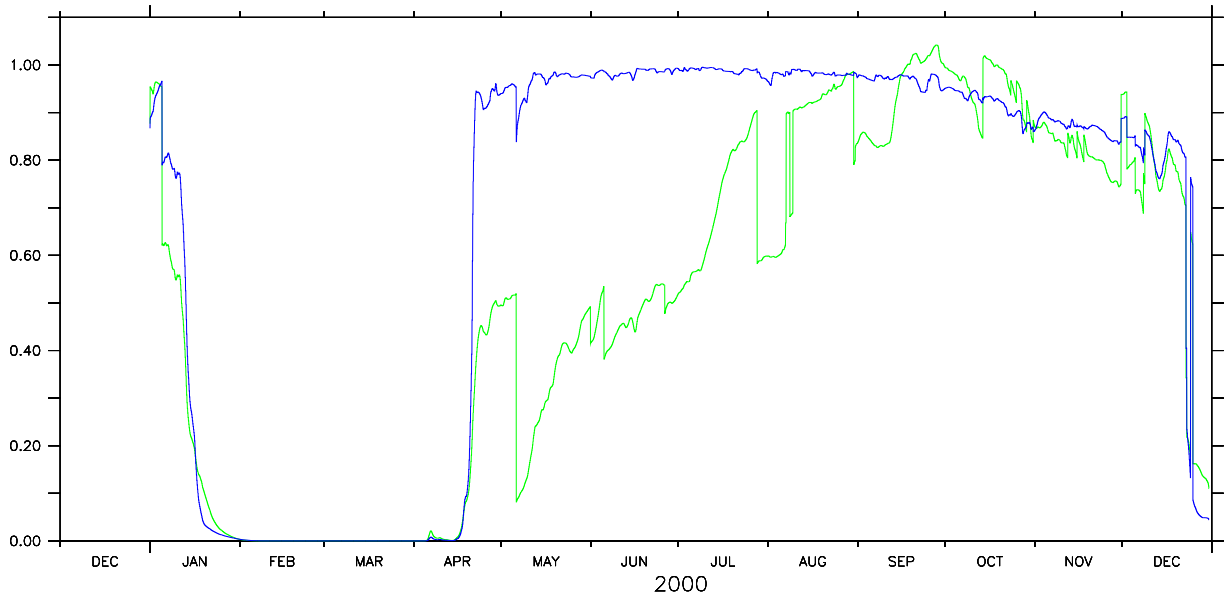

Figure 2.14: Ice thickness (green) and concentration (dark blue) for a Virtual Ice Buoy (VIB) near the coast plotted against the month for 2000. The vertical steps are due to the VIB changing grid cells and therefore coincident for thickness and concentration. The magnitude of the steps is greatest near the coast where adjacent grid cells can have very different values, e.g. the step in early May.

of ice floes or ice buoys. An attempt was made to simulate ice buoys using the gridded ice velocities that CICE4 produces and the following section describes this application.

2.6.2 How "ice_tracks" Works

What "ice_tracks" does do is integrate the ice velocity, at a specified location and time, with respect to time to produce a displacement. The displacement is added to the location to give a new location. The ice velocity at this new location is obtained for the incremented time and the process is repeated. A set of initial locations (latitudes and longitudes) are entered, each one representing the initial position of a Virtual Ice Buoy (VIB) and "ice_tracks" calculates the new location, hour by hour over the specified time interval. The "ice_tracks" application records the positions (latitudes and longitudes) for each VIB for each hour and these can be compared to the tracks of real ice buoys or to tracks obtained from other models. The "ice_tracks" application also reads forces acting on the virtual ice floe and many other environmental parameters and records these for each time step.

The "ice_tracks" application first compares the VIB latitude and longitude with the latitudes and longitudes of the corners of the grid cells. The sum of the distances of the VIB to the grid cell corners will be a minimum for the grid cell in which the VIB is located. The VIB then obtains all the values it needs from this grid cell. When a VIB moves from one grid cell to another values can abruptly change. This is most evident for sea ice properties such as area averaged ice thickness (Fig. 2.14).

In Figure 2.14 there is an interval from the middle of February to the end of March when

VIB 7 does not change grid cells. This is because it is not moving because all the ice had melted. When a VIB finds itself in a grid cell with no ice, and therefore no ice velocity, it "floats" in the same location until a time when ice forms and starts to move. In years past ice buoys were designed to float and could potentially be incorporated into the subsequent years ice growth in a similar way to VIBs. However, VIBs maintain the station of where they began to float while real buoys would drift under the influence of wind and currents.

Recorded fields

There are 41 simulated fields which each VIB record contains and these are listed in appendix C. Another example of these fields plotted against the hour of the year is presented later in the thesis (Fig. 2.14). The application also records the final locations (latitude and longitude) of all the VIBs, which can be used as a restart file for a subsequent run.

3. Forcing Data

3.1 Introduction

Forcing is the external boundary conditions that can vary in space and time and which are applied to the model. Forcing may include actual forces such as wind stress, but can also include other quantities such as sea surface salinity or surface air pressure. This chapter lists the forcing fields and gives a brief description. The models from which the forcing was obtained are then introduced. Finally, some comparisons are made between some of the forcing averages and those of the NCEP/NCAR-2 atmospheric re-analysis product. Unfortunately, an NCEP re-analysis product also supplied the boundary condition for the PolarLAPS simulations (section 3.3). While it would have been more desirable to have used an independent reanalysis such a product was not available.

3.2 Forcing fields summary

Some forcing fields were produced by other models which are briefly described in section 3.2. Below is a list of all forcing fields and where they were calculated:

air temperature	-	PolarLAPS
surface wind	-	PolarLAPS
surface air pressure	-	PolarLAPS
humidity	-	PolarLAPS
precipitation	-	PolarLAPS
cloud fraction	-	PolarLAPS
sea surface salinity	-	AusCOM
surface currents	-	AusCOM
sea surface height	-	AusCOM
short-wave radiation down	-	internally calculated
long-wave radiation down	-	internally calculated
long-wave radiation up	-	internally calculated
deep ocean heat	-	internally calculated and varying in time but constant in space
mixed layer depth	-	manually calculated and varying in time but constant in space

Sea surface temperature (SST) was available from both PolarLAPS and AusCOM but a forced SST produced poor quality simulations. So the slab ocean option was used allowing a more natural interaction between ice and mixed layer.

3.3 The Models

Spatially and temporally varying forcing was supplied by three models: PolarLAPS; AusCOM; CICE4 itself. CICE4 has been described previously. This section gives a brief description of the other two models.

PolarLAPS (Polar Limited Area Prediction Systems) was a numerical weather prediction model operated by the Australian Bureau of Meteorology (Adams, 2009). PolarLAPS was run on a grid with the South Pole displaced to the equator and with a 90 ° rotation. The displaced pole is to avoid converging meridians over the Antarctic continent but the reason for the 90 ° rotation was not explained. The grid is known in this thesis as the "panantarctic" grid.

The atmospheric forcing used in this project is produced by nesting the PolarLAPS domain within the NCEP-DOE Reanalysis-2 product (http://www.esrl.noaa.gov/psd/). The model is re-initialized every 24 hours and fields from +12 hours to +36 hours are saved. The atmospheric forcing was constructed from the hourly surface forecasts and three hourly upper-level forecasts. For each run, the model spins up for the first 12 hours. PolarLAPS interpolates from the 250-km resolution of the reanalysis product at the domain boundary to the ∼27.5 km resolution used by PolarLAPS.

PolarLAPS forcing includes the 132 months from January 1998 to December 2008.

AusCOM (Australian Climate Ocean Model) (Bi and Marsland, 2010) is a global general circulation ocean model coupled to a sea ice model. The ocean model is an implementation of the Modular Ocean Model version 4 and the sea ice model is CICE. AusCOM was run on a lower resolution grid and interpolated to the panantarctic grid. AusCOM forcing is available from January 1998 to November 2006 only.

3.4 Forcing fields details

This section contains an incomplete analysis of the atmospheric forcing and also a comparison of it to the NCEP/NCAR-2 atmospheric re-analysis product. Unfortunately, an NCEP re-analysis product also supplied the northern boundary condition for the PolarLAPS simulations (section 3.3). While it would have been more desirable to have used an independent reanalysis such a product was not available. Within the "panantarctic" domain PolarLAPS has its own physics and is run at higher spatial resolution so while not independent the comparison does highlight areas of interest and possible problems.

Using the PolarLAPS forcing as is CICE4 grossly underestimates total ice area in summer compared to passive-microwave estimates, i.e. less than 9% in the second half of February (Fig. 3.1). Results from such simulations are of limited use in examining the effects of a future climate. If 90% of the ice is missing in the simulations of the current climate then it will not take much increase in surface temperature to remove all ice. Having less than 10% of ice in summer also makes sensitivity results difficult to interpret.

This argues for an adjustment of some of the forcing fields. The two fields that were chosen were air temperature and cloud fraction. The adjustments were made over the entire model domain and to the minimum amount needed to produce sufficient summer ice area.

Air temperature and cloud fraction will be examined in this section along with some other forcing fields.

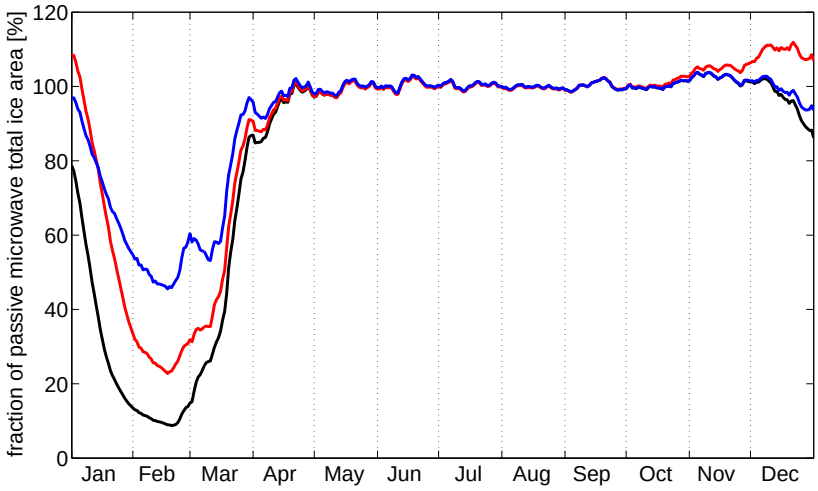

Figure 3.1: Fraction of passive microwave-derived total ice area for 1999 without adjustment to surface air temperature (red), cloud fraction (blue), and air temperature and cloud fraction (black).

3.4.1 Air Temperature

The PolarLAPS air temperature field is near surface (∼9 m) and has the units of absolute temperature. CICE4 converts absolute temperature to Celsius, which is used in the following analysis.

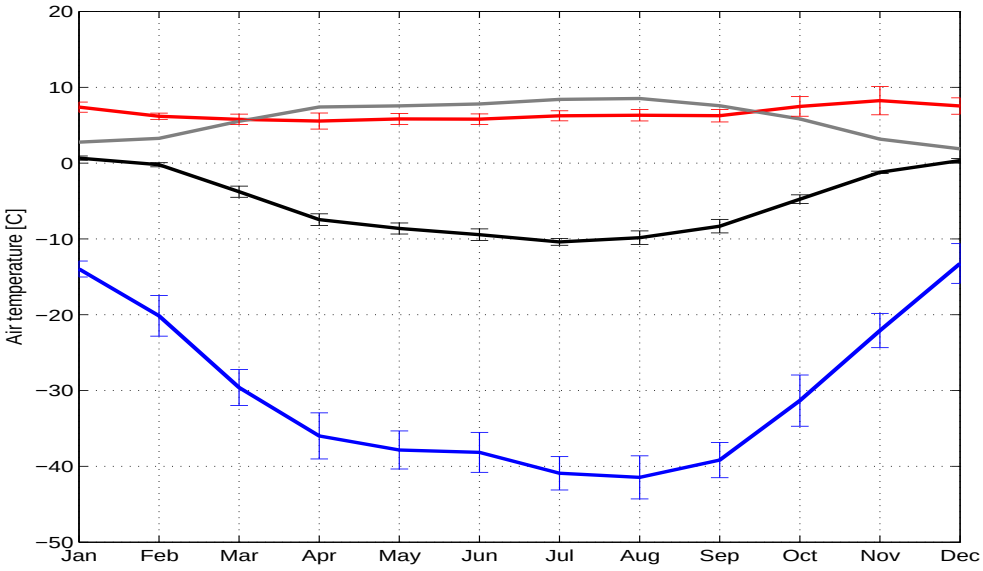

Figure 3.2: 1998 to 2008 average of monthly average air temperature in the sea ice zone with ±1 sample standard deviation of interannual variability as error bars: Average air temperature (black line); maximum air temperature (red line); minimum air temperature (blue line); the variability of air temperature within the month (1 sample standard deviation) (grey line).

The 1998 to 2008 average of the monthly average air temperature in the sea ice zone is a

maximum in January (0.66 °C) and a minimum in July (-10.4 °C) (Fig. 3.2). August is the month with greatest interannual variability in average air temperature (one sample standard deviation = 0.89 °C) and November has the least (one sample standard deviation = 0.16 °C). Within each month the maximum variability of air temperature in space and time occurs in August (one sample standard deviation = 8.52 °C) and the minimum is in November (one sample standard deviation = 1.88 °C).

Low surface air temperatures are important for the initial growth of sea ice in open water, i.e. frazil (Alam and Curry, 1998) and a contributor to the surface energy balance once sea ice has formed (Maykut and Untersteiner, 1971). The monthly average summer air temperatures in the sea ice zone are close to zero (Fig. 3.2). Monthly average winter temperatures are close to -10 °C and are more variable than those of summer as measured by sample standard deviation. Another measure of variability is the difference between the monthly minimum and maximum temperatures. The monthly maximums do not vary much throughout the year (about 7 °C) but the monthly minimums decrease from about -13 °C in December and January to less than -40 °C in August (Fig. 3.2).

From March to September the average air temperature in the sea ice zone is less than 0 °C. The -2 °C isotherm is north of most of the ice (Fig. 3.3a). In October there are areas near the ice edge where the air temperature is above 0 °C. The fraction of the ice in the above 0 °C air temperature areas increases from October to January. In all months there are areas where the average air temperature is below -2 °C (Fig. 3.3b). Appendix D details monthly average air temperatures from January to December for 1998 to 2008 in the sea ice zone.

Compared to the NCEP re-analysis PolarLAPS produces higher air temperatures in the sea ice zone (Fig. 3.4), with the largest average difference in autumn of 3.25 °C (difference ranging from -1.48 °C to 8.36 °C) (Fig. 3.4b). The least average difference occurred in summer with PolarLAPS being 0.56 °C higher than NCEP (difference ranging from -3.24 °C to 6.05 °C) (Fig. 3.4a).

The regions where PolarLAPS air temperatures are highest compared to NCEP are near the Antarctic coast. Usually they are adjacent to, rather than coincident with, the zones of high katabatic outflows from the Antarctic plateau. For instance, in March there are katabatic flows around 71 °E, i.e. 67–75 °E (Fig. 3.10c), but the maximum difference between PolarLAPS and NCEP in air temperature for March, April, and May occurs to the east and west of this zone (Fig. 3.4b).

The adjustment to air temperature was made from the beginning of November to the middle of March (early April in 2003) with a maximum average adjustment usually in January of -3.04 °C (maximum of -4.0 °C in early February for 1998 and 1999).

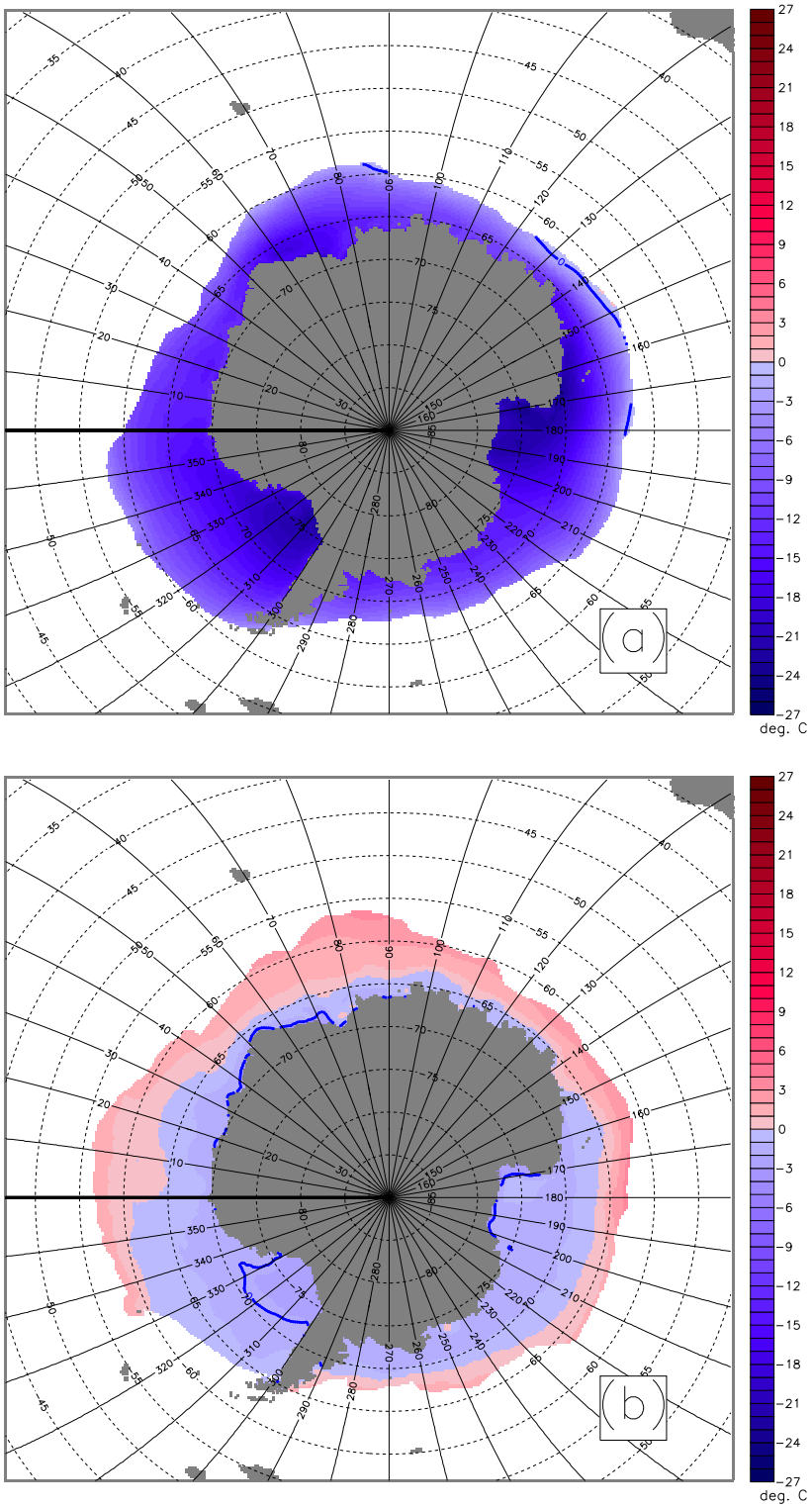

Figure 3.3: July and December monthly average air temperature in the sea ice zone: a) July; b) December. Areas shaded in warm colours have average air temperatures above the freezing point of fresh water. The blue contour is the -2 °C isotherm. In July almost all the sea ice zone experiences air temperatures below -2 °C while in December this area is reduced to the southern Weddell Sea. In December almost half the sea ice zone has air temperatures above 0 °C.

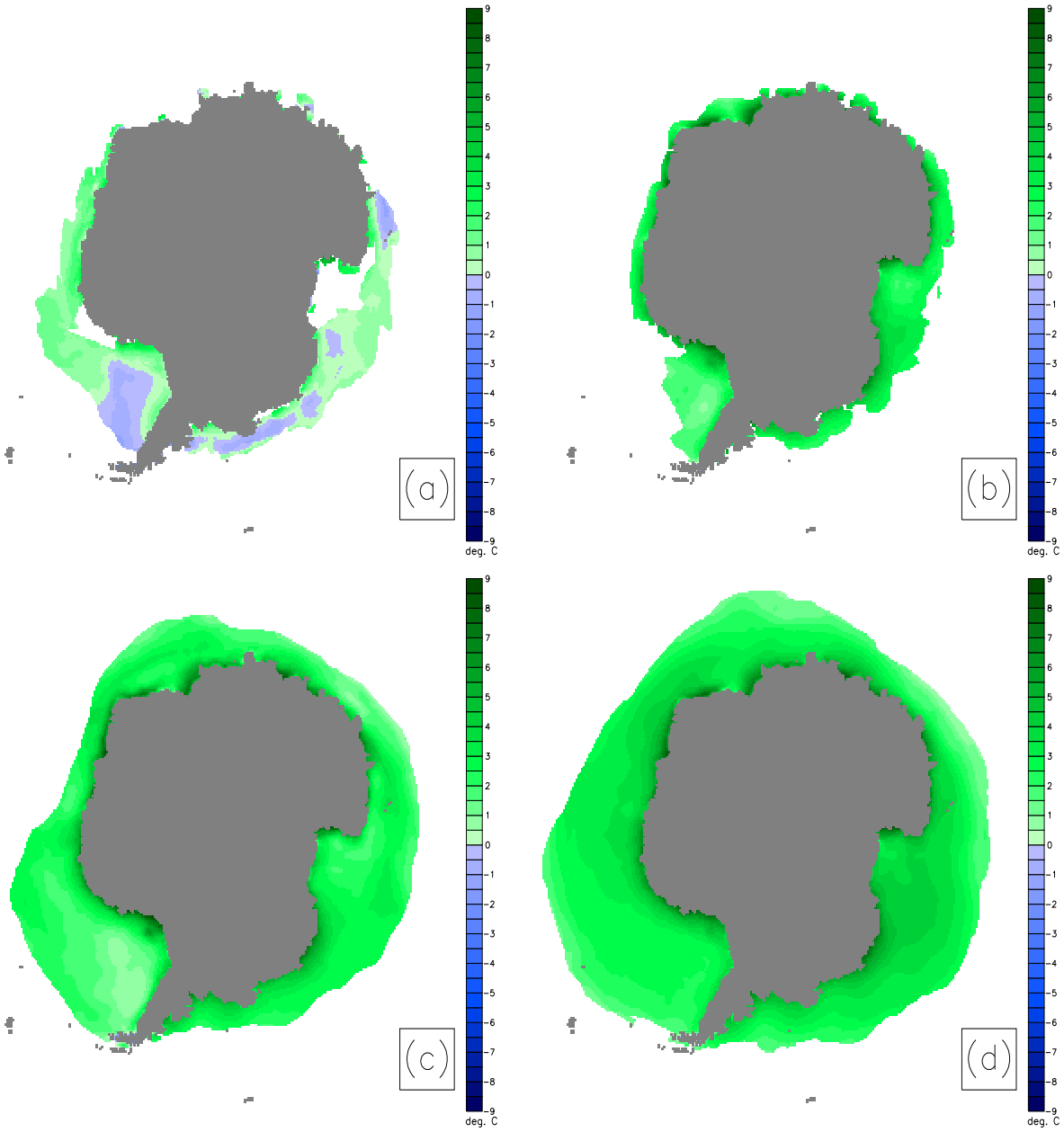

Figure 3.4: Difference between PolarLAPS and NCEP in seasonal average air temperature within the sea ice zone: a) Summer (December to February); b) Autumn (March to May); c) Winter (June to August); d) Spring (September to November).

3.4.2 Cloud Fraction

PolarLAPS calculates cloud fraction (cf) by the equation:

$$cf = \sum_{i=bottom}^{top} a * CLWC_i + b * CIWC_i$$

where i is the i^{th} vertical layer of the PolarLAPS model, $CLWC$ is the cloud liquid water content, $CIWC$ is the cloud ice water content, a and b are tuneable constants.

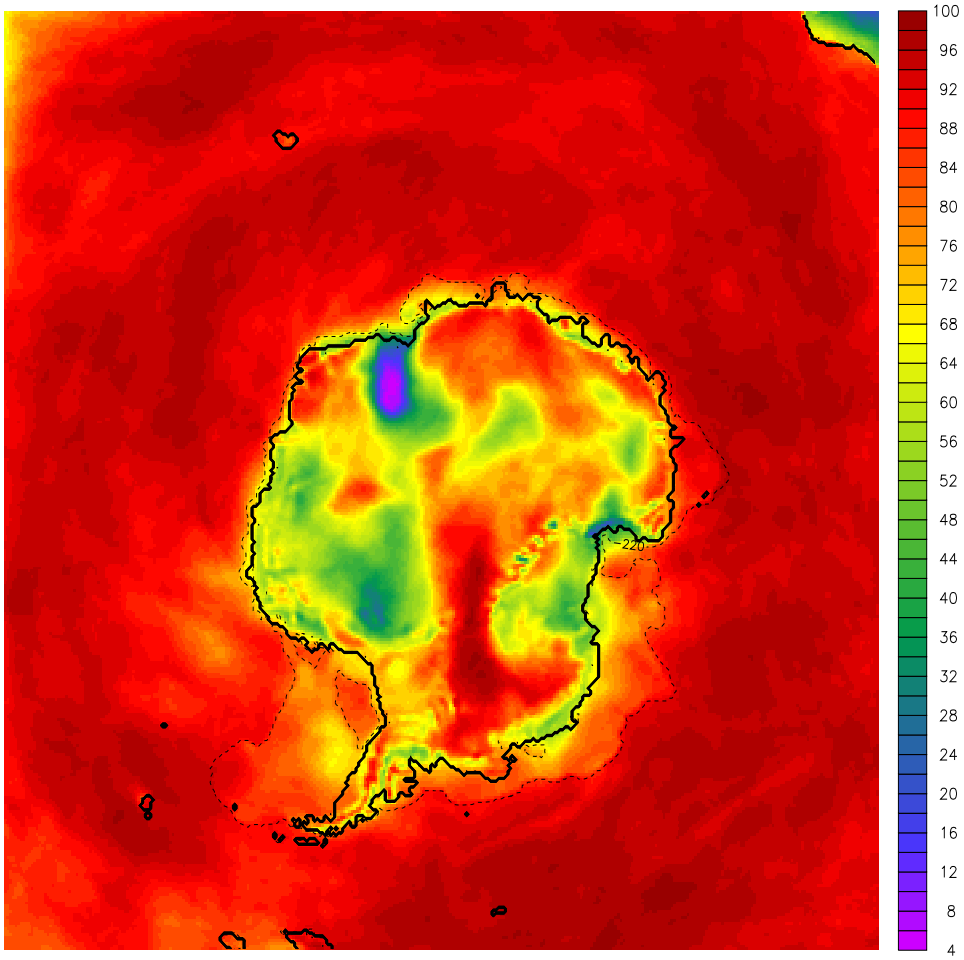

Figure 3.5: Average cloud fraction [%] for January 1998. Also shown is the PolarLAPS ice mask (light blue dashed) and the Antarctic coast (black).

PolarLAPS cloud fractions in the sea ice zone are probably too low. This is because there were few radiosonde measurements for the simulation interval and what there are did not include the ice component of clouds, only liquid water (Adams, 2010). The effect of using low values for cloud fraction is higher short-wave radiation intensity at the surface and lower downward long-wave radiation intensity. This will produce surface air temperatures that are too high in summer and too low in winter. In the Arctic Ocean sea ice correlates negatively with cloud fraction (Palm et al., 2010). Satellite-based cloud fraction measurements in the southern hemisphere also show reduced cloud fraction in the sea ice zone (Bromwich et al., 2012). However, there is evidence for increased very low level cloud fraction over sea ice, especially near the sea ice edge and in the MIZ (Adams, 2010; Cuzzone and Vavrus, 2011). PolarLAPS does produce higher cloud fraction over its prescribed ice mask (Fig. 3.5). However, the PolarLAPS ice mask will generally not be similar to the one simulated by CICE4.

An adjustment to cloud fraction was made from November to early March with maximum adjustment in January, i.e. January average 3.3% (maximum 4% in 1998 and 1999).

3.4.3 Short-wave Radiation Down

PolarLAPS did have a short-wave radiation field but it was a net flux field and therefore not useful. CICE4 expected to get total downward flux and it calculated its own net flux. Unfortunately, by the time this was identified PolarLAPS had been decommissioned so a re-run was impossible.

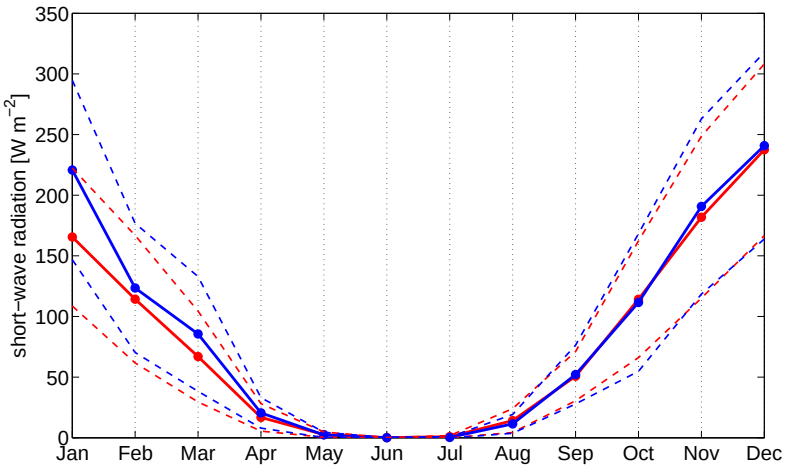

Figure 3.6: Monthly average downward short-wave observations (red) and model (blue) with ± 1 sample standard deviation. The observations were made at Rothera Point Station on the Antarctic Peninsula and the model values from the closest grid cell.

CICE4 had a subroutine to calculating downward short-wave radiation. This was evaluated and found to be satisfactory when considering average intensity. However, the flux spatial distribution on any particular time step was not as realistic as that provided by the code that was used. This code was based on Zillman (1972) (Equation 3.1).

$$fsw \downarrow = fsw_0 \, (1 - 0.6 \, cf^3) \tag{3.1}$$

where cf is the cloud fraction and fsw_0 is calculated using:

$$fsw_0 = \frac{S \, cos^2 Z}{(cos \, Z + 2.7) \, vp \times 10^{-5} + 1.085 \, cos \, Z + 0.10} \tag{3.2}$$

where S is the solar constant with a value 1353.0 W/m^2, Z is the solar zenith angle, vp is the vapour pressure with a value of 3.66 Pa. The value of $cos \, Z$ is calculated from:

$$cosZ = sin \, \phi \, sin \, \delta + cos \, \phi \, cos \, HA \tag{3.3}$$

where ϕ, δ, and HA are latitude, declination, and hour angle respectively.

Monthly average downward short-wave radiation intensities from the model were compared to observations made at a number of Antarctic stations. The model values were obtained from the nearest ocean grid cell to the location of the station. Best agreement between model and observations (Fig. 3.6) was obtained for Rothera Point Station which is located on the west side of the Antarctic Peninsula and very near the ocean. The model did not perform as well for the other stations, i.e. Neumayer and Halley. In both of these cases the model underestimated monthly average fluxes by larger than a sample standard deviation in spring and summer. Neumayer and Halley are on the Antarctic mainland and further from the coast making the comparison less reliable.

3.4.4 Long-wave Radiation Down

PolarLAPS did have a long-wave radiation field but it was a net flux field and therefore not useful. CICE4 expected to get total downward flux and it calculated its own net flux. Because a re-run of PolarLAPS was not possible an alternative, much simpler parameterization was used within CICE4. Downward long-wave radiation is calculated in the model. This is done following Parkinson and Washington (1979) (Equation 3.4):

$$flw \downarrow = \sigma T_a^4 \{1 - 0.261\, exp\,[-7.77 \times 10^{-4}\,(273 - T_a)^2]\}\{1 + 0.275\, cf\} \tag{3.4}$$

where σ is the Stefan-Boltzmann constant, T_a is the air temperature, and cf is the cloud fraction.

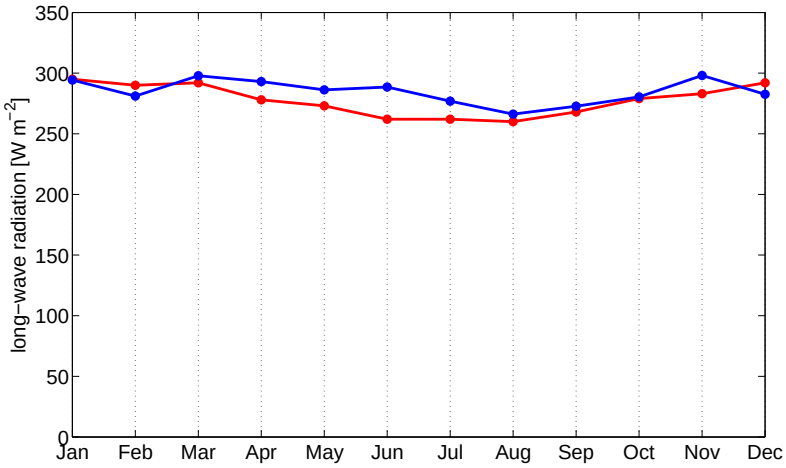

Figure 3.7: Monthly average downward long-wave observations (red) and model (blue). The observations were made at King Sejong Station on King George Island off the extreme tip of the Antarctic Peninsula. The model values are the average of the four closest grid cells.

Despite its lack of sophistication the monthly average the parameterization gives good agreement with observations made at King Sejong Station (Fig. 3.7). This is a single spot comparison and therefore should not be relied on too much but it gives a little confidence that downward long-wave radiation values are not wildly wrong.

3.4.5 Mixed Layer Depth

There are in-situ measurements of mixed layer depths in the Southern Ocean, some using ARGO floats (Sallée et al., 2010) and some also including ship-based profiles (de Boyer Montégut et al., 2004). However, there are considerably fewer measurements under sea ice. While there are some measurements using Ice-ARGO floats (Williams et al., 2011b; Wong and Riser, 2011) and some drift station observations (McPhee and Martinson, 1994) the bulk of recent profiles made within sea ice regions have been obtained using instrumented elephant seals (Charrassin et al., 2008; Williams et al., 2011a). Adult elephant seals will feed in high concentration pack ice (Bornemann et al., 2000) and dive to over 1000 m (Hindell et al., 1991).

The depth of the mixed layer varies with season (Wong and Riser, 2011). In summer the mixed layer is relatively shallow and fresh from the sea ice melt (Williams et al., 2011a; Wong and Riser, 2011). The depth of the mixed layer increases through autumn and winter and often reaches a maximum in spring (Wong and Riser, 2011).

Mixed layer depth varies in space as well as time (de Boyer Montégut et al., 2004). However, the configuration of CICE4 in this research incorporated only temporal variation. The mixed layer depth was chosen for tuning the model because it is not well constrained by observations. Using an initial estimate of mixed layer depth values (usually the optimum set from the previous year) and the model's response to small changes in mixed layer depth two or three simulations were usually sufficient to determine an optimum set of mixed layers (Fig. 3.8) and these values are plausible when compared to in-situ measurements (Wong and Riser, 2011).

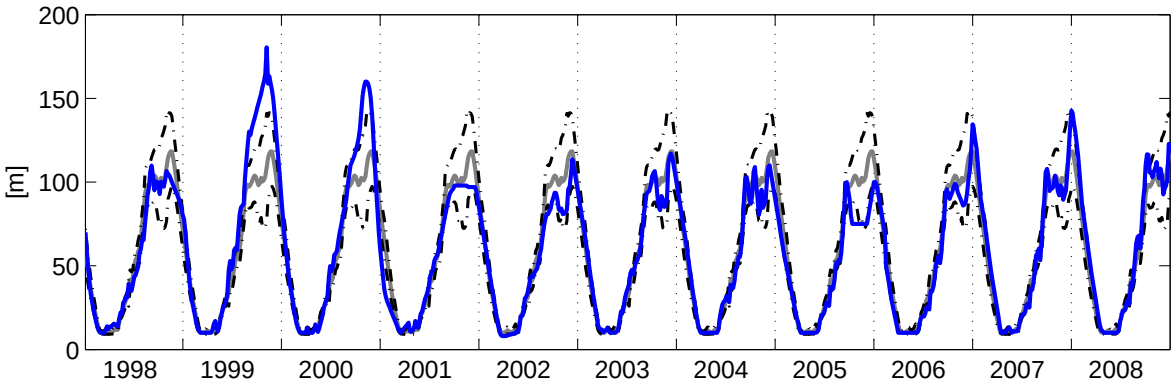

Figure 3.8: Mixed layer depth used for years 1998 to 2008 (blue line) with the average MLD (grey line) and ±1 sample standard deviations (black dot-dashed lines).

3.4.6 Surface Wind

The PolarLAPS winds are near surface and are provided as "u" and "v" components, which are positive from the bottom to the top of the grid and from left to right. The "u" and "v" components are converted to southerly wind speed, and westerly wind speed for this analysis. The meridional winds are thermodynamically important because southerly winds are relatively cold and northerly winds are relatively warm. The following analysis of the wind forcing is restricted to grid cells with sea ice. A general description is that wind speeds are high and easterly near the coast, have a lower value in the vicinity of the Antarctic Divergence, and are high again but westerly further north (Fig. 3.10a and 3.10b).

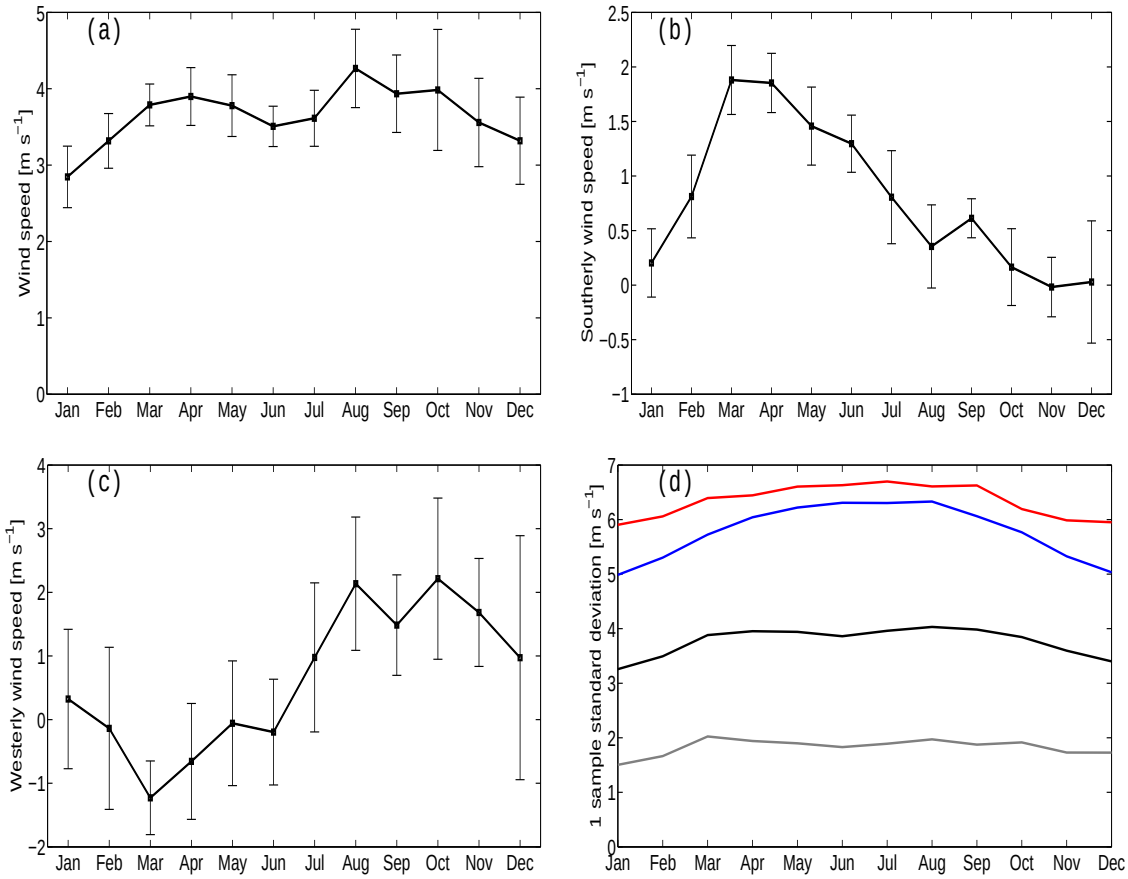

Figure 3.9: Panantarctic monthly average wind 1998 to 2008 in the sea ice zone with ±1 sample standard deviation interannual variation in monthly average error bars: a) wind speed; b) southerly wind speed; c) westerly wind speed. d) Variability within each month given by 1 sample standard deviation: westerly (red line); southerly (blue line); wind speed (black line); monthly average wind speed (spatial variation only) (grey line).

The monthly average wind speed has a minimum in January (2.85 m s^{-1}) and a maximum in August (4.27 m s^{-1}) (Fig. 3.9a). October has the highest interannual variability of monthly average wind speed (0.79 m s^{-1}), and June has the least (0.26 m s^{-1}). March has the highest monthly average southerly wind speed (1.88 m s^{-1}), and November has the least (-0.02 m s^{-1}), i.e. slightly northerly (Fig. 3.9b). December has the most interannual variability in monthly average southerly wind speed, and September has the least. Wind speed variability within the months is most in August and least in January.

PolarLAPS wind speeds are generally lower than NCEP. Only in summer is the average PolarLAPS wind speed greater than for NCEP in the sea ice zone (0.52 m s^{-1}, with difference ranging from -4.45 m s^{-1} to 4.34 m s^{-1}) (Fig. 3.11a). Autumn is the season when the average NCEP wind speed is largest compared to PolarLAPS (-0.87 m s^{-1}, ranging from -8.69 m s^{-1} to 4.43 m s^{-1}) (Fig. 3.11b). In the vicinity of the Antarctic Divergence, PolarLAPS produces stronger wind speeds, while NCEP is stronger to the north and south of the Antarctic Divergence (Fig. 3.11d). In Mackenzie Bay (70–72 °E) and further north, PolarLAPS produces slightly stronger winds but in the adjacent Cape Darnley region and further west (57–68 °E), NCEP winds are much stronger i.e. by more than 9 m s^{-1}.

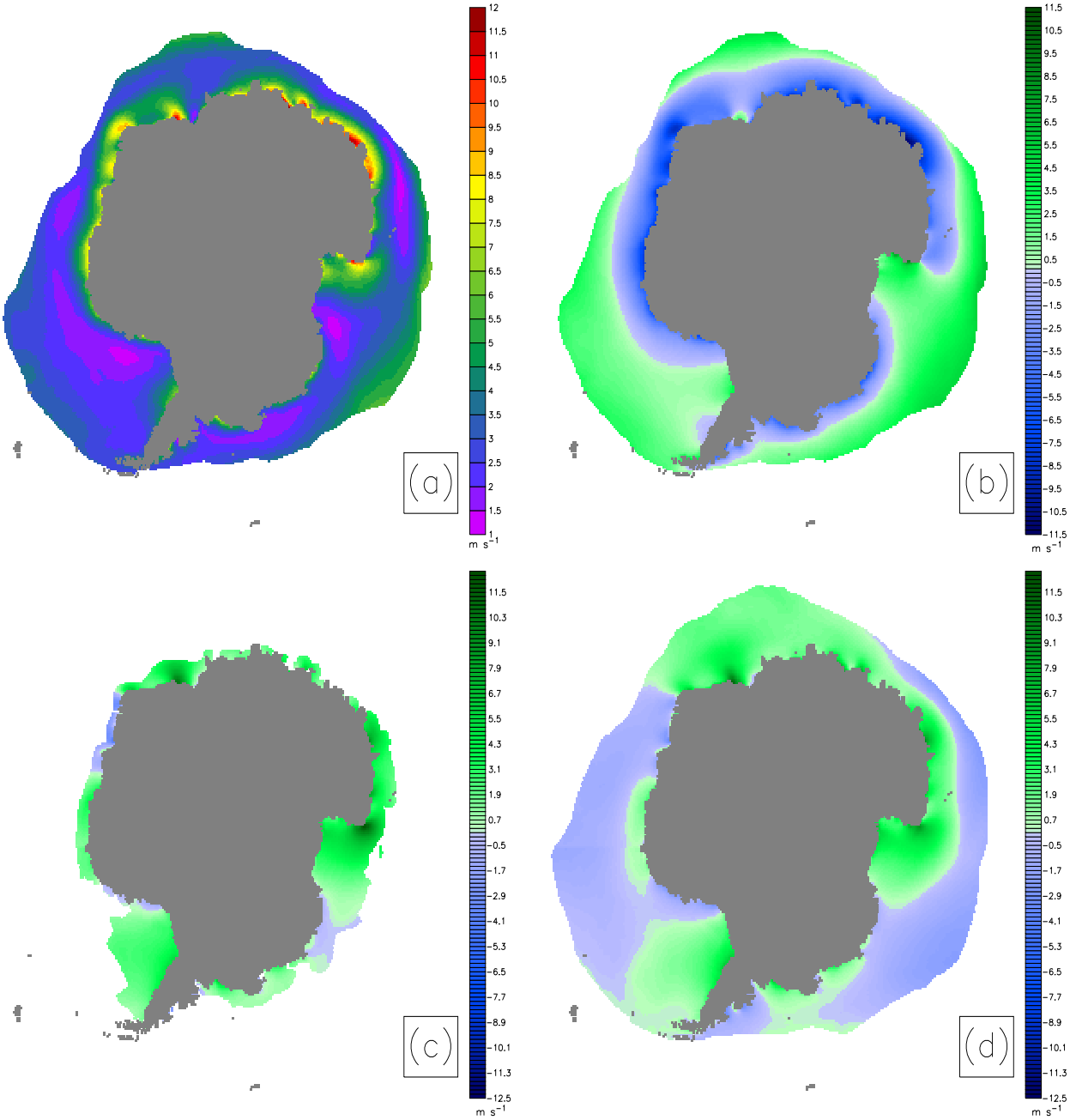

Figure 3.10: Monthly average wind speeds in grid cells with sea ice: a) July wind speed; b) July westerly wind speed; c) March southerly wind speed early in the ice growth season; d) August southerly wind speed late in the ice growth season.

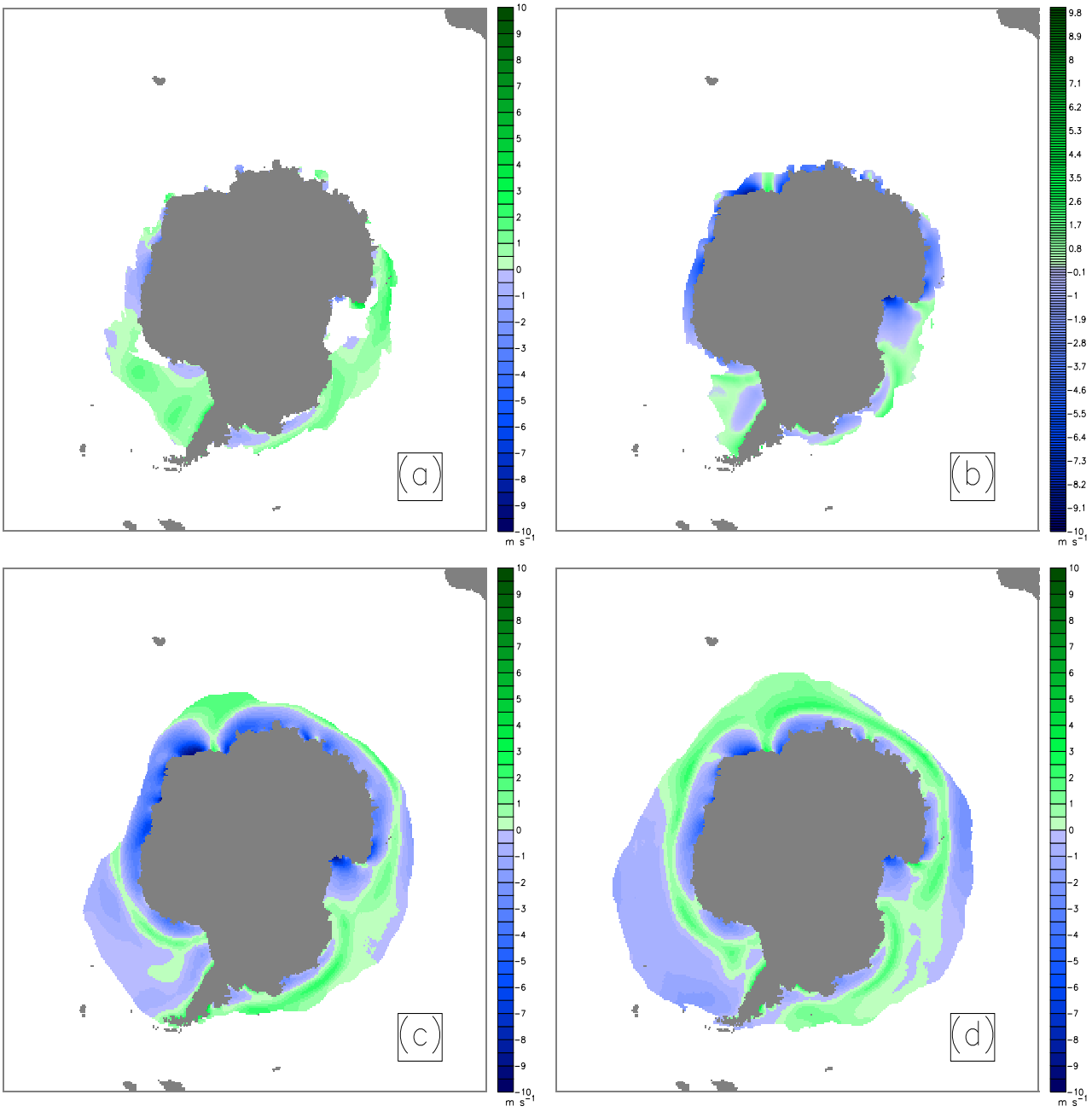

Figure 3.11: Difference between PolarLAPS - NCEP in seasonal average wind speed within the sea ice zone: a) December, January, and February; b) March, April, and May; c) June, July, and August; d) September, October, and November.

4. Results

4.1 Introduction

This chapter presents the results that are used to investigate the research questions. Section 4.2 presents aspects of simulated ice growth and decay that support the research question results. Section 4.3 examines the relationship between total ice volume and total ice area. Section 4.4 examines the role ice advection contributes to determining the latitude of the sea ice edge. Section 4.5 reports on simulations using forcing that is compatible with IPCC Fourth Assessment Report (AR4) projections for Southern Ocean climate in the year 2100.

All simulations shown in this chapter have an adjustment of air temperature and cloud fraction applied over the model domain as described in chapter 3. This was done because without any adjustment the total ice area in summer is as low as 6.6% of passive microwave-derived estimates of total ice area (Fig. 3.1). It would be pointless examining changes for the 2100 projections using IPCC AR4 consistent forcing if almost 95% of the sea ice is missing from the present day simulation. Also the results of variability of total ice area and total ice volume would be impacted by such a large deficit. Examination of thermodynamics and ice advections in maintaining the latitude of the ice edge would be little affected by the summer ice deficit. In the time interval April to December the deficit is no worse than 75% of passive microwave-derived estimates of total ice area. However, the simulations used for these results included the same air temperature and cloud fraction adjustment for consistency.

4.2 Ice growth and decay

This section examines the processes for increasing ice thickness and some typical examples showing the spatial distribution of the various growth processes. Then the processes of ice decay are examined and typical examples are presented.

4.2.1 Ice growth

There are large differences between the contributions made by the four ice growth mechanisms. Growth here refers to growth in thickness and so includes dynamic as well as thermodynamic ice growth. During its month of peak production (July) congelation ice accounts for 67% of total production in CICE4 (Fig. 4.1). Dynamic ice growth is next largest with 24% of total production in its peak month of August. Frazil ice is next largest with 7% in its peak month of July. The least is snow ice which produces 4% in its peak month (August).

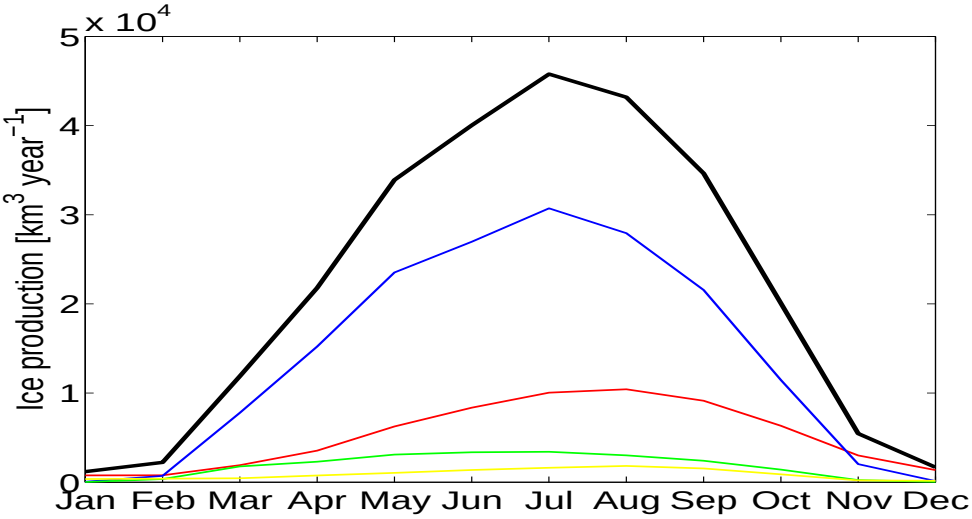

Figure 4.1: Monthly average ice volume production for 1998 to 2008: total (black); congelation ice (blue); dynamic (red); frazil (green); snow-ice (yellow).

Congelation ice grows under calm conditions and under existing ice when more heat is conducted upward from the bottom surface than enters from the ocean. The rate of heat conduction is determined by the thermal conduction coefficients of ice and snow, the difference in temperature between the top and bottom surfaces and the thickness of the ice and snow. In CICE4 the thermal conductivity of ice and snow are constants. Congelation growth is greatest in locations where the ice and snow are thin and the top surface temperature is low (Fig. 4.2b). The decrease of ice growth as ice thickness increases is similar to exponential decay. Therefore an exponential decay curve of the function $y = 1.3 * x^{-1.7} + 0.2$ has been overlayed and while it is a little too far to the right almost all the data points are below this curve. Why a small fraction of the data points are above this curve was not determined but it could be the effect of snow thickness which was not controlled for.

Top surface temperature depends on the balance of the various sources of energy arriving at the surface. Surface temperature correlates best with air temperature (Fig. 4.2a, $r^2 = 0.96$, $p < 2.2 \times 10^{-16}$). The next best correlation is with downward long-wave radiation (Fig. 4.3a, $r^2 = 0.77$, $p < 2.2 \times 10^{-16}$). In the model downward long-wave radiation and air temperature are not independent. As air temperature decreases the range of downward long-wave radiation intensities decreases (Fig. 4.3b). This is clearly not a linear relationship but the best linear fit has been superimposed as indicative only.

Because the top surface temperature correlates with air temperature it is useful to group congelation growth by air temperature when plotting growth against ice thickness (Fig. 4.2b). Most of the congelation growth data point fall below a curve similar to an exponential decay curve. The lower air temperature data points tend to be closer to this curve with the higher air temperature data gathering near the origan. Because data for Figure 4.2b is from the middle of April there is a predominance of thin ice and air temperatures are often low so ice growth rates are high and most of the data points are towards the left-hand side of the figure. Data from later months has more thick ice and lower growth rates. If the congelation growth data is grouped by downward long-wave radiation intensity when plotting against ice thickness the figure looks similar to Figure 4.2b but the data grouping is less distinct.

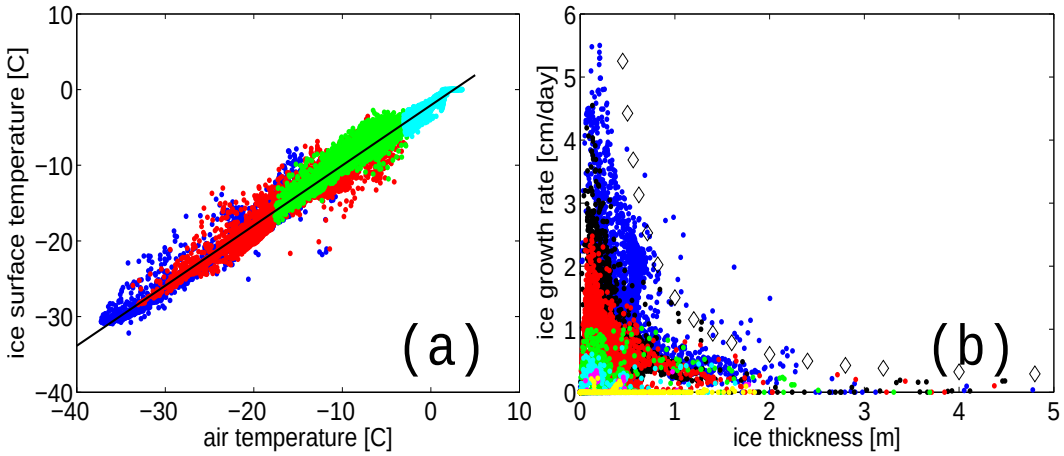

Figure 4.2: Data from 15 April 1998: (a) Correlation between surface temperature and air temperature (for all the data $r^2 = 0.96$, linear fit (black line): $T_{surf} = 0.80 \times T_{air}$ - 2.06, $p < 2.2 \times 10^{-16}$). The colour of the data points denotes the range of downward long-wave radiation with blue < 200 W m^{-2}, red 200-240 W m^{-2}, 240-280 W m^{-2}, cyan >280 W m^{-2}.; (b) Congelation ice growth and ice thickness. The colour of the points indicate the air temperature range: blue <-15 °C, black -15 to -10 °C, red -10 to -5 °C, green -5 to -3 °C, cyan -3 to -1 °C, magenta -1 to 0 °C, yellow >0 °C. The black hollow diamonds are on the curve $y = 1.3 * x^{-1.7} + 0.2$.

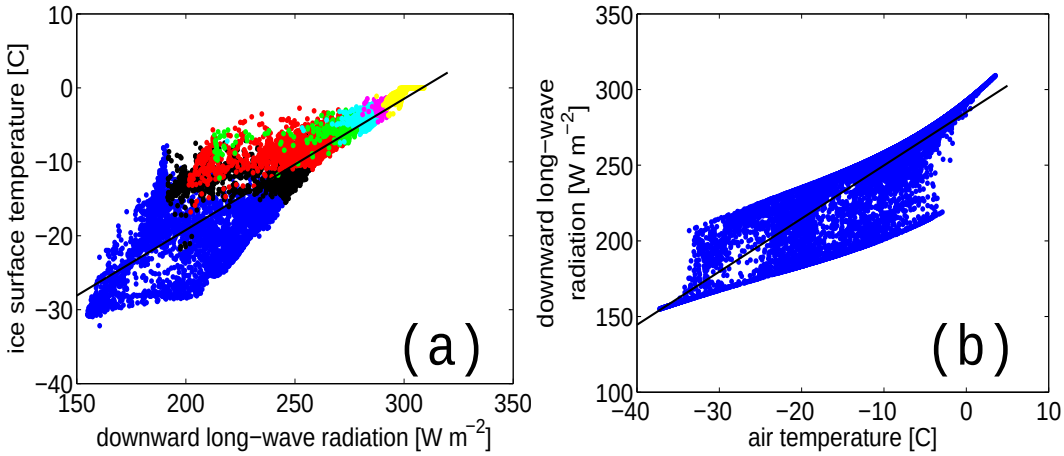

Figure 4.3: Data from 15 April 1998: (a) Correlation between surface temperature and downward long-wave radiation (for all data $r^2 = 0.77$, linear fit (black): $T_{surf} = 0.18 \times$ flwdn - 54.73, $p < 2.2 \times 10^{-16}$). The colour of the points indicate the air temperature range: blue <-15 °C, black -15 to -10 °C, red -10 to -5 °C, green -5 to -3 °C, cyan -3 to -1 °C, magenta -1 to 0 °C, yellow >0 °C.; (b) Correlation between downward long-wave radiation and air temperature (r^2 = 0.77, linear fit (black): flwdn = 3.51 × T_{air} + 284.95, $p < 2.2 \times 10^{-16}$).

Temperatures are generally lower further south but even near the Antarctic coast ice growth rates are low in the thick ice upstream of coastal protrusions but high in the downstream coastal polynyas (Fig. 4.4). The Ross Ice Shelf Polynya is a site of high thermodynamic ice growth which is in agreement with satellite-based estimates (Tamura et al., 2008). There is also

high ice production in the polynyas near Cape Darnley and in the Ronne Ice Shelf Polynya. Ice thickness is low in the lee of islands and this promotes thermodynamic growth in these locations.

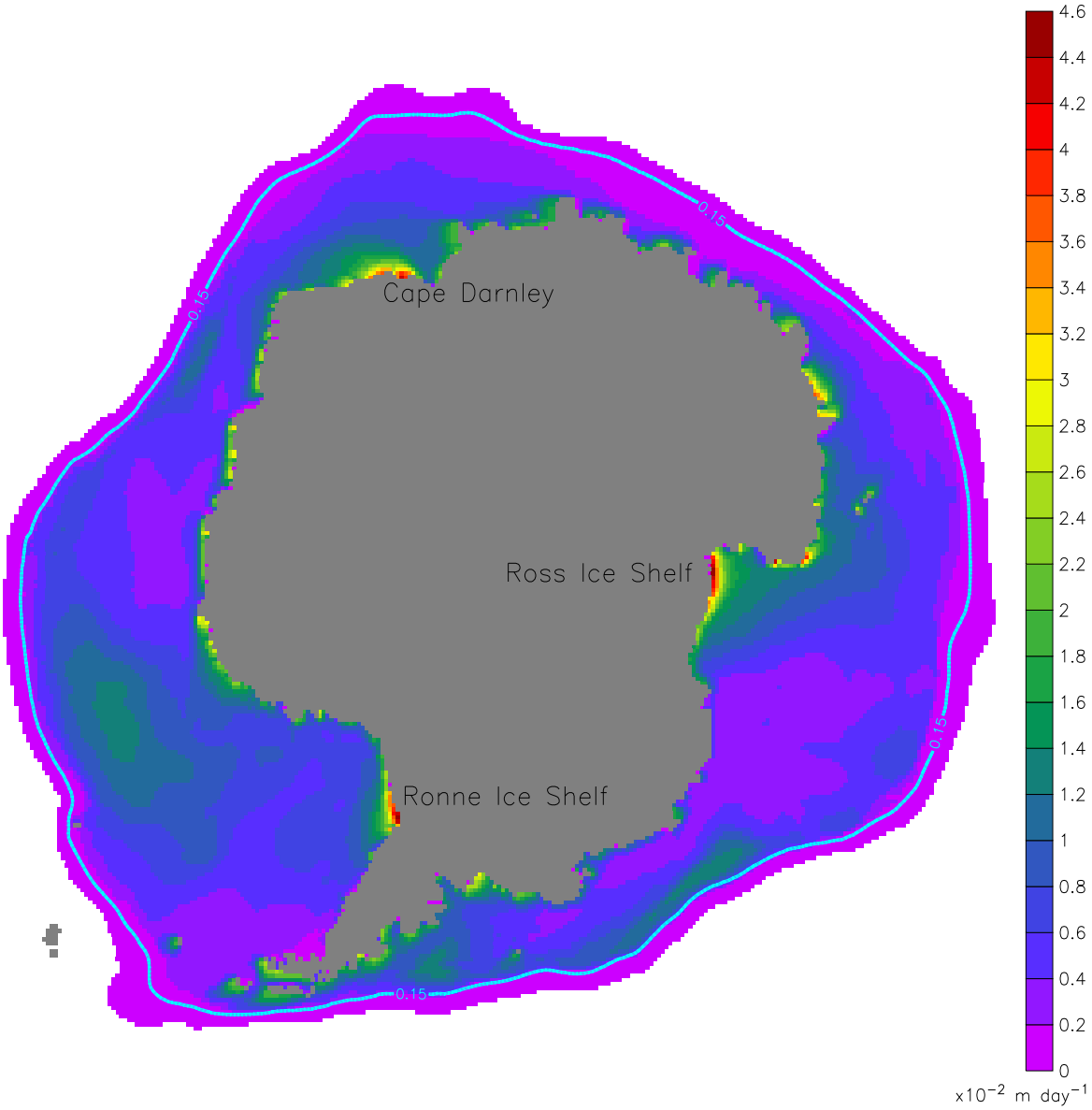

Figure 4.4: Monthly average congelation ice growth (July 2007) on a linear scale. Also shown is the 15% ice concentration contour (light blue). The land mask is grey.

The inverse relationship between congelation ice growth and ice thickness can be seen by comparing figures 4.4 and 4.5. Ice thickness is low in the coastal polynyas where ice production is high. On the upstream side of the coastal protrusions ice thicknesses are high and ice production rates low. There exists in the simulated ice thickness streams of thicker ice leaving the coastal protrusions and carried west by the easterly winds and coastal current. In particular there is a thick stream leaving the Ninnis Bank grounded ice berg / fast-ice tongue at about 150 °E . Some of the ice impacting against this tongue has its origin as far away as the Ross Sea. This ice follows the coast west from the Ross Sea and crosses the Antarctic

Divergence at about 145 °E before being caught in the ACC and moving eastward. There is another region of thick ice in the eastern Ross Sea which is caused by dynamic ice growth as ice interacts with the coast line. Another prominent region of thick ice is on the north-east region of the Antarctic Peninsula. This is a region known to produce thick, multiyear ice (Weiss et al., 2011).

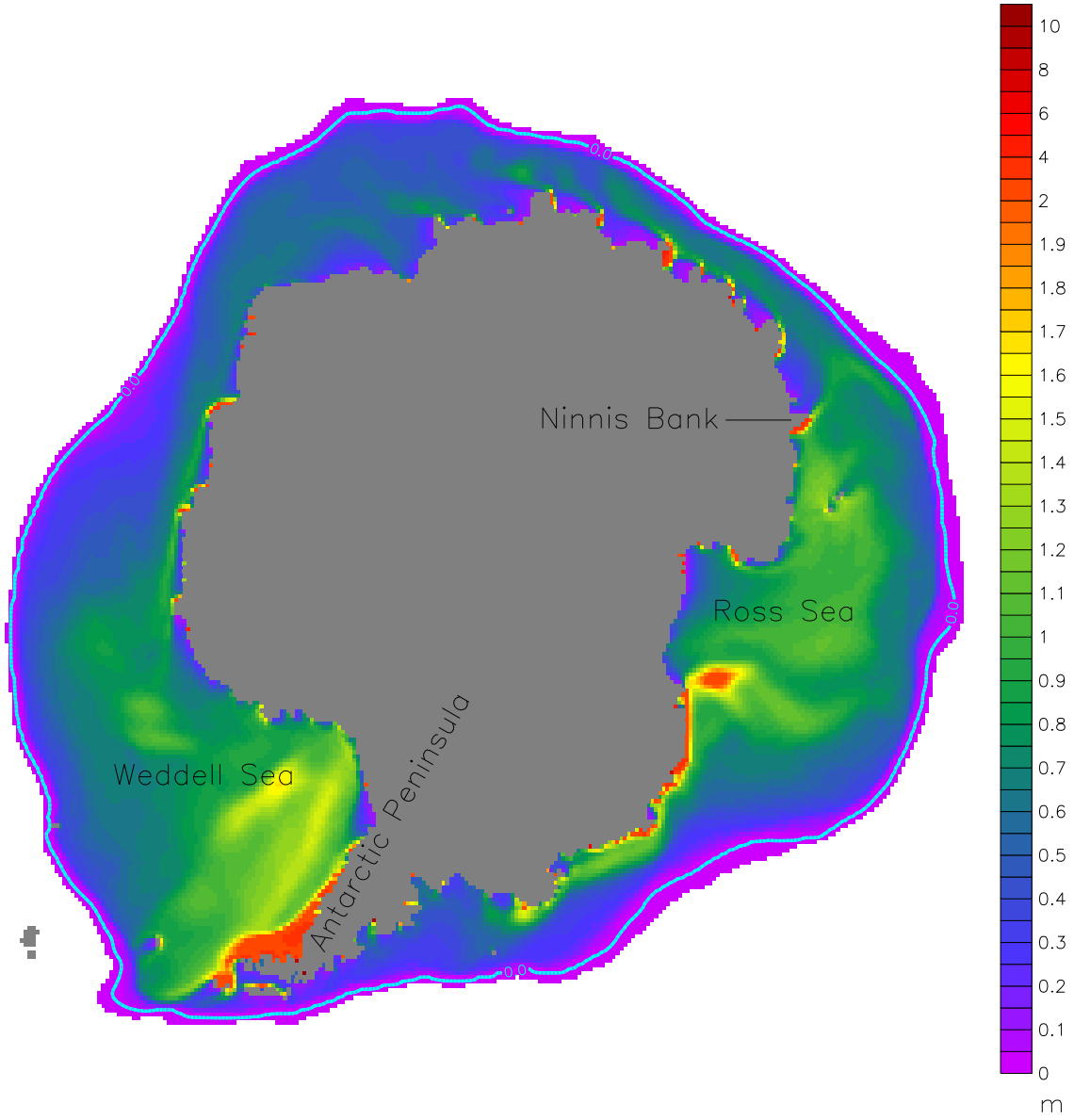

Figure 4.5: Ice thickness on 15 July 2007 on a bi-linear scale, fine resolution from 0 to 2 m and then course to 11 m. The thickest ice is found in small bays which are represented by one or two grid cells and are an artefact of the model because ice cannot advect out of these bays. Also shown is the 15% ice concentration contour (light blue). The land mask is grey.

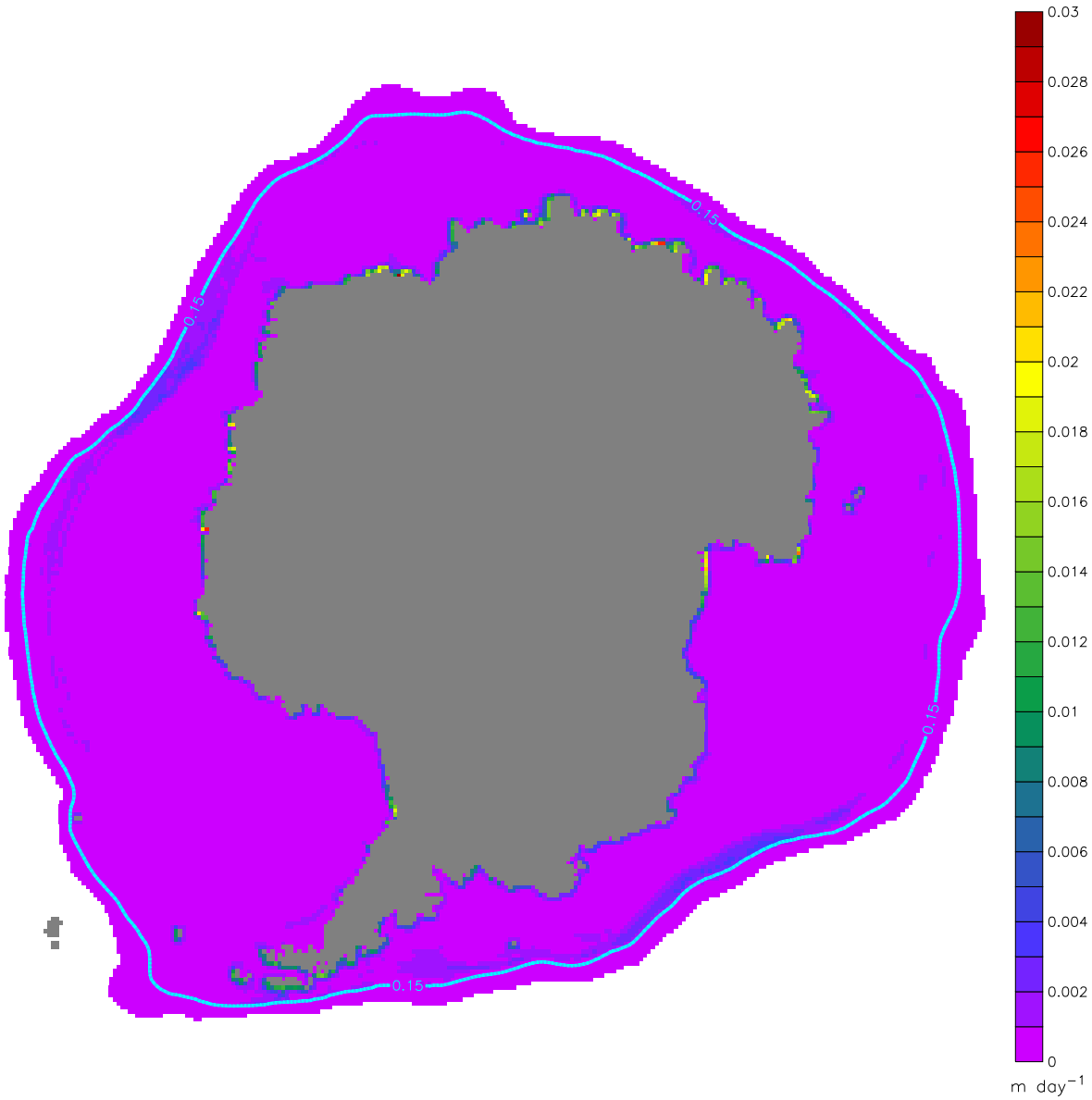

Figure 4.6: Monthly average frazil ice growth (July 2007). Also shown are ice thickness contours (black) and the 15% ice concentration contour (light blue). The land mask is grey.

In reality, Southern Ocean coastal polynyas are sites where frazil ice production dominates. This is because strong katabatic winds move any ice at the surface ice down-wind and agitate the surface water through wave action keeping frazil crystals in suspension (de la Rosa and Maus, 2011). Despite CICE4 underestimating frazil ice growth, coastal polynyas in our simulations are sites of relatively high frazil ice production because of the higher open water fraction that is produced when the polynya is active (Fig. 4.6). Outside the coastal polynyas but adjacent to the coast there is a region where monthly average frazil ice growth is elevated. This coastal region has high average shear which promotes lead opening and hence frazil ice growth. In the sea ice pack generally there is very little simulated frazil ice growth because ice concentration is high. Further north there is more open water and higher frazil production in some regions a little south of the 15% ice concentration contour (Fig. 4.6).

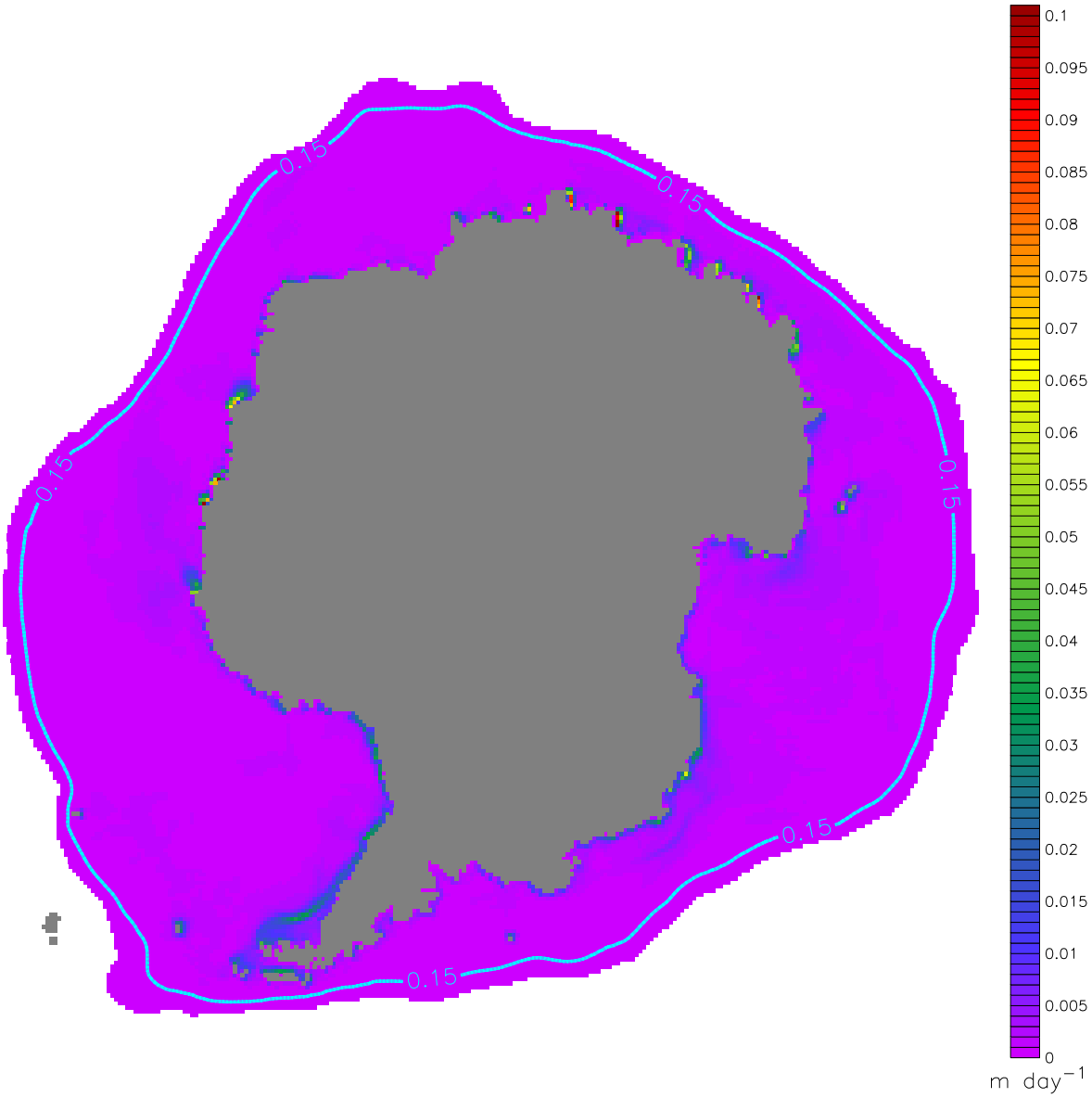

Figure 4.7: Monthly average dynamic ice growth (July 2007). Also shown is the 15% ice concentration contour (light blue). The land mask is grey.

Dynamic ice growth in CICE4 makes the second greatest contribution to increasing ice thickness after congelation ice growth. Dynamic ice growth is growth only in ice thickness as it does not produce new ice by the freezing of sea water. Dynamic ice growth has maxima on the up-stream side of coastal protrusions where ice convergence is greatest and ice concentrations are high (Fig. 4.7). Dynamic ice growth is also elevated in the high shear region adjacent to the coast. Islands also interrupt ice advection and are locations of enhanced dynamic ice growth.

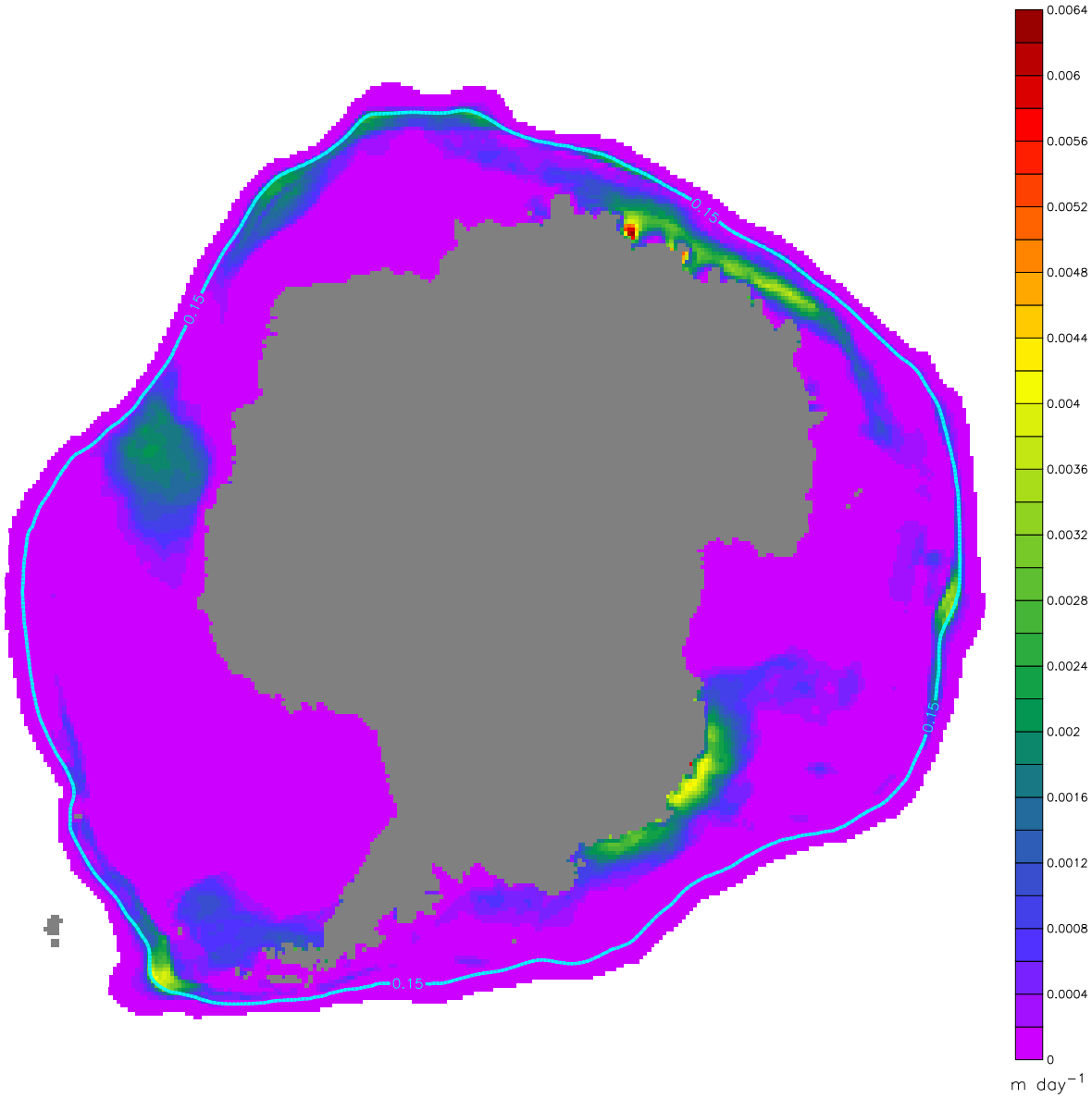

Figure 4.8: Monthly average snow-ice growth (July 2007). Also shown is the 15% ice concentration contour (light blue). The land mask is grey.

Snow-ice is the last ice growth process in CICE4. On average its contribution is largest in regions of high precipitation such as the Bellingshausen and Amundsen seas (Fig. 4.9) and where sea ice is thin such as near the ice edge (Fig. 4.8). Over shorter time scales snow-ice production is episodic and correlates with snow-fall events if the ratio of snow thickness to ice thickness is close to 0.33 (Fig. 4.10a). When basal melt rates are high the snow–ice interface can be lowered to the sea surface at which point the snow-ice production rate will correlate with basal melt rate. This can be see near the 15% ice concentration contour just north and east of the Antarctic Peninsula (Fig. 4.8). The ice at this location is not particularly thin (Fig. 4.5) but basal melt rates are high due to strong northward advection of ice. When the snow thickness to ice thickness ration equals 0.33, as it often does in summer, the snow-ice production rate follows the diurnal cycle of the basal melt rate during time intervals of no snow-fall (Fig. 4.10b). Note also that snow-ice can form when the ratio of snow to ice

thickness is less than 0.33.

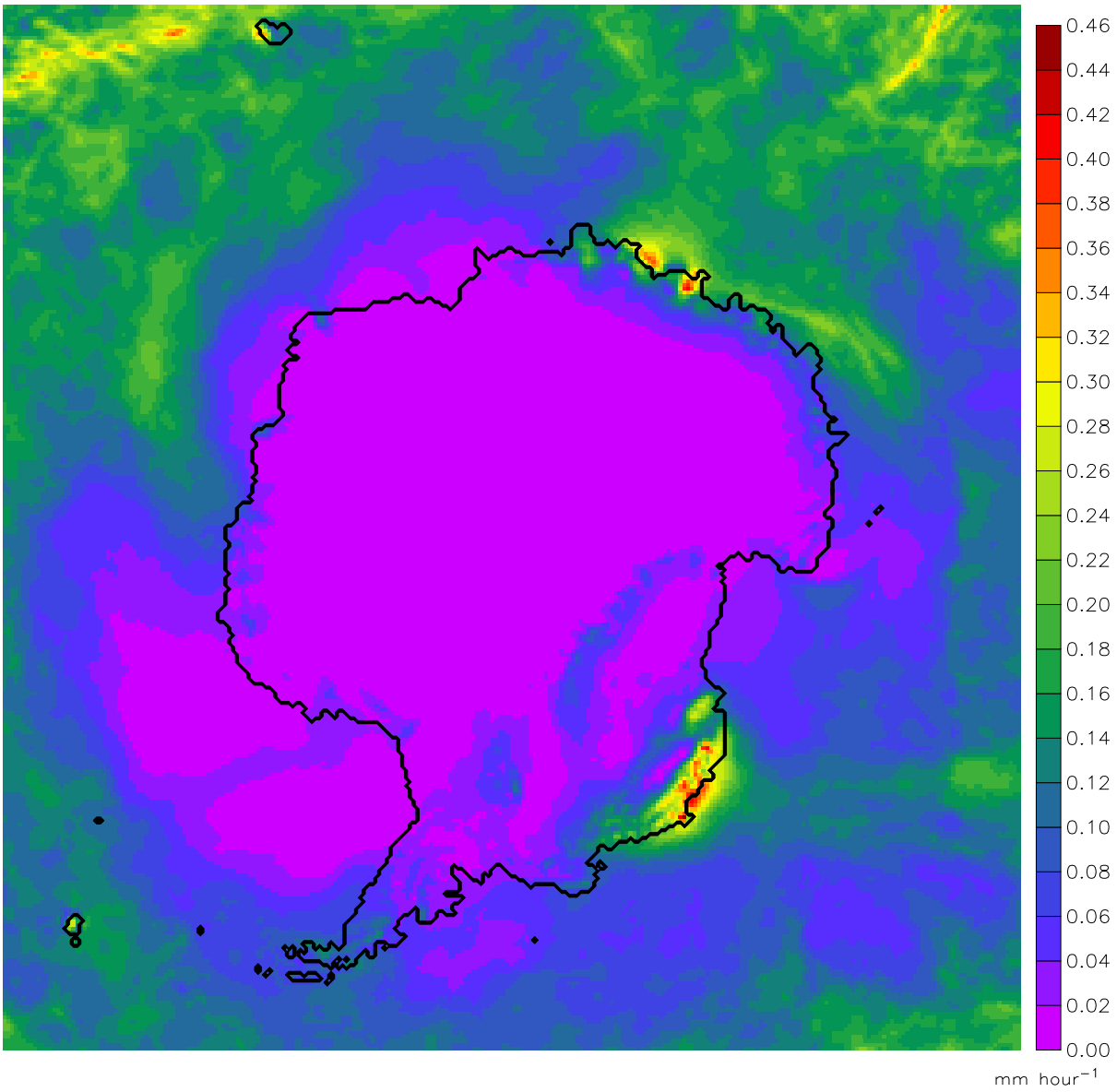

Figure 4.9: Monthly average precipitation (July 2007) from PolarLAPS. Also shown is the Antarctic coastline (black).

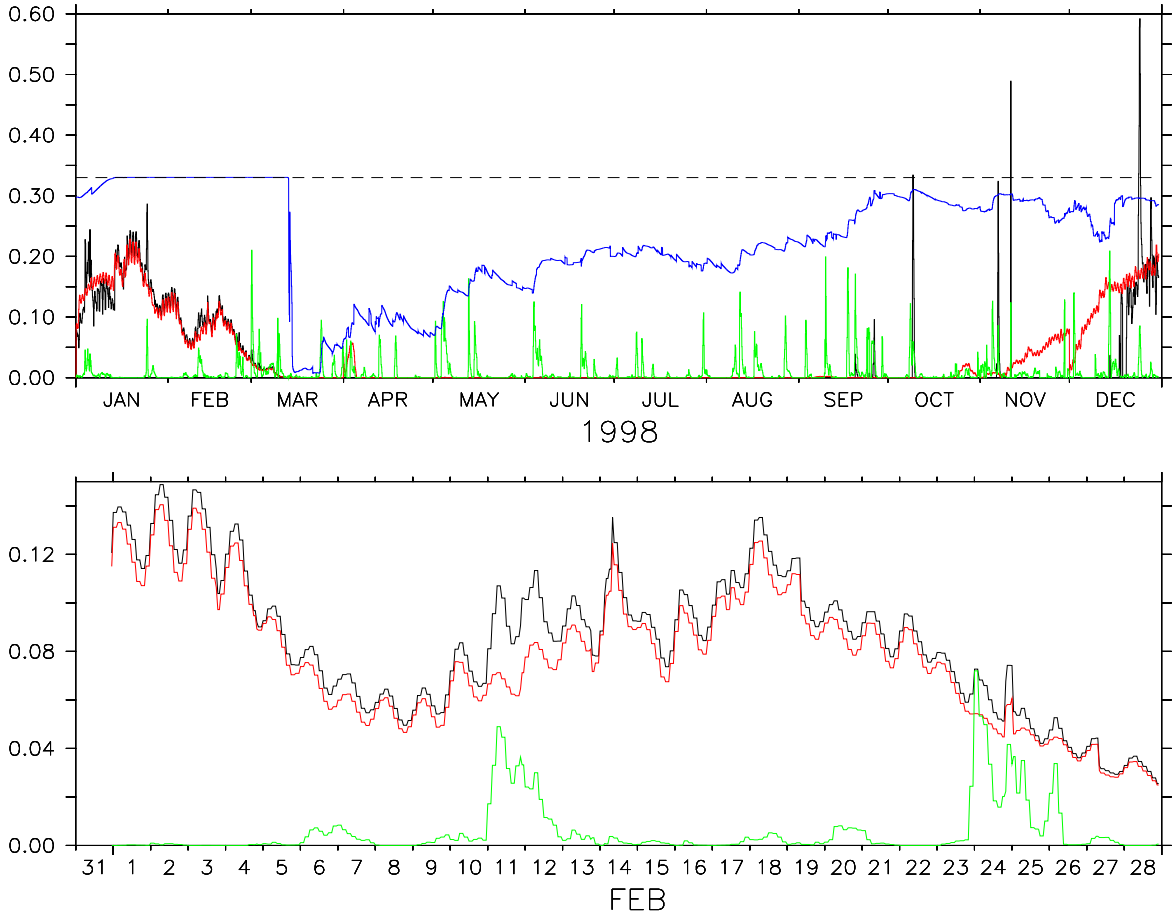

Figure 4.10: Snow-ice production (black) in cm day^{-1} for virtual ice buoy 7 released at 200 °E and 74.5 °S on 1 January 1998. (a) 1 January to 31 December. (b) 1 to 28 February. Also shown is snow-fall divided by 10 (green) in cm day^{-1}, basal melt divided by 10 (red) in cm day^{-1}, and the snow thickness to ice thickness ration (blue). The black dashed line is the snow density to ice density ration of 0.33.

4.2.2 Ice decay

There are three ice decay mechanisms in CICE4. Of these basal melt is dominant, accounting for 88% of annual melt. The next largest is top melt at over 11% of total annual melt and lastly lateral melt at less than 1%. All decay mechanisms are greatest in summer, which is not surprising. What is a little more unexpected is that decay values greater than zero are found in the middle of winter (Fig. 4.11).

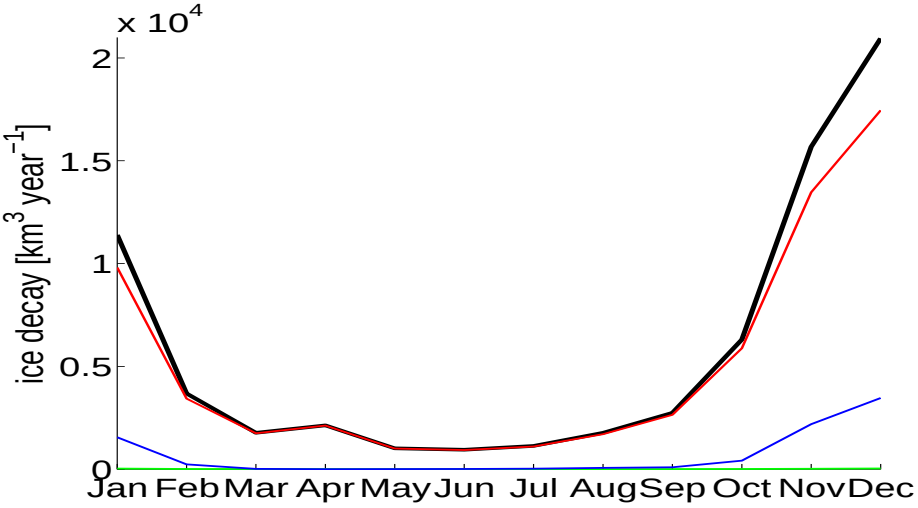

Figure 4.11: Monthly ice decay by type, average for 1998 to 2008. Decay volume total (black), basal melt (red), top melt (blue), lateral melt (green).

Basal melt is present throughout the year because there are regions where ice is advected northwards into water above freezing. One such region is located about 80 °E (Fig. 4.12). In this location persistent southerly winds reinforced by ocean currents cause ice to advect northwards driving the ice edge northwards also. Early in the ice growth season there is very little basal melt and what there is occurs in a narrow band with its maximum corresponding to the 15% ice concentration contour (not shown in Fig. 4.12a). As the ice decay season begins the width of the band of enhanced basal melt increases and tends to move south of the 15% ice concentration contour. By December, when basal melt is greatest, the band of melt has expanded further until melt is occurring under most of the pack (Fig. 4.12b).

Top melt is greatest in spring and summer when air temperatures and radiation fluxes are at a maximum. In autumn and winter top melt is effectively zero. In December, when top melt is at a maximum, maximum rates occur just south of the MIZ.

Lateral melt plays a very minor part in simulated ice decay. It has a similar spatial distribution to basal melt and a similar evolution throughout the year.

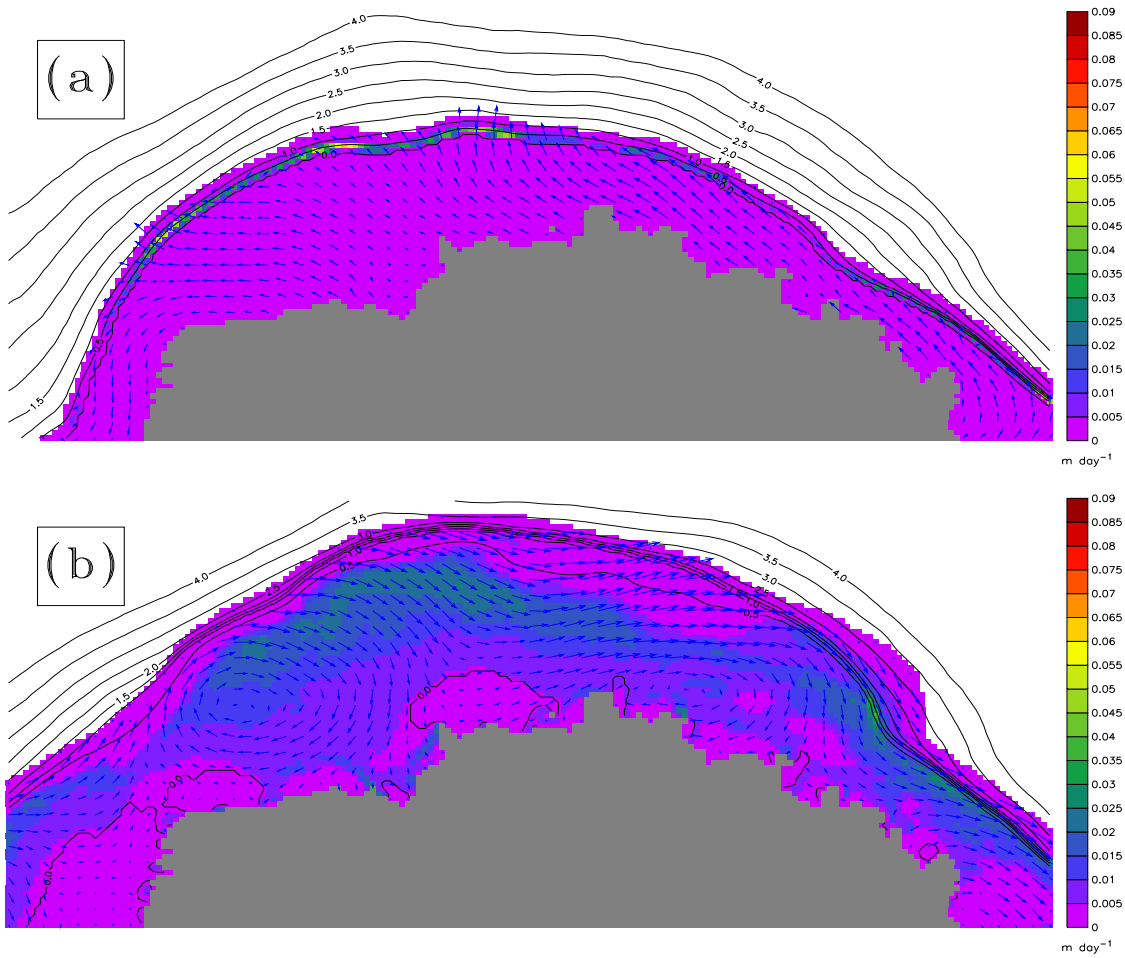

Figure 4.12: Examples of basal melt centred on 90 °E on: (a) 2 June 2008; (b) 4 December 2008. Also shown is the surface temperature of the ocean above the local freezing point (black) and the ice velocity vectors (blue). The land mask is grey.

4.3 Variability of total ice area and total ice volume

When averaged for the years 1998–2008 simulated Southern Ocean total sea ice area has a seasonal cycle with a minimum on 18 February and a maximum on 20 September (Fig. 4.14a). January is the month with greatest interannual variability in total ice area and July has the least. Simulated total ice volume has a similar cycle but changes lag total ice area, with minimum volume occurring on 7 March and the maximum on 11 October (Fig. 4.14a). Maximum interannual variability in total ice volume occurs in January and October has the least. Daily average ice thickness is obtained by dividing the daily total ice volume by daily total ice area (Fig. 4.14b). Average ice thickness has a maximum on 2 February and a minimum on 3 May. Maximum interannual variability in average ice thickness occurs on 4 February and is least on 25 September.

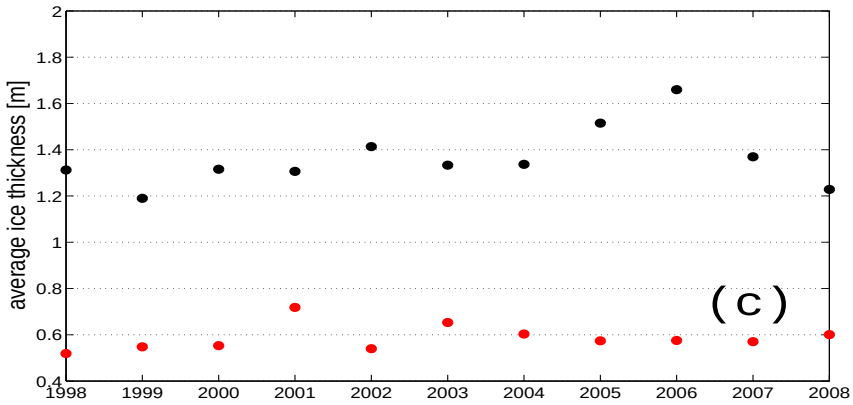

Figure 4.13: Average ice thickness at ice minimum (red) and ice maximum (black).

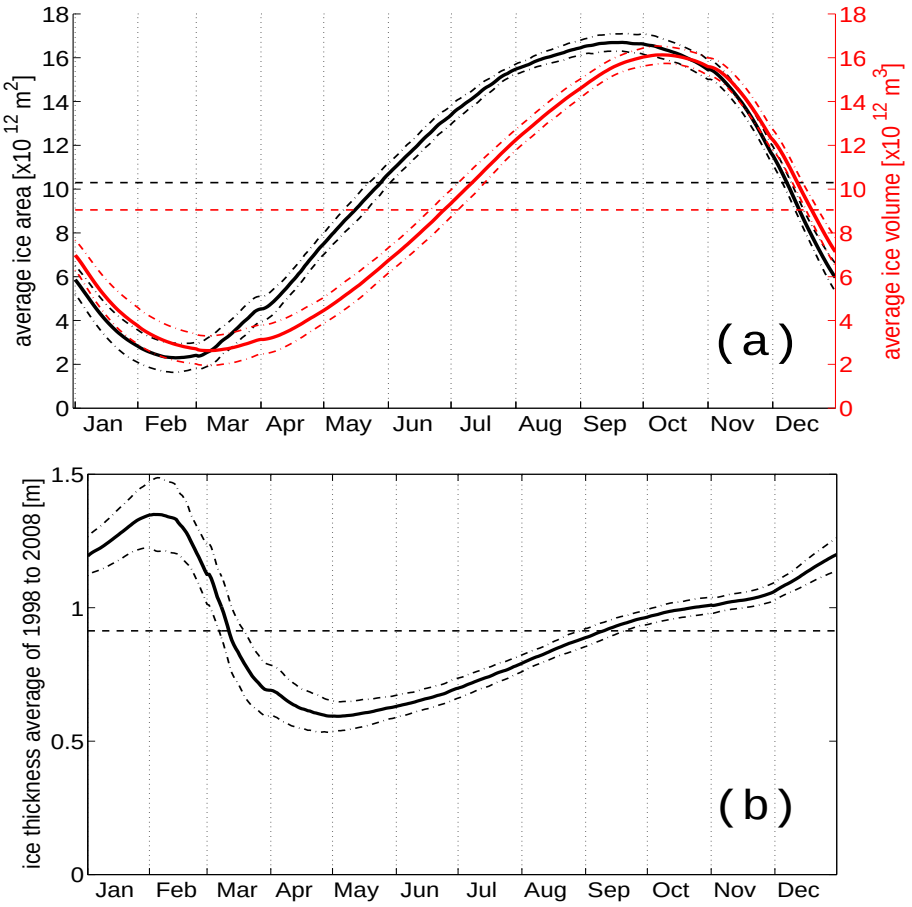

Figure 4.14: 1998 to 2008 average. (a) Daily total ice area (black) and volume (red) with ±1 standard deviation (dot-dashed) and annual average area (black dashed) and volume (red dashed). (b) Average thickness with ±1 standard deviation (dot-dashed) and annual average (dashed).

That maximum average ice thickness should occur in summer seems counterintuitive. It would seem more logical that sea ice would be thinner in summer when most melting occurs. The key to understanding this is to remember that it is average ice thickness and that this is

obtained by dividing the total ice volume by the total ice area and open water is not considered. Let us imagine that 90% of the area was 0.5 m thick and that 10% was 2 m thick which gives an average thickness of 0.65 m. Now if there is melting that accounts for a uniform 0.5 m of ice then all the 0.5 m ice will have melted and there only remains the thick ice which is now 1.5 m thick. But the 1.5 m thick ice is now 100% of the ice so the average ice thickness has increased from 0.65 to 1.5 m even thought ice of all initial thicknesses has thinned. This effect would be a lot less apparent in the Arctic Ocean where there has been little thin first year ice. However, the Arctic Ocean appears to becoming more like the Southern Ocean where most ice melting each summer. So in the future it is likely that the Arctic Ocean sea ice will exhibit this counterintuitive behaviour.

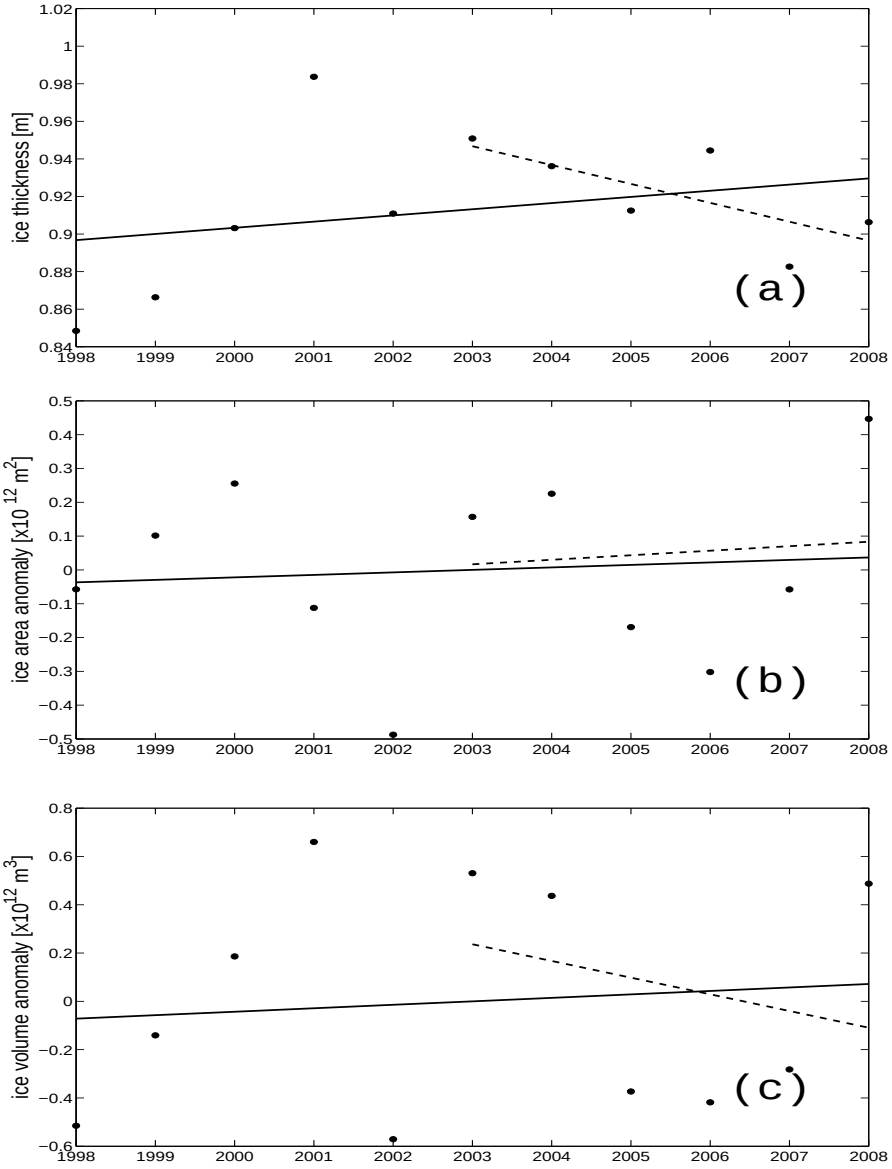

Figure 4.15: Trends in annual averages for: (a) ice thickness; (b) ice area; (c) ice volume for time intervals 1998–2008 (solid) and 2003–2008 (dashed).

At ice minimum there is a small positive trend in ice thickness of 0.6% per year (Fig. 4.13) but this is not significant ($p = 0.5957$, $R^2 = 0.03$). At ice maximum the thickness trend is

larger (1.2% per year) but is still not significant ($p = 0.2423$, $R^2 = 0.15$).

At ice minimum the total ice area is only 16% of that at ice maximum. This large seasonal cycle makes the notion of an annual average of limited value other than to collapse the annual cycle into a single value which can be used to look for interannual trends (Fig. 4.15b). Similar annual averages were calculated for ice thickness (Fig. 4.15a) and ice volume (Fig. 4.15c). Trends in annual average total ice area are slightly positive for the full eleven years of the simulation (0.07% per year) and for 2003–2008 a little more positive (0.12% per year). However, these trends have a high probability of occurring due to normal interannual variation ($p = 0.79$ and 0.86 respectively) and so are not significant. Annual average total ice volume has a positive trend for time interval 1998–2008 (0.17% per year) but a negative trend for interval 2003–2008 (-0.72% per year). Volume trends are also not significant ($p = 0.77$ and 0.59 respectively). Annual average ice thickness has a positive trend for time interval 1998–2008 (2.11% per year) but negative for 2003–2008 (-1.55% per year). Annual average ice thickness trends are not significant at 95% confidence but the 2003–2008 trend just fails at 90% confidence ($p = 0.11$) but the 1998–2008 trend is not significant ($p = 0.41$).

There exists a best fit linear correlation between annual average total ice volume and annual average total ice area (Fig. 4.16a). The coefficient of the correlation is 1.20 [m] and the correlation is significant at 95% confidence ($p = 0.0184$, $R^2 = 0.48$). There exists a highly significant linear correlation between total ice volume and total ice area at ice minimum (Fig. 4.16b, $p < 0.0001$, $R^2 = 0.88$) but not at ice maximum ($p = 0.2777$, $r = 0.36$). By month the correlation exists as follows: January–March at >99% confidence; April at 99% confidence; May and June at 95% confidence; July–October no significant correlation; November and December at 95% confidence. The month with the highest p-value is October and the lowest R^2 occurs in September.

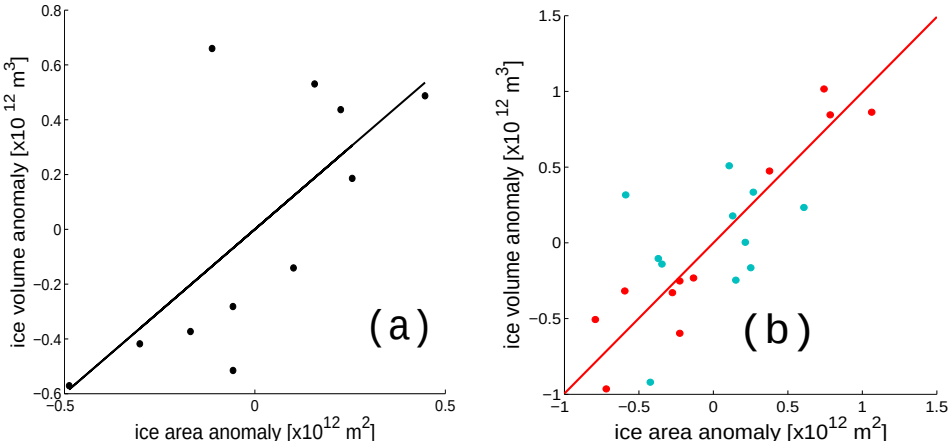

Figure 4.16: Ice volume anomaly versus ice area anomaly: (a) annual average; (b) at ice minimum (red) and ice maximum (blue).

4.4 Determination of the ice-edge location

This section examines the contributions of ice advection and *in situ* thermodynamic growth of ice to the location of the ice edge. It expands on and supersedes the work presented by Stevens and Heil (2010) because it has a higher zonal resolution (1° instead of 10°) and uses

data from all years of the 11-year simulation. The months included in the analysis are April to December for all years 1998 to 2007 and April to November for 2008. The approach followed is that if the northward expansion rate of the ice edge is greater than the northward ice velocity at the ice edge, then thermodynamic ice growth determines the location of the ice edge, i.e. thermodynamic expansion of the ice edge is out-pacing the northward advection of ice. On the other hand, if the northward ice velocity is greater than the northward expansion rate of the ice edge then it is ice advection that determines the location of the ice edge, i.e. the edge location can only be maintained/advanced by ice advection. It should be noted that northward ice advection is generally associated with southerly winds, which occur mostly at a lower temperature than northerly winds and are therefore likely to promote thermodynamic ice growth. Despite this complication it is possible to distinguish thermodynamically dominated zones from advection dominated zones.

For thermodynamic ice growth to occur the mixed layer must be near the ocean freezing point temperature. Ice can advect quicker than the time it takes to cool the mixed layer to the freezing point so in advection-dominated zones ice enters water above the freezing point. This causes the ice to melt which in turn cools the mixed layer. It is ice advection that enables any thermodynamic ice growth near the ice edge in the advection-dominated zones by conditioning the mixed layer to the freezing point. Also the ice thickness profile of a north-south transect is quite different in a thermodynamically dominated sector, i.e. the ice starts thin at the edge and grows gradually thicker as the transect progresses south. An advection dominated sector has a rapid increase in ice thickness near the ice edge so that thickness is close to the values found further south. The rapid increase in ice thickness near the ice edge is caused by the high melt rates that occur in these zones (Fig. 4.17).

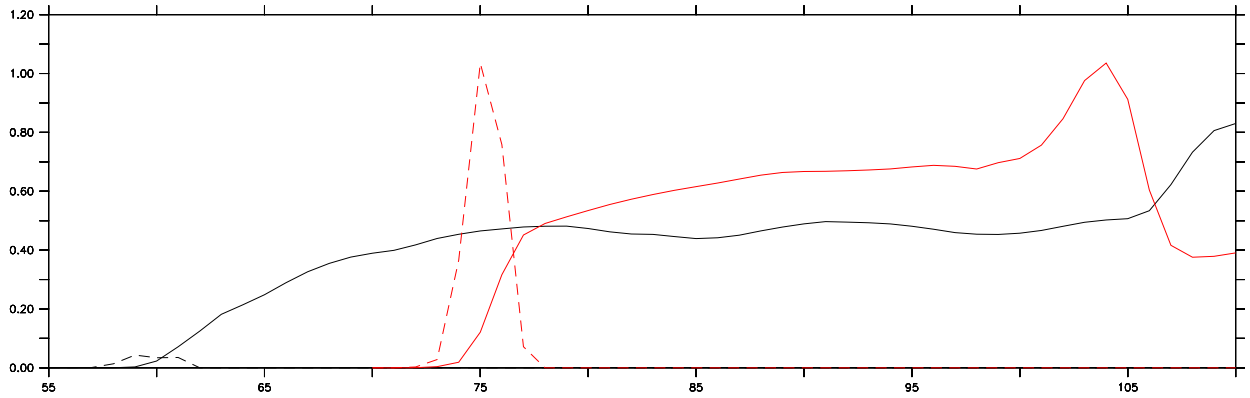

Figure 4.17: Ice thickness transects at the thermodynamically dominated longitude 30 °E (black solid) and the advection dominated longitude 85 °E (red solid). The y-axis units are metres. Also shown is the basal melt rate (dashed) divided by 3 (cm day^{-1}). Horizontal axis is a measure of distance but can not be compared because they have different scales and therefore the units have not been added.

April to December were the months examined because there is ice in almost all longitudinal zones for these months. During the January to March time interval ice is largely restricted to the deep embayments and the ice edge is difficult to define (using automated methods) because of open water areas within the deep embayments. However, April to December includes a sample from all four seasons. The Antarctic Peninsula zone was excluded from the analysis

because there is little or no ice north of the Peninsula and because the Peninsula can cause the ice edge to have large north-south segments which confuse the analysis, due to the assumption that the edge runs mostly east-west.

The northward expansion rate of the ice edge was quantified by defining an ice concentration which is taken to be the edge (15% in this case) and calculating the distance the edge moved over a time interval of nine days. Nine days was chosen for two reasons: 1. it produced measurable edge displacements; 2. it is longer than the lifetime of most atmospheric low pressure systems and so the measurements will have less local variability due to short-term weather. The northward expansion rate of the ice edge was calculated by dividing the distance the edge moved north by the time interval. The calculation was done at 1 ° longitudinal intervals and at 1 day time steps.

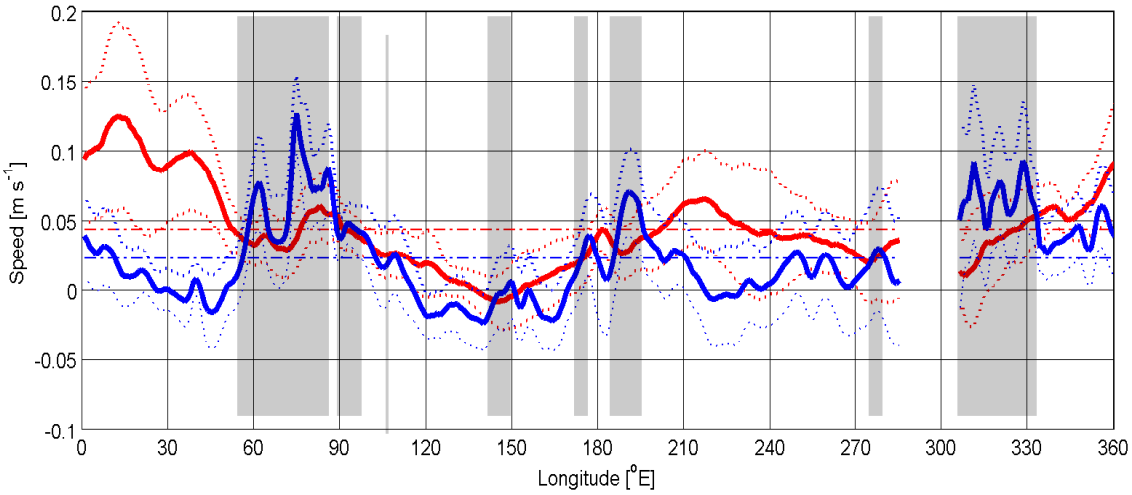

Figure 4.18: July northward speed of ice edge (thick red) and July northward ice velocity (thick dark blue) averages for 1998 to 2008. Also shown ±1 sample standard deviation (thin dotted) and the zonal average (thin dot-dashed). The zones where the northward ice velocity is greater than the northward ice edge speed are marked by grey rectangles.

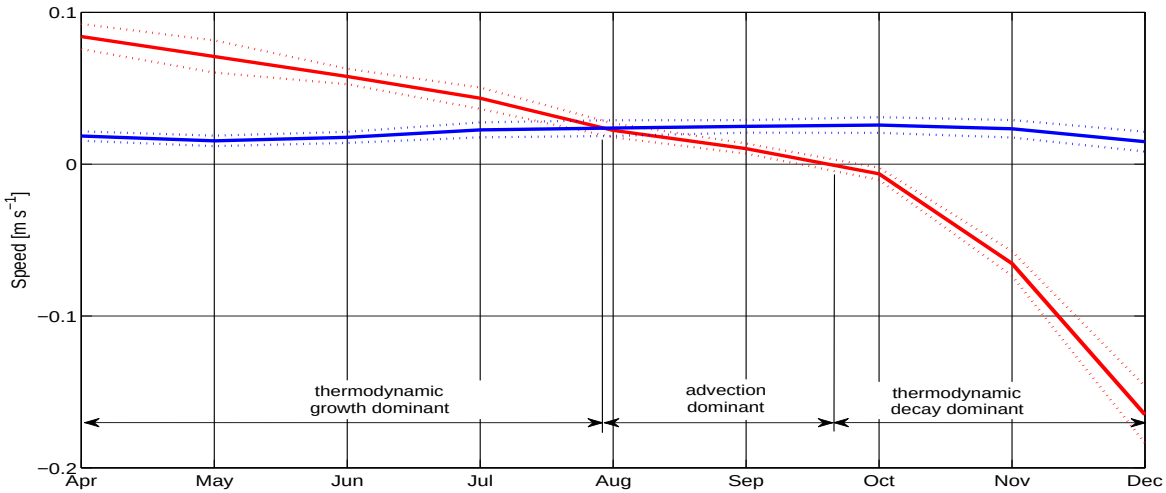

Figure 4.19: Zonal, monthly average rate of expansion of the ice edge to the north (thick red solid), northward ice velocity at the ice edge (thick dark blue solid), with ±1 sample standard deviation (thin dotted).

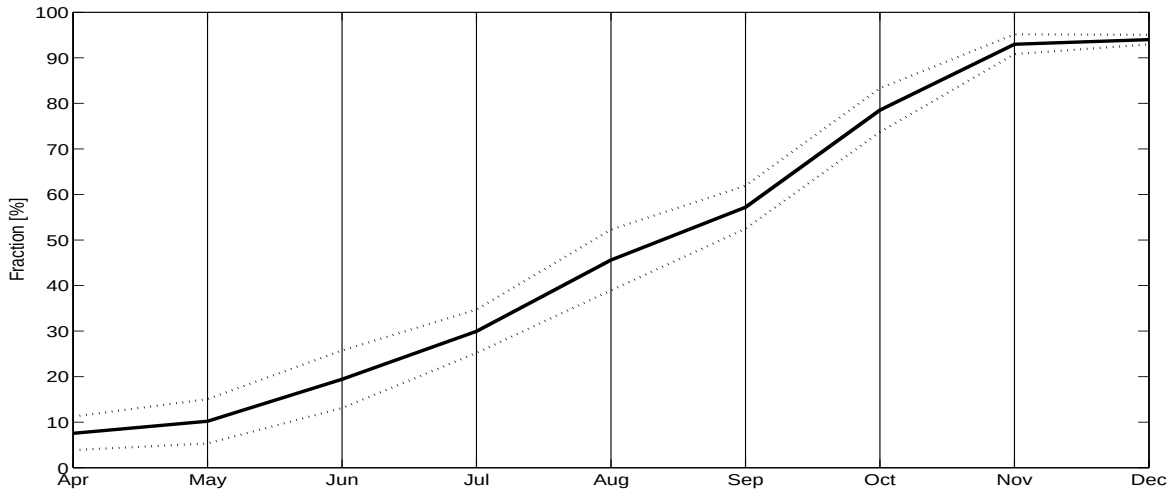

Figure 4.20: Zonal, monthly average of the fraction of 1° longitudinal segments where the northward ice velocity at the ice edge is greater than the expansion rate of the ice edge speed to the north (thick solid), with ±1 sample standard deviation (thin dotted).

4.5 Model predictions for changed climate

Numerical models are an important tool for estimating future climates and the effect that a changed climate might have on natural systems such as Southern Ocean sea ice. Here an attempt is made to simulate Southern Ocean sea ice using forcing that has average values that are consistent with the IPCC Fourth Assessment Report predictions for the Earth's climate in 2100. The most complete set of projected values available was for the A1B scenario and the forcing for these simulations was based on this scenario.

For this research CICE4 was run stand-alone and no 2100 projected forcing was available. So the existing forcing was used with an offset value or multiplied by a suitable coefficient that reflected changes that are projected to occur during this century. This produces forcing with the projected average changes but not necessarily with the correct spatial distribution. For example, the projected increase in air temperature in the northern Southern Ocean (1.0–1.5 °C) is much less than the global average increase (2.8 °C) but in the Southern Ocean sea-ice zone the increase is closer to the global average (about 2 °C) (Solomon et al., 2007) chapter 10, figure 10.8. The forcing offset that approximates the sea-ice zone average increase was applied to the forcing even though it will be too large for the northern regions of the model domain. The projected changes also vary with season and where offset values for different seasons were available they were used. Air temperature was one such forcing field with the December–February projected increase being 1.2 °C while the June–August increase is projected to be 3 °C. Between these two time intervals the air temperature offset was calculated by linear interpolation.

Besides air temperature the fields that had an offset applied were: precipitation (+0.2 mm day^{-1}), cloud fraction (+1.5%), surface air pressure (-2.3 hPa), wind strength (+25%), long-wave downward radiation (+12 W m^2), air humidity (+20%). The field that was not changed was surface ocean currents which may increase with increasing wind strength. For the Antarctic Circumpolar Current (ACC) at least the predictions of increased volume transport are uncertain. Some models predict a significant increase (Fyfe and Saenko, 2005), other eddy-permitting models predict a modest increase with increased eddy flux (Downes et al., 2011),

and other eddy-resolving models predict an increase in eddy flux rather than volume transport due to a state of "eddy saturation" in the ACC (Hogg et al., 2007). But in the westward coastal drift, which is not eddy saturated, an increase in wind forcing would produce an increase in current volume transport. Katabatic winds from the Antarctic Continent are at least partly responsible for the westward drift current and how these winds will change in the projected climate is uncertain.

For the optimized simulations of the control runs the winter modelled total ice area is very close to the passive microwave-derived total ice area. When the A1B scenario offsets are applied the winter total ice area is typically about 80% of the corresponding passive microwave-derived area (Fig. 4.21 and 4.23). This is partly caused by a reduced ice extent and partly because of lower ice concentrations within the pack. In summer CICE4 often underestimates the total ice area, e.g. for 1998 total ice area minimum occurs on 2 March when the model produces 73% of the passive microwave-derived area. However, with the A1B scenario offsets applied the modelled total ice area is only 2% of the passive microwave-derived area at ice minimum (Fig. 4.21 and 4.22). The eleven year average ice minimum occurs earlier in February when compared to the present day, i.e. from about 24 February to about 12 February. On February 12 ice with concentrations higher than 15% only remain in south of the Weddell Sea and on the up-stream side of East Antarctic coastal protrusions (Fig. 4.22), i.e. some at Riiser-Larsen, a little at 115 °E, but most at the grounded iceberg/fast-ice over the Ninnis Bank at about 150 °E . The ice at 150 °E is also the thickest at almost 4 m (Fig. 4.22). In other simulations with an even warmer climate than for the A1B scenario it was found that this is the only location where ice remains at ice minimum (not shown).

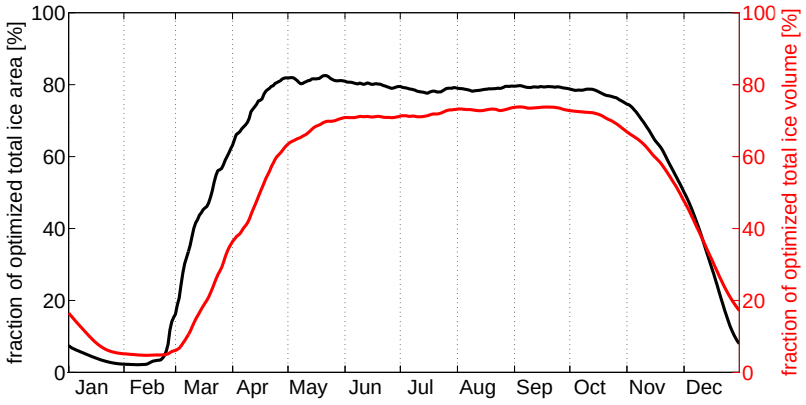

Figure 4.21: IPCC AR4 A1B projections for 2100 forcing offsets as a fraction of the optimized simulation. Daily total ice area (black) and total ice volume (red). The offsets were applied to the 1998 forcing data.

Satellite-derived total ice volume estimates are only just becoming available. So it was not possible to compare the estimates of total ice volume to satellite derived volumes as was done for total ice area. However, it was possible to compare the volume in the optimized simulation estimate to the A1B scenario estimate. In winter the A1B scenario simulation produces about 70% of the optimized simulation total ice volume. In summer the corresponding fraction is ≈5% (Fig. 4.21).

To investigate the impact of the various components of the IPCC AR4 A1B scenario forcing, simulations were run with all but one field set for the A1B configuration and the last field set

to that of the optimum values of the control simulation. For want of a better name this set of simulations were called the "all-but-one" runs. The impact was measured by the fraction of the control simulation that was restored by using one field at the optimum setting. Changes in both total ice area and total ice volume were calculated and the results are summarized in Table 4.1. All but one of the fields have the same sign and indeed similar restored fraction values for both total ice area and total ice volume. The exception is precipitation where reducing it to the optimum value reduces the total ice area a small amount but increases the total ice volume. The fractional change in total ice area and volume is the annual average but its value varies with season (not shown). In all cases but one the largest impact is in summer. The exception is wind speed which when restored to the optimum value causes the largest decrease in ice area and volume in winter.

Field set to optimum (control simulation) i.e. not to A1B value	A1B scenario value for field	Annual average of fraction of optimum total ice area [%]	Annual average fraction of optimum total ice volume [%]
air temperature	+1.2 °C (summer) to +3 °C (winter)	20.17	24.80
specific humidity	×1.20	6.50	8.12
downward long-wave radiation	+12 W m^{-2}	4.36	4.97
surface air pressure	+230 Pa	0.00	0.00
precipitation	0.192 mm day^{-1}	-0.07	0.88
cloud fraction	+1.5%	-0.14	-0.09
wind speed	×1.25	-4.13	-5.35

Table 4.1: For each of the fields that were altered to make their values compatible with the IPCC AR4 A1B scenario for 2100 one at a time was set back to the optimum values while the rest remained at the A1B values. The one field that was set to the optimum is in the left hand column and the next to the right lists the offset that would have been applied to make it the A1B values. The restoring ability of the field being examined is measured by the fraction increase [%] of total ice area and volume compared to those of the optimum simulation. The fields are listed from those that restore the most total ice area to those that restore the least. Using optimum values for precipitation, cloud fraction and wind speed actually reduced the total ice area.

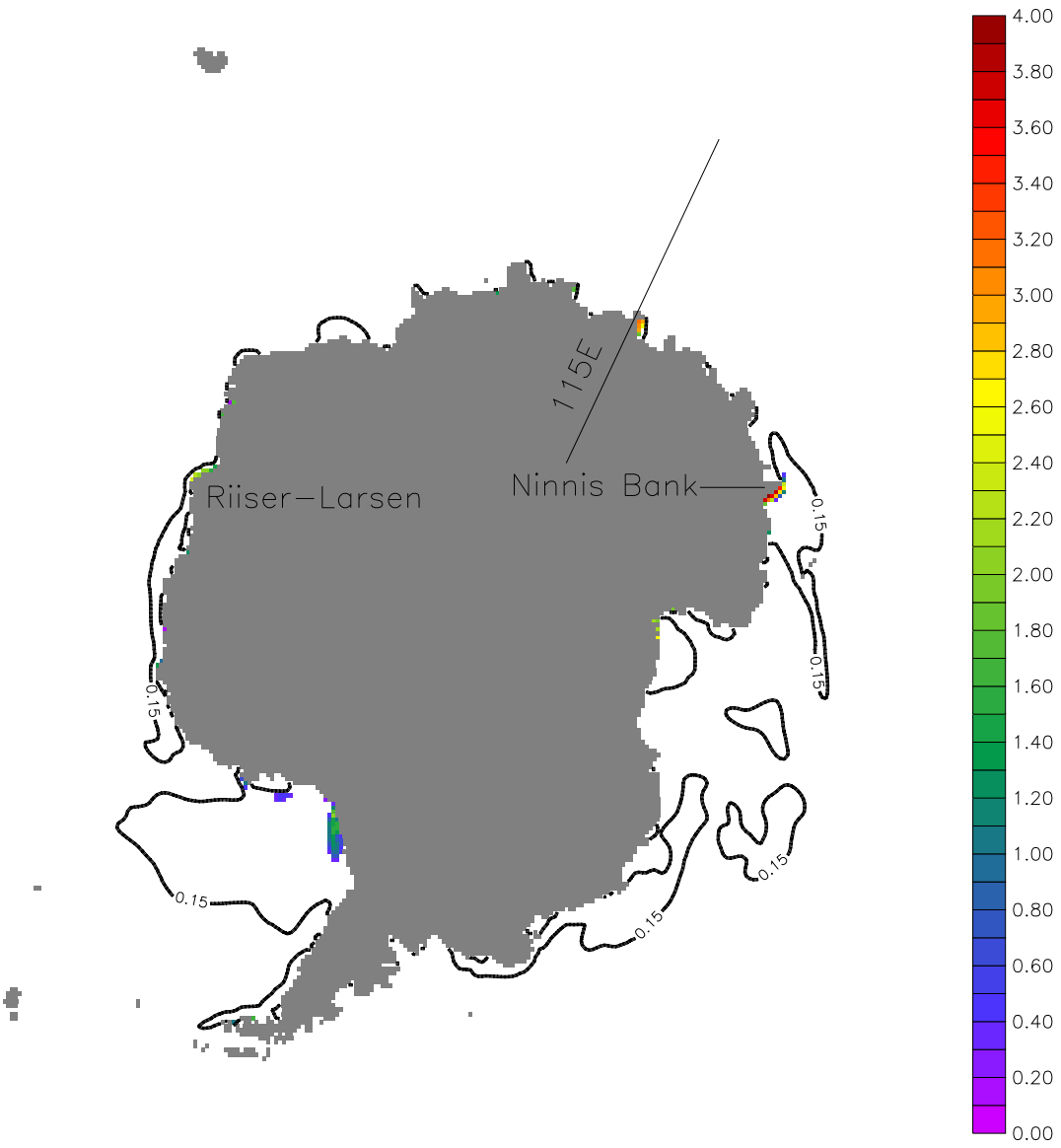

Figure 4.22: Ice thickness at ice minimum where ice concentrations are at least 15% for simulation using forcing offsets consistent with IPCC AR4 A1B scenario projections for 2100. Also shown is the 0.15% ice concentration contour from the optimized simulation (black). Land mask is grey. The offsets were applied to the 1998 forcing.

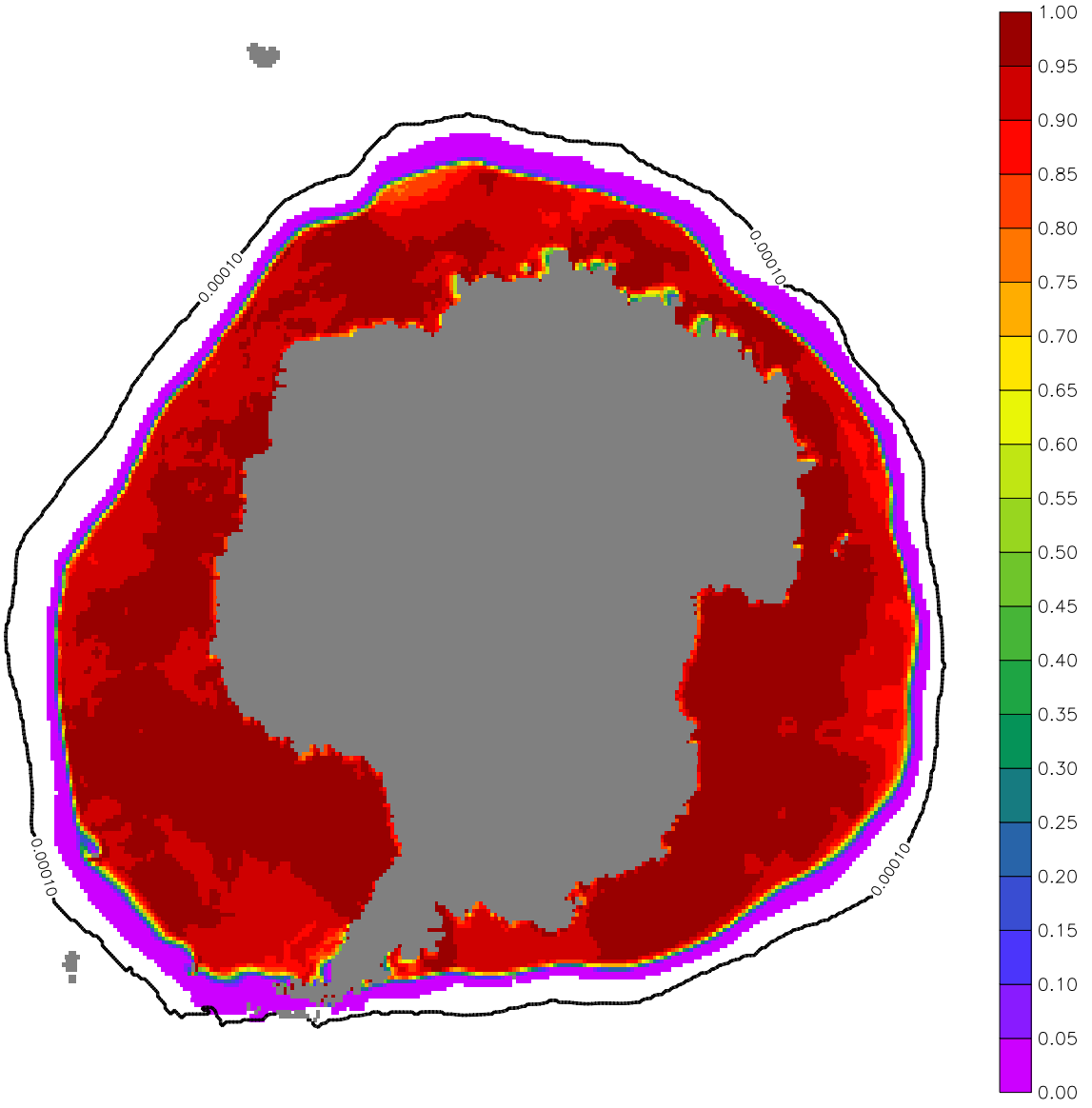

Figure 4.23: Ice concentration for simulation using forcing offsets consistent with IPCC AR4 A1B scenario projections for 2100 near ice maximum (27 September). Also shown is the 0.01% ice concentration contour from the optimized simulation (black). Land mask is grey. The offsets were applied to the 1998 forcing.

5. Discussion

5.1 Indroduction

This chapter discusses the results in the same order as presented in Chapter "4". There is an additional short discussion of the model sensitivity results which were not presented in Chapter "4" but are found in Chapter "2" and in Appendix "A".

5.2 Ice growth and decay

As stated in chapter 2 CICE4 calculates the rate of change in the ice thickness distribution with a discrete version of equation 2.1. The first term on the right hand side is the contribution made by ice movement, the second is thermodynamic processes, and the last is dynamic processes. Total ice volume can only be changed by the thermodynamic processes of freezing and melting and by the conversion of snow to ice. Because CICE4 is calculating change in ice thickness the dynamic processes ridging and rafting can be considered mechanisms of ice growth within a grid cell through the addition of ice thickness. Ridging is caused by a negative gradient in ice velocity across the grid cell in regions of high ice concentration, i.e. ice entering the grid cell faster than ice leaving. Even in regions of low ice concentration a gradient in ice velocity will cause changes of average ice thickness within the grid cell. This can be understood by considering the open water fraction of the grid cell to be ice of zero thickness. If a velocity gradient exists, e.g. a positive gradient where ice leaves the grid cell faster than ice enters it, then the grid cell will contain more zero thickness ice at the end of each time step, thereby decreasing average ice thickness. Conversely a negative velocity gradient will reduce the area occupied by open water (zero ice thickness) and so increase the average ice thickness in the grid cell.

5.2.1 Ice growth

Congelation ice is the dominant ice production mechanism in CICE4. It accounts for 67% of total ice growth in our simulations. Frazil ice accounts for only 7% in our simulations, which is much less than the ∼50% measured in some Southern Ocean studies (Gow et al., 1987; Jacka et al., 1987; Lange et al., 1989; Allison and Worby, 1994). In some locations such as along the prime meridian, almost all the ice comprised consolidated pancakes that originated as frazil ice (Wadhams et al., 1987). Our simulations overestimate congelation ice and underestimate frazil ice because CICE4 classifies as congelation ice any ice that is produced where ice exists. In reality congelation ice only forms under low wind conditions (<3 m s^{-1}) (Eicken and Large, 1989). Granular ice formed from frazil predominates when winds

are stronger than 10 m s^{-1} keeping the ocean surface agitated and maintaining open water. A better frazil ice parameterization is clearly needed for CICE4. Possibly the model would be improved by the inclusion of a representation of grease ice (Bauer and Martin, 1983) or at least the inclusion of collection thickness (Biggs et al., 2000). LIM3 has a collection thickness and performs much better in this regard with congelation ice accounting for 37%, frazil 38% and snow-ice 25% of total volume of ice created (i.e. excluding dynamic ice growth) (Vancoppenolle et al., 2009).

Dynamically grown ice accounts for about 24% of total ice volume in our simulations based on increasing ice thickness. In the Bellingshausen and Amundsen seas ice less than 0.3 m is usually rafted before attaining this thickness (Worby et al., 1996). The degree of rafting of thin ice varies with wind strength such that <10% of the ice area is deformed when winds are <3 m s^{-1} increasing to >50% when winds are >10 m s^{-1} (Eicken and Large, 1989). So the simulated estimate of 24% is almost certainly too low under Southern Ocean conditions. This underestimate can probably be attributed to the parameterization of dynamic ice growth in CICE4 which emphasises ridging rather than rafting. Even in the Arctic Ocean where first year ice is less common, modelling rafting improves the simulated ice thickness distribution (Babko et al., 2002). Experiments using LIM3 have shown a 25% increase in Southern Ocean simulated sea ice volume and larger ice extent in summer (1×10^6 km^2) when rafting is included (Vancoppenolle et al., 2009). While this increase in summer ice extent would not completely overcome the ice area deficit in our simulations it would improve the situation enormously.

In the Southern Ocean snow loadings are often high so snow-ice can contribute considerably to total ice volume. In regions like the Bellingshausen and Amundsen seas snow-ice can be as much as 24% of ice cores (Jeffries et al., 1997). In East Antarctic waters 13% has been measured (Worby and Wu, 1998). While the volume of snow-ice produced annually in our simulations is low in January it accounts for almost 30% of ice production. There are two reasons for this. Firstly there is very little thermodynamic production (congelation and frazil). Secondly as ice melts at the bottom the ice-snow interface is more likely to be depressed below the sea surface (Lytle and Ackley, 2001). This association between basal melt and snow-ice growth is well represented in the simulations presented in this thesis (Fig. 4.10). Spring and summer are the seasons when snow-ice production is high and this agrees with Southern Ocean simulations with LIM3 (Vancoppenolle et al., 2009). However, over the model domain CICE4 probably underestimates snow-ice growth in the Southern Hemisphere. The reasons for the under production of snow-ice are not clear. It is possible that the CICE4 ice density is too low and so more snow is required to depress the interface between ice and snow to the ocean surface. Alternatively, if the snow that falls has a density that is too low then it may not be sufficient to depress the ice to snow interface to the ocean surface. It is also possible that PolarLAPS is underestimating snow fall.

5.2.2 Ice decay

In the Southern Ocean oceanic heat fluxes can be substantial (Lytle and Ackley, 1996; McPhee et al., 1999; Lytle et al., 2000). Oceanic heat can cause basal melt of the sea ice depending on the rate at which heat is conducted from the bottom surface of the ice. During winter in the Weddell Sea, for instance, the sea ice can experience alternating time intervals of growth and decay depending largely on air temperatures (Lytle et al., 2000). It is to be expected that basal melt is the dominant decay mechanism and this is reflected in our simulations.

The mechanism producing the oceanic heat flux is deep convection caused by brine rejection from sea ice growth. Therefore oceanic heat will be at a maximum when sea ice growth is a maximum. Our simulation attempted to model this by using a time varying oceanic heat flux that was a maximum early in the ice growth season.

Top melt contributes much less to total ice decay in the Southern Ocean than in the Arctic Ocean. This is because the air in the Southern Hemisphere is considerably less humid than in the Northern Hemisphere (Andreas and Ackley, 1982). Snow and ice at the top surface tend to sublime rather than form melt-ponds as happens in the Arctic Ocean.

Lateral melt comprises a very small fraction of total ice decay in our simulations. Lateral melt rates depend on the size of the ice floe. In small floes the lateral melt rates will be large compared to those of large floes (Steele, 1992). So in regions like the MIZ where small floes are common lateral melt rates will be higher. These floes will soon disappear unless they are replaced by the breaking-up of large floes. Wave energy decays exponentially with distance from the ice edge (Wadhams et al., 1988). Wave energy is therefore high in the MIZ tending to promote floe break-up thus maintaining the floe size distribution. CICE4 does not have a floe size distribution and instead prescribes a constant floe diameter. It is not surprising therefore that simulated lateral melt rates are low even in the MIZ.

Our simulated ice decay is in reasonable agreement with results from other models. Simulations with LIM3 for instance found that basal melt accounted for 95% of total ice decay (Vancoppenolle et al., 2009) compared to 88% in our simulation. LIM3 does not simulate lateral melt so the remaining 5% is top melt compared to 11% in our simulation.

5.2.3 Model sensitivity

The model sensitivity component of this thesis was undertaken to determine the response of the model throughout the seasonal cycle. What was important was the sign of the response and its magnitude and how these vary in time. Almost all the sensitivity results presented in Chapter 2 and Appendix A are in line with expectations based on first principles. For instance, total ice area is reduced throughout the year when air temperature is increased. The response to increased mixed layer depth is more complex but makes sense when considering that a deeper mixed layer means there is a larger volume of water to heat or cool. Similarly for a increase in cloud fraction which causes a increase in total ice area in summer, when downward short-wave radiation is most intense, but a slight reduction in ice area in winter when the increase in cloud fraction increases the downward long-wave radiation.

Probably the most difficult to understand is the model's response to increase in ice density. The fact that the volume response is much larger than the area response seems reasonable. However, it seems strange that an increase in ice density causes an increase in total ice area and total ice volume. It would appear more logical that the freezing of a given volume of sea water into low density ice would produce a greater volume of ice compared to the high ice density case. The volume of sea water that freezes is determined by the net energy flux out of the mixed layer and should be independent of ice density.

What is certain is that the ice density value is important in determining the volume of ice produced by the model. CICE4 uses a constant value for ice density and no attempt is made to model the different densities of the various ice types produced. This is probably less of an issue for the northern hemisphere where snow ice and granular ice produced from the frazil, grease, pancake mechanism are less prevalent. In the Southern Ocean larger errors in ice

volume can be expected in space and time because of differences in the types of ice produced.

5.3 Variability of total ice area and total ice volume

The model results showing a positive correlation between ice area and ice volume (Fig. 4.16) are at odds with recent satellite-based measurements of ice thickness which indicate that Southern Ocean sea ice is getting thinner while its area is increasing leading to little change in total ice volume (Kurtz and Markus, 2012).

In the simulation time interval 1998–2008 the trend for total ice area was positive but not significant with about an 80% chance of this trend being due to normal interannual variation. The 1998–2008 trend in total ice volume is also slightly positive but not significant ($p = 0.77$).

Kurtz and Markus (2012) estimated ice thickness and ice area for the years 2003 to 2008 which form a segment of our simulation. For this time interval the trend in simulated annual average ice thickness is also negative, decreasing by 1 cm year^{-1} ($p = 0.11$, $r = -0.72$) and the simulated total ice area in increasing slightly (0.13% year^{-1}, $p = 0.87$, $r = 0.09$). However, the trend in annually averaged ice thickness for the full eleven year simulation is slightly positive but not significant, 0.33 cm year^{-1} ($p = 0.41$, $r = 0.28$). It would appear possible that Kurtz and Markus (2012) results are a product of the short time series available to them and an almost doubling of the time series to eleven years is sufficient to remove the observed trends. For the simulations probably the greatest errors are associated with the prescribed constant densities for snow and ice. Southern Ocean snow is known to vary by more than 10% (Toyota et al., 2011a; Eicken and Large, 1989). Southern Ocean sea ice also varies in density between seasons with summer ice values of 875 kg m^{-3} and winter of 920 kg m^{-3} (Buynitskiy, 1967).

Kurtz and Markus (2012) conclude that the errors in estimating freeboard are negligible based on a method by Markus *et al.* (2011). Nevertheless, there remain errors in estimating snow loading and in snow and ice densities. In numerical simulations like ours density is also the major source of errors. CICE4 has a constant ice density. All ice, once it has formed has this density. Furthermore, CICE4 does not include a sea water fraction in dynamically grown ice. In reality the density of ice will vary in space and time. The different ice types have different densities and their proportions in any sea ice section will determine the bulk density. The proportions of different ice types and the fraction of sea water within the sea ice section will vary in time as ice forms and melts and as dynamically grown ice compacts and consolidates.

In the sensitivity analysis changes in ice density had small effects on ice area but much larger ones on ice volume, i.e. about ten times larger. Therefore errors in ice density will manifest mostly as errors in ice thickness and volume rather than area.

5.4 Determination of the ice-edge location

The relative contributions of ice advection and thermodynamic ice growth vary with longitudinal zone (Fig. 4.18). In April thermodynamic growth is dominant in practically all zones. This has been quantified by summing all zones where northward ice velocity is greater than the northward expansion rate of the ice edge (Fig. 4.19). In May there is one zone in the western Weddell Sea where northward ice velocity is greater than the northward expansion rate of the ice edge. By July there are many zones where the northward ice velocity is greater

than the northward expansion rate of the ice edge, i.e. in East Antarctica (57–87 °E, 91–99 °E, and 143–150 °E), in the Ross Sea (173–177 °E and 186–195 °E), in the Bellingshausen Sea (275–277 °E), and in the Weddell Sea (305–331 °E) (Fig. 4.18). These zones account for about 30% of the longitudinal extent included in the calculation. From April to December the zonal distribution of northward ice velocity has a fairly consistent pattern of peaks, with the maximum centred on 74 °E, and secondary peaks in the Weddell Sea and Ross Sea. This is because the ice velocity is largely determined by the pattern of the prevailing winds and currents. It is the northward expansion rate of the ice edge which is changing, i.e. decreasing from April to December as the contour of the freezing conditions slows its movement north, stops and then contracts towards the coast. As the freezing conditions contour moves south an increasing number of zones have an ice velocity greater than the edge speed.

Errors common to the estimation of northward ice speed and the northward expansion rate of the ice edge are associated with the resolution of the model grid (about 27 km) and the re-gridding to a rectilinear grid with a 0.2 degree latitude resolution to facilitate 1 degree longitude sampling. Errors in estimating the northward ice speed at the ice edge also include defining a range of ice concentrations which are close to the ice edge but will not produce gaps in the data. The extreme ice edge (ice concentrations greater than zero but less than 2%) has a lower northward ice speed than at ice concentrations of 30%. The reason for this is not clear because the ice-atmosphere momentum interaction calculations do not include an ice concentration term. However, the ice-ocean interaction calculations do and this may be the cause. The extreme ice edge was therefore excluded from the estimation of the northward ice speed even though this reduced the sampling area. Error peculiar to the estimation of the northward expansion rate of the ice edge relate to the selection of a sampling time interval. This needed to be a large enough interval to produce a measurable displacement of the ice edge and but as small as possible to give the best temporal resolution.

In theory it should be possible to compare the modelled ice velocities with satellite-based estimates, i.e. from passive microwave or SAR. These estimates are based on tracking features between two acquisitions displace in time by up to three days. Dividing the displacement thus obtained by the time between acquisitions estimates the average ice velocity for this time interval. However, in practice the feature tracking systems fail in all but high ice concentrations.

5.5 Model predictions for changed climate

Applying forcing offsets that are consistent with the IPCC AR4 A1B scenario projections for 2100 has a greater effect in summer than winter for both total ice area and volume (Fig. 4.21). Near ice minimum ice concentrations greater than 15% are largely restricted to the Weddell Seas and to the up-stream sides of East Antarctic coastal protrusions. These latter locations are sites of very thick ice produced by the intense dynamic ice growth as the westward ice drift is interrupted by the fast-ice. The thickest ice is produced by this mechanism upstream of the Ninnis Bank fast-ice near 150 °E and is sufficiently thick to survive melting even in very warm climates. There are two reasons for the large thickness of ice produced at this location. Firstly the Ninnis Bank fast-ice projects well to the north into westward drifting pack ice. Secondly the pack ice stream that reaches 150 °E has a large source region which includes a large part of the Ross Sea and so is concentrated and thick.

It has to be remembered that in these simulations the Ninnis Bank fast-ice, and indeed all

similar East Antarctic coastal protrusions, are part of the land mask and therefore not subject to decay processes as real fast-ice. Whether these fast-ice fields would exist in a warmer climate is not certain. The fast ice can form because it is anchored by a multitude of small and sometimes large icebergs that have become grounded on the relatively shallow water over the Ninnis Bank (Massom, 2003). The A1B compatible simulation produces about 80% of current total ice area in winter (Fig. 4.21) so there would still be the opportunity for the Ninnis Bank fast-ice to form at this time of year. It is more difficult to estimate the fate of fast-ice in summer when melting is highest and breakout of fast-ice is more likely (Fraser et al., 2012). There is also evidence that dynamically grown fast-ice such as east of the Ninnis Bank is less resistant to breakouts than if it had grown thermodynamically (Fraser et al., 2012).

The aim of the "all-but-one" set of simulations was to quantify the relative importance of the various A1B forcing offsets. Both total ice area and total ice volume were examined. The sign of the restored total ice area is in agreement with the sensitivity results. For instance, the sensitivity results showed that increasing air temperature decreases total ice area and when the higher temperatures were removed in the "all-but-one" simulations there was a large increase in total ice area. Increased wind strength in the sensitivity studies produced larger total ice area. In the "all-but-one" simulations wind strength was reduce and total ice area decreased. More interesting is the ranking of the contribution. Air temperature (A1B offset of 1.2 °C in summer and 3.0 °C in winter) proved to have the largest impact which was more than three times larger than the next highest ranking forcing. The next highest was humidity which is a little unexpected (A1B offset of +20%). But the humidity increase is on top of a low base compared to cloud fraction, which is generally high in the Southern Ocean sea ice zone. The third ranked forcing was downward long-wave radiation (A1B offset of +12 W m^{-2}). Wind speed had a similar response in magnitude to downward long-wave radiation but in the opposite direction (A1B offset +25%). The A1B offsets for cloud fraction, precipitation, and surface air pressure produced small changes in total ice area and total ice volume.

6. Conclusions

In this study the various ice growth and decay processes were examined and their relative contributions to changes in ice thickness were quantified. The fractional contributions to thermodynamic growth different from in-situ observations but there is reason to believe that the total thermodynamic growth is well represented. Thickening by dynamic ice growth is underestimated in our simulations largely because rafting of thin ice is not included in CICE4's parameterization. Snow-ice growth is also examined and found to have a reasonable spatial distribution but to account for less ice thickness than is often measured in the field. The reasons for this are not clear but uncertainty in snow and ice density are likely to be the reasons and it is also possible that the snow fall is underestimated in PolarLAPS.

Some of the relationships between factors influencing thermodynamic ice growth were presented. Ice thickness was shown to be very important. Air temperature was found to correlate best with top surface temperature. Downward long-wave radiation had the second best correlation with surface temperature. However, there is a relationship between downward long-wave radiation and air temperature so they are not independent.

The sensitivity of CICE4 to a number of forcing fields was assessed in relation to the fractional change caused in total ice area for small perturbations in forcing. Sensitivity studies were carried out for the forcing fields used for tuning the model on an hourly basis (mixed layer depth, surface air temperature, and cloud fraction). Other forcing examined includes ice density, precipitation, surface humidity, wind strength, downward short- and long-wave radiation, ice and snow albedo, thermal conductivity of snow, ocean albedo, surface currents, ocean drag coefficient, deep ocean heat, and sea surface salinity.

In investigating research question 1, the relationship between annual average total ice area and annual average total ice volume was examined for the eleven years of our simulation (1998 to 2008). During this time interval there were slight positive trends in area, volume and thickness but none were significant at 90% confidence. The 2003–2008 sub-interval had slight positive area trend but negative thickness and volume trends. None of these were significant at 90% confidence. It was found that the annual average total ice volume correlates with the annual average total ice area. Examining this relationship by month shows a highly significant correlation (99%) from January to April. But the correlation deteriorates as the year progresses but May and June still signifigant at 95%. July to October fail at 90% after which the correlation improves and is once again significant at 95% in November and December.

In investigating research question 2, the model was used to examine ice growth and decay processes and to quantify the likely contribution that ice advection makes to the determination of the latitude of the ice edge from April to December. Early in the ice growth season the northward movement of the ice edge was determined predominantly by thermodynamic growth processes. As the ice growth season progressed, ice advection was of increasing importance and this could be measured by comparing speed of ice advection to the north and northward

speed of the ice edge. The zonal average ice advection speed approached and then passed that of zonal average ice edge speed. The increasing importance of ice advection was also measured by summing the longitudes where northward ice advection speed was greater than the ice edge speed. This measure increased from less than 10% in April to over 90% in December. This increase was due to a decrease in the speed of the ice edge as the year progressed while the northward ice velocity changed very little with season.

In investigating research question 3, simulations were completed using forcing offset by amounts that are compatible with the IPCC Fourth Assessment Report for 2100 projections of climate using the A1B scenario. These showed that the summer total ice area was greatly reduced to about 2% of present values while winter total ice area suffered a much smaller reduction to about 80% of present values. Ice minimum occurs earlier in February and at this time ice of higher than 15% concentration is only found deep in the Weddell Sea and on the upstream sides of the East Antarctic coastal protrusions. The Ninnis Bank fast-ice is one of these protrusions and this is the site of the thickness and most enduring ice to remain in warm climates. What is uncertain is whether the Ninnis Bank fast-ice itself would survive in the warmer climates.

7. Further Work

In the Southern Ocean frazil ice is the dominant form of thermodynamic ice growth. Yet, as this thesis shows, CICE4 produces relatively small amounts. Simply including a collection thickness improves the fraction of frazil ice produce and this would be a useful addition to CICE. Introducing a ice type dependence on wind speed might improve the relative fraction of different ice types. More could possibly be done in the sub-grid representation of leads but this would be a greater change than adding a collection thickness.

It might be useful to develop the Virtual Ice Buoy application and use this to evaluate the importance of refinements like multiple or even variable ice and snow density. It could also be used to evaluate the importance of dynamic ice growth parameterizations. In theory virtual ice cores could be created as a record of the growth and decay processes.

The slab ocean is a very simplified representation of the ocean and its processes. Ice-ocean interaction processes would be improved if the model represented some or all of the following:

- mass and thermal energy transport within surface currents
- calculation of mixed layer depth by each grid cell which would allow it to vary spatially and temporally
- calculation of deep ocean heat based on changes in mixed layer depth
- calculation of salinity in the mixed layer through interaction of sea ice and atmosphere
- bathymetry especially over the continental shelf
- ocean tides
- ocean waves

Adding all this complexity to the representation of the ocean suggests that a better path might be to couple CICE4 to an ocean model. Coupling has its own issues and because most ocean models are on a lower resolution grid than used in this research the gains of coupling may not be as great as hoped. A solution to the resolution issue is an adaptive grid that has higher resolution where needed in the sea ice zone (Debreu et al., 2008). Because sea ice has its greatest interactions and influence on the top 20 or 30 m of ocean beneath the ice it might be possible to have the sea ice model responsible for this layer and for the coupled ocean model to be responsible for the rest of the ocean.

CICE4 uses an elastic-viscous-plastic rheology. One alternative that shows promise in the Arctic Ocean is the elasto-brittle (EB) rheology (Girard et al., 2011). However, sea ice is not a 2-dimensional elastic substance so in this way EB is un-physical. Also, the EB rheology may

not work as well in the Southern Ocean because the ice is more open there compared to the Arctic Ocean. With ice concentrations above 95% the stresses modelled in the EB framework can be transmitted over long distances in a time step sub-cycling process. However, Southern Ocean sea ice can often be below 95% ice concentration and so long distance stress transmission may not be important or possible. However, there are locations, like in the high shear zone near the Antarctic Coast, where the EB rheology may be useful at improving the quality of ice dynamic simulations. But the EB has a long way to go before it can demonstrate a significant improvement over current rheologies in large-scale sea ice models running for long simulations.

Bibliography

N. Adams. A numerical modeling study of the weather in east antarctica and the surrounding southern ocean. *Weather and Forecasting*, 19(2):653–672, 2004.

N. Adams. The development of a numerical weather prediction climatology and it's application to antarctic weather forecasting. In *The 4th Antarctic Meteorological Observation, Modelling, and Forecasting Workshop*, Fort Sumter, Charleston, South Carolina USA, 2009.

N. Adams. Re: Polarlaps cloud fraction [sec=unclassified], 2010.

U. Adolphs and G. Wendler. A pilot study on the interactions between katabatic winds and polynyas at the adélie coast, eastern antarctica. *Antarctic Science*, 7:307–314, 1995.

A. Alam and J. Curry. Evolution of new ice and turbulent fluxes over freezing winter leads. *Journal of Geophysical Research - Oceans*, 103(C8):15783–15802, 1998.

I. Allison. Antarctic sea ice growth and oceanic heat flux. In *Sea Level, Ice, and Climatic Change*, 1979.

I. Allison and A. Worby. Seasonal changes of sea ice characteristics off east antarctica. *Annals of Glaciology*, 20(1):195–201, 1994.

I. Allison, R. Brandt, and S. Warren. East antarctic sea ice: albedo, thickness distribution, and snow cover. *Journal of Geophysical Research*, 98(C7):12417–12429, 1993.

E. Andreas and S. Ackley. On the differences in ablation seasons of arctic and antarctic sea ice. *Journal of Atmospheric Science*, 39:440–447, 1982.

E. Andreas, W. Tucker III, and S. Ackley. Atmospheric boundary-layer modification, drag coefficient, and surface heat flux in the antarctic marginal ice zone. *Journal of Geophysical Research - Oceans*, 89(C1):649–661, 1984.

O. Babko, D. Rothrock, and G. Maykut. Role of rafting in the mechanical redistribution of sea ice thickness. *Journal of Geophysical Research: Oceans*, 107:27–1–27–14, 2002.

J. Bauer and S. Martin. A model of grease ice growth in small leads. *Journal of Geophysical Research - Oceans*, 88(C5):2917–2925, 1983.

L. Bennetts, M. Peter, V. Squire, and M. Meylan. A three-dimensional model of wave attenuation in the marginal ice zone. *Journal of Geophysical Research - Oceans*, 115(C12043), 2010.

D. Bi and S. Marsland. Australian climate ocean model (auscom) users guide. Technical report, The Centre for Australian Weather and Climate Research, 2010.

N. Biggs, M. Morales Maqueda, and A. Willmott. Polynya flux model solutions incorporating a parameterization for the collection thickness of consolidated new ice. *Journal of Fluid Mechanics*, 408:179–204, 2000.

E. Bjørgo, O. Johannessen, and M. Miles. Analysis of merged smmr-ssmi time series of arctic and antarctic sea ice parameters 1978-1995. *Geophysical Research Letters*, 24(4):413–416, 1997.

C. Böning, A. Dispert, M. Visbeck, S. Rintoul, and F. Schwarzkopf. The response of the antarctic circumpolar current to recent climate change. *Nature Geoscience*, 1:864–869, 2008.

H. Bornemann, M. Kreyscher, S. Ramdohr, T. Martin, A. Carlini, L. Sellmann, and J. Plotz. Southern elephant seal movements and antarctic sea ice. *Antarctic Science*, 12:3–15, 2000.

R. Brandt, S. Warren, A. Worby, and T. Grenfell. Surface albedo of the antarctic sea ice zone. *Journal of Climate*, 18:3606–3622, 2005.

D. Bromwich, J. Nicolas, K. Hines, J. Kay, E. Key, M. Lazzara, D. Lubin, G. McFarquhar, I. Gorodetskaya, D. Grosvenor, T. Lachlan-Cope, and N. van Lipzig. Tropospheric clouds in antarctica. *Reviews of Geophysics*, 2012.

V. Buynitskiy. Structure, principal properties and strength of antarctic sea ice. *Soviet Antarctic Expedition Information Bulliton (English Translation)*, 65:504–510, 1967.

A. Carleton and M. Fitch. Synoptic aspects of antarctic mesocyclones. *Journal of Geophysical Research - Atmospheres*, 98(D7):12997–13018, 1993.

D. Cavalieri and C. Parkinson. Antarctic sea ice variability and trends, 1979-2006. *Journal of Geophysical Research*, 113(C07004), 2008.

D. Cavalieri, C. Parkinson, and K. Vinnikov. 30-year satellite record reveals contrasting arctic and antarctic decadal sea ice variability. *Geophysical Research Letters*, 30(18), 2003.

J. Charrassin, M. Hindell, S. Rintoul, F. Roquet, S. Sokolov, M. Biuw, D. Costa, L. Boehme, P. Lovell, R. Coleman, R. Timmermann, A. Meijers, M. Meredith, Y. Park, F. Bailleul, M. Goebel, Y. Tremblay, C. Bost, C. McMahon, I. Field, M. Fedak, and C. Guinet. Southern ocean frontal structure and sea-ice formation rates revealed by elephant seals. *PNAS*, 105 (33):11634–11639, 2008.

J. Comiso and A. Gordon. Recurring polynyas over the cosmonaut sea and the maud rise. *Journal of Geophysical Research*, 92(C3), 1987.

J. Comiso and F. Nishio. Trends in the sea ice cover using enhanced and compatible amsr-e, ssm/i, and smmr data. *Journal of Geophysical Research*, 113(C02S07), 2008.

J. Comiso and C. Parkinson. Arctic sea ice parameters from amsr-e data using two techniques and comparisons with sea ice from ssm/i. *Journal of Geophysical Research*, 113(C02S05), 2008.

J. Comiso and K. Steffen. Studies of antarctic sea ice concentrations from satellite data and their applications. *Journal of Geophysical Research*, 106(C12):31361–31385, 2001.

J. Comiso and H. Zwally. Concentration gradients and growth/decay characteristics of the seasonal sea ice cover. *Journal of Geophysical Research - Oceans*, 89(C5):8081–8103, 1984.

J. Comiso, R. Kwok, S. Martin, and A. Gordon. Variability and trends in sea ice extent and ice production in the ross sea. *Journal of Geophysical Research - Oceans*, 116(C04021), 2011.

S. Corti, F. Molteni, and T. Palmer. Signature of recent climate change in frequencies of natural atmospheric circulation regimes. *Nature*, 398(6730):799–802, 1999.

R. Courant, K. Friedrichs, and H. Lewy. Über die partiellen differenzengleichungen der mathematischen physik. *Mathematische Annalen*, 100:32–74, 1928.

M. Curran, T. van Ommen, V. Morgan, K. Phillips, and A. Palmer. Ice core evidence for antarctic sea ice decline since the 1950s. *Science*, 302(5648):1203–1206, 2003.

J. Cuzzone and S. Vavrus. The relationships between arctic sea ice and cloud-related variables in the era-interim reanalysis and ccsm3. *Environmental Research Letters*, 6, 2011.

C. de Boyer Montégut, G. Madec, A. Fischer, and A. Lazar. Mixed layer depth over the global ocean: An examination of profile data and a profile-based climatology. *Journal of Geophysical Research*, 109(C12003), 2004.

W. de la Mare. Abrupt mid-twentieth-century decline in antarctic sea-ice extent from whaling records. *Nature*, 389:57–60, 1997.

S. de la Rosa and S. Maus. Laboratory study of frazil ice accumulation under wave conditions. *The Cryosphere Discussions*, 5:1835–1886, 2011.

S. de la Rosa, S. Maus, and S. Kern. Thermodynamic investigation of an evolving grease to pancake ice field. *Annals of Glaciology*, 52(67), 2011.

L. Debreu, C. Vouland, and E. Blayo. Agrif: Adaptive grid refinement in fortran. *Computers and Geosciences*, 34:8–13, 2008.

H. Douville, F. Chauvin, S. Planton, J. Royer, D. Salas-Mélia, and S. Tyteca. Sensitivity of the hydrological cycle to increasing amounts of greenhouse gases and aerosols. *Climate Dynamics*, 20(1):45–68, 2002.

S. Downes, A. Budnick, J. Sarmiento, and R. Farneti. Impacts of wind stress on the antarctic circumpolar current fronts and associated subduction. *Geophysical Research Letters*, 38 (L11605), 2011.

J. Dukowicz and J. Baumgardner. Incremental remapping as a transport/advection algorithm. *Journal of Computational Physics*, 160:318–335, 2000.

E. Ebert and J. Curry. An intermediate one-dimensional thermodynamic sea ice model for investigating ice-atmosphere interactions. *Journal of Geophysical Research*, 98(C6):10085–10109, 1993.

H. Eicken and M. Large. Development and properties of sea ice in the coastal regime of the southeastern weddell sea. *Journal of Geophysical Research*, 94(C6):8193–8206, 1989.

L. Emmerson and C. Southwell. Sea ice cover and its influence on adélie penguin reproductive performance. *Ecology*, 89:2096–2102, 2008.

S. Farrell, S. Laxon, D. McAdoo, D. Yi, and H. Zwally. Five years of arctic sea ice freeboard measurements from the ice, cloud and land elevation satellite. *Journal of Geophysical Research - Oceans*, 114(C04008), 2009.

S. Farrell, T. Markus, R. Kwok, and L. Connor. Laser altimetry sampling strategies over sea ice. *Annals of Glaciology*, 52(57), 2011.

J. Forcada, P. Trathan, K. Reid, E. Murphy, and J. Croxall. Contrasting population changes in sympatric penguin species in association with climate warming. *Global Change Biology*, 12:411–423, 2006.

A. Fraser, R. Massom, K. Michael, B. Galton-Fenzi, and J. Lieser. East antarctic landfast sea ice distribution and variability, 2000-08. *Journal of Climate*, 25(4):1137–1156, 2012.

J. Fyfe and O. Saenko. Human-induced change in the antarctic circumpolar current. *Journal of Climate*, 18(15):3068–3073, 2005.

K. Giles, S. Laxon, and A. Worby. Antarctic sea ice elevation from satellite radar altimetry. *Geophysical Research Letters*, 35(L03503), 2008.

N. Gillett and D. Thompson. Simulation of recent southern hemisphere climate change. *Science*, 302(5643):273–275, 2003.

L. Girard, S. Bouillon, J. Weiss, D. Amitrano, T. Fichefet, and V. Legat. A new modeling framework for sea-ice mechanics based on elasto-brittle rheology. *Annals of Glaciology*, 52 (57), 2011.

K. Golden. Brine percolation and the transport properties of sea ice. *Annals of Glaciology*, 33, 2001.

K. Golden, H. Eicken, A. Heaton, J. Miner, D. Pringle, and J. Zhu. Thermal evolution of permeability and microstructure in sea ice. *Geophysical Research Letters*, 34(16), 2007.

A. Gordon and B. Huber. Southern ocean winter mixed layer. *Journal of Geophysical Research - Oceans*, 95(C7):11655–11672, 1990.

A. Gow, S. Ackley, K. Buck, and K. Golden. Physical and structural characteristics of weddell sea pack ice. Technical report, Cold Regions Research and Engineering Laboratory, 1987.

R. Graham, A. de Boer, K. Heywood, M. Chapman, and D. Stevens. Southern ocean fronts: Controlled by wind or topography? *Journal of Geophysical Research - Oceans*, 117(C08018), 2012.

A. Gupta, A. Santoso, A. Taschetto, C. Ummenhofer, J. Trevena, and M. England. Projected changes to the southern hemisphere ocean and sea ice in the ipcc ar4 climate models. *Journal of Climate*, 22(11):3047–3078, 2009.

P. Heil, V. Lytle, and I. Allison. Enhanced thermodynamic ice growth by sea-ice deformation. *Annals of Glaciology*, 27(1):433–437, 1998.

W. Hibler III. A dynamic thermodynamic sea ice model. *Journal of Physical Oceanography*, 9:815–846, 1979.

M. Hindell, D. Slip, and H. Burton. The diving behavior of adult male and female southern elephant seals, mirounga-leonina (pinnipedia, phocidae). *Australian Journal of Zoology*, 39: 595–619, 1991.

M. Ho, A. Kiem, and D. Verdon-Kidd. The southern annular mode: a comparison of indices. *Hydrology and Earth System Sciences Discussions*, 2011.

A. Hogg, M. Meredith, J. Blundell, and C. Wilson. Eddy heat flux in the southern ocean: response to variable wind forcing. *Journal of Climate*, 21:608–620, 2007.

M. Holland, C. Bitz, and A. Weaver. The influence of sea ice physics on simulations of climate change. *Journal of Geophysical Research - Oceans*, 106(C9):19639–19655, 2001.

E. Hunke and D. Comeau. Sea ice and iceberg dynamic interaction. *Journal of Geophysical Research*, 116(C05008), 2011.

E. Hunke and J. Dukowicz. An elastic-viscous-plastic model for sea-ice dynamics. *Journal of Physical Oceanography*, 27:1849–1867, 1997.

E. Hunke and W. Lipscomb. Cice: the los alamos sea ice model documentation and software user's manual version 4.0 la-cc-06-012, 2008.

T. Jacka, I. Allison, R. Thwaites, and J. Wilson. Characteristics of the seasonal sea ice of east antarctica and comparisons with satellite observations. *Annals of Glaciology*, 9:85–91, 1987.

S. Jacobs and J. Comiso. Climate variability in the amundsen and bellingshausen seas. *Journal of Climate*, 10(4):697–709, 1997.

M. Jeffries, A. Worby, K. Morris, and W. Weeks. Seasonal variations in the properties and structural composition of sea ice and snow cover in the bellingshausen and amundsen seas, antarctica. *Journal of Glaciology*, 43(143):138–151, 1997.

F. Jin. Eddy-induced instability for low-frequency variability. *Journal of the Atmospheric Sciences*, 67(6):1947–1964, 2009.

J. Jones, R. Fogt, M. Widmann, G. Marshall, P. Jones, and M. Visbeck. Historical sam variability. part i: Century-length seasonal reconstructions*. *Journal of Climate*, 22(20): 5319–5345, 2009.

I. Joughin and R. Alley. Stability of the west antarctic ice sheet in a warming world. *Nature Geoscience*, 4, 2011.

A. Karpechko, N. Gillett, L. Gray, and M. Dall'Amico. Influence of ozone recovery and greenhouse gas increases on southern hemisphere circulation. *Journal of Geophysical Research: Atmospheres*, 115:D22117, 2010.

N. Kimura. Mechanisms controlling the temporal variation of the sea ice edge in the southern ocean. *Journal of Oceanography*, 63:685–694, 2007.

A. Kohout and M. Meylan. An elastic plate model for wave attenuation and ice floe breaking in the marginal ice zone. *Journal of Geophysical Research*, 113(C09016), 2008.

N. Kurtz and T. Markus. Satellite observations of antarctic sea ice thickness and volume. *Journal of Geophysical Research - Oceans*, 117(C08025), 2012.

R. Kwok. Satellite remote sensing of sea-ice thickness and kinematics: a review. *Journal of Glaciology*, 56(200):1129–1140, 2010.

M. Lange, S. Ackley, P. Wadhams, G. Dieckman, and H. Eicken. Development of sea ice in the weddell sea. *Annals of Glaciology*, 12:92–96, 1989.

D. Lannuzel, V. Schoemann, J. de Jong, L. Chou, B. Delille, S. Becquevort, and J. Tison. Iron study during a time series in the western weddell pack ice. *Marine Chemistry*, 108:85–95, 2008.

R. Lei, N. Li, P. Heil, B. Cheng, Z. Zhang, and B. Sun. Arctic sea ice thermal regimes and oceanic heat flux derived from a mass balance buoy. *Journal of Geophysical Research - Oceans*, 2012.

M. Leppäranta. *The drift of sea ice*. Springer, 2005.

W. Lipscomb. Remapping the thickness distribution in sea ice models. *Journal of Geophysical Research*, 106(C7):13989–14000, 2001.

A. Lynch, P. Uotila, and J. Cassano. Changes in synoptic weather patterns in the polar regions in the twentieth and twenty-first centuries part 2: Antarctic. *International Journal of Climatology*, 26:1181–1199, 2006.

V. Lytle and S. Ackley. Heat flux through sea ice in the western weddell sea: convective and conductive transfer processes. *Journal of Geophysical Research*, 101(C4), 1996.

V. Lytle and S. Ackley. Snow-ice growth: a fresh-water flux inhibiting deep convection in the weddell sea, antarctica. *Annals of Glaciology*, 33(1):45–50, 2001.

V. Lytle, R. Massom, N. Bindoff, A. Worby, and I. Allison. Wintertime heat flux to the underside of east antarctic pack ice. *Journal of Geophysical Research*, 105(C12), 2000.

T. Markus, R. Massom, A. Worby, V. Lytle, N. Kurtz, and T. Maksym. Freeboard, snow depth and sea-ice roughness in east antarctica from in situ and multiple satellite data. *Annals of Glaciology*, 52(57):242–248, 2011.

S. Martin, R. Drucker, and R. Kwok. The areas and ice production of the western and central ross sea polynyas, 1992-2002, and their relation to the b-15 and c-19 iceberg events of 2000 and 2002. *Journal of Marine Systems*, 68:201–214, 2007.

J. Maslanik, C. Fowler, J. Stroeve, S. Drobot, H. Zwally, D. Yi, and W. Emery. A younger, thinner arctic ice cover: Increased potential for rapid, extensive sea-ice loss. *Geophysical Research Letters*, 34(L24501), 2007.

R. Massom. Observing the advection of sea ice in the weddell sea using buoy and satellite passive microwave data. *Journal of Geophysical Research*, 97(C10):15559–15572, 1992.

R. Massom. Recent iceberg calving events in the ninnis glacier region, east antarctica. *Antarctic Science*, 15:303–313, 2003.

R. Massom, K. Jacka, M. Pook, C. Fowler, N. Adams, and N. Bindoff. An anomalous late-season change in the regional sea ice regime in the vicinity of the mertz glacier polynya, east antarctica. *Journal of Geophysical Research*, 108(C7), 2003.

R. Massom, S. Stammerjohn, W. Lefebvre, S. Harangozo, N. Adams, T. Scambos, M. Pook, and C. Fowler. West antarctic peninsula sea ice in 2005: Extreme ice compaction and ice edge retreat due to strong anomaly with respect to climate. *Journal of Geophysical Research - Oceans*, 113(C02S20), 2008.

R. Massom, K. Hill, C. Barbraud, N. Adams, A. Ancel, L. Emmerson, and M. Pook. Fast ice distribution in adelie land, east antarctica: interannual variability and implications for emperor penguins aptenodytes forsteri. *Marine Ecology Progress Series*, 374:243–257, 2009.

G. Maykut and D. Perovich. The role of shortwave radiation in the summer decay of a sea ice cover. *Journal of Geophysical Research - Oceans*, 92(C7):7032–7044, 1987.

G. Maykut and N. Untersteiner. Some results from a time-dependent thermodynamic model of sea ice. *Journal of Geophysical Research*, 76(06):1550–1575, 1971.

L. McMurdie, C. Claud, and S. Atakturk. Satellite-derived atmospheric characteristics of spiral and comma-shaped southern hemisphere mesocyclones. *Journal of Geophysical Research - Atmospheres*, 102(D12):13889–13905, 1997.

M. McPhee and D. Martinson. Turbulent mixing under drifting pack ice in the weddell sea. *Science*, 263:216–221, 1994.

M. McPhee, C. Kottmeier, and J. Morison. Ocean heat flux in the central weddell sea during winter. *Journal of Physical Oceanography*, 29, 1999.

N. Nakicenovic and R. Swart. *A Special Report of Working Group III of the Intergovernmental Panel on Climate Change*. Cambridge University Press, Cambridge, 2000.

NSIDC. Larsen b ice shelf collapses in antarctica, 2002.

J. Nybakken, W. Broenkow, and T. Vallier. *Interdisciplinary encyclopedia of marine sciences*. Grolier Academic Reference, New York, 2003.

H. Oerter, J. Kipfstuhl, J. Determann, H. Miller, D. Wagenbach, A. Minikin, and W. Graft. Evidence for basal marine ice in the filchner-ronne ice shelf. *Nature*, 358(6385):399–401, 1992.

A. Orsi, T. Whitworth III, and W. Nowlin. On the meridional extent and fronts of the antarctic circumpolar current. *Deep Sea Research Part A*, 42(5):641–673, 1995.

A. Orsi, G. Johnson, and J. Bullister. Circulation, mixing, and production of antarctic bottom water. *Progress In Oceanography*, 43:55–109, 1999.

L. Padman and C. Kottmeier. High-frequency ice motion and divergence in the weddell sea. *Journal of Geophysical Research*, 105(C2):3379–3400, 2000.

S. Palm, S. Strey, J. Spinhirne, and T. Markus. Influence of arctic sea ice extent on polar cloud fraction and vertical structure and implications for regional climate. *Journal of Geophysical Research - Atmospheres*, 115(D21209), 2010.

C. Parkinson and W. Washington. A large-scale numerical model of sea ice. *Journal of Geophysical Research*, 84(C1):311–337, 1979.

C. Parkinson, D. Cavalieri, P. Gloersen, H. Zwally, and J. Comiso. Arctic sea ice extents, areas, and trends, 1978-1996. *Journal of Geophysical Research*, 104(C9):20837–20856, 1999.

M. Raphael. Impact of observed sea-ice concentration on the southern hemisphere extratropical atmospheric circulation in summer. *Journal of Geophysical Research*, 108(D22), 2003.

E. Rignot and S. Jacobs. Rapid bottom melting widespread near antarctic ice sheet grounding lines. *Science*, 296(5575):2020–2023, 2002.

S. Rintoul. Antarctic circumpolar current. In B. R. Kerman, editor, *Encyclopedia of Ocean Sciences*, pages 178–190. Elsevier Ltd., London, 2009.

S. Rintoul, S. Sokolov, and R. Massom. Rapid development and persistence of a massive antarctic sea ice tongue. *Journal of Geophysical Research*, 113(C07045), 2008.

D. Rothrock and A. Thorndike. Measuring the sea ice floe size distribution. *Journal of Geophysical Research*, 89(C10):6477–6486, 1984.

D. Rothrock, Y. Yu, and G. Maykut. Thinning of the arctic sea-ice cover. *Geophysical Research Letters*, 26(23):3469–3472, 1999.

J. Sallée, K. Speer, and S. Rintoul. Zonally asymmetric response of the southern ocean mixed-layer depth to the southern annular mode. *Nature Geoscience*, 3(4):273–279, 2010.

J. Screen, C. Deser, and I. Simmonds. Local and remote controls on observed arctic warming. *Geophysical Research Letters*, 39(L10709), 2012.

M. Sigmond and J. Fyfe. Has the ozone hole contributed to increased antarctic sea ice extent?,. *Geophysical Research Letters*, 37(L18502), 2010.

L. Smedsrud. Grease-ice thickness parameterization. *Annals of Glaciology*, 52(57), 2011.

S. Solomon, D. Qin, M. Manning, M. Marquis, K. Averyt, M. Tignor, J. Miller, and Z. Chen. Climate change 2007: The physical science basis. Technical report, LEGOS, 2007.

V. Squire. Geophysical and oceanographic information in the marginal ice zone from ocean wave measurements. *Journal of Geophysical Research - Oceans*, 100(C1):997–998, 1995.

V. Squire. Of ocean waves and sea-ice revisited. *Cold Regions Science and Technology*, 49: 110–133, 2007.

V. Squire, J. Dugan, P. Wadhams, P. Rottier, and A. Liu. Of ocean waves and sea ice. *Annual Review of Fluid Mechanics*, 27:115–168, 1995.

S. Stammerjohn, D. Martinson, R. Smith, X. Yuan, and D. Rind. Trends in antarctic annual sea ice retreat and advance and their relation to el nino-southern oscillation and southern annular mode variability. *Journal of Geophysical Research - Oceans*, 113(C03S90), 2008.

L. Stearns, B. Smith, and G. Hamilton. Increased flow speed on a large east antarctic outlet glacier caused by subglacial floods. *Nature Geoscience*, 1:827–831, 2008.

M. Steele. Sea ice melting and floe geometry in a simple ice-ocean model. *Journal of Geophysical Research - Oceans*, 97(C11):17729–17738, 1992.

W. Steffen, P. Crutzen, and J. McNeill. The anthropocene: Are humans now overwhelming the great forces of nature? *Ambio*, 36:614–621, 2007.

R. Stevens and P. Heil. The interplay of dynamic and thermodynamic processes in driving the ice-edge location in the southern ocean. *Annals of Glaciology*, 52(57), 2010.

J. Stewart. Gondwana. In B. R. Kerman, editor, *Antarctica: an encyclopedia*, volume 1. McFarland, 1990.

N. Streten and D. Pike. Characteristics of the broadscale antarctic sea ice extent and the associated atmospheric circulation 1972-1977. *Meteorology and Atmospheric Physics*, 29(3): 279–299, 1980.

J. Stroeve, M. Holland, w. Meier, T. Scambos, and M. Serreze. Arctic sea ice decline: Faster than forecast. *Geophysical Research Letters*, 34(L09501), 2007.

T. Tamura and K. Ohshima. Mapping of sea ice production in the arctic coastal polynyas. *Journal of Geophysical Research - Oceans*, 116(C07030), 2011.

T. Tamura, K. Ohshima, T. Markus, D. Cavalieri, S. Nihashi, and N. Hirasawa. Estimation of thin ice thickness and detection of fast ice from ssm/i data in the antarctic ocean. *Journal of Atmospheric and Oceanic Technology*, 24, 2007.

T. Tamura, K. Ohshima, and S. Nihashi. Mapping of sea ice production for antarctic coastal polynyas. *Geophysical Research Letters*, 35(L07606), 2008.

D. Thompson and S. Solomon. Interpretation of recent southern hemisphere climate change. *Science*, 296(5569):895–899, 2002.

A. Thorndike, D. Rothrock, G. Maykut, and R. Colony. The thickness distribution of sea ice. *Journal of Geophysical Research*, 80(33):4501–4513, 1975.

T. Toyota, R. Massom, K. Tateyama, T. Tamura, and A. Fraser. Properties of snow overlying the sea ice off east antarctica in late winter, 2007. *Deep Sea Research Part II*, 58(9-10): 1137–1148, 2011a.

T. Toyota, S. Ono, K. Cho, and K. Ohshima. Retrieval of sea-ice thickness distribution in the sea of okhotsk from alos/palsar backscatter data. *Annals of Glaciology*, 52(57), 2011b.

W. Tucker III, S. Ackley, D. Eppler, D. Farmer, N. Davis, P. Wadhams, Y. Yu, M. Wensnahan, and D. Rothrock. Submarine upward looking sonar ice draft profile data and statistics, 1998.

M. Vancoppenolle, T. Fichefet, H. Goosse, S. Bouillon, G. Madec, and M. Maqueda. Simulating the mass balance and salinity of arctic and antarctic sea ice. 1. model description and validation. *Ocean Modelling*, 27(1):33–53, 2009.

T. Várnai and R. Cahalan. Potential for airborne offbeam lidar measurements of snow and sea ice thickness. *Journal of Geophysical Research*, 112(C12S90), 2007.

D. Vaughan, G. Marshall, W. Connolley, C. Parkinson, R. Mulvaney, D. Hodgson, J. King, C. Pudsey, and J. Turner. Recent rapid regional climate warming on the antarctic peninsula. *Climatic Change*, 60(3):243–274, 2003.

G. Vaughan, L. Bennetts, and V. Squire. The decay of flexural-gravity waves in long sea ice transects. *Proceedings of the Royal Society A*, 465:2785–2812, 2009.

P. Wadhams, M. Lange, and S. Ackley. The ice thickness distribution across the atlantic sector of the antarctic ocean in midwinter. *Journal of Geophysical Research - Oceans*, 92(C13): 14535–14552, 1987.

P. Wadhams, V. Squire, D. Goodman, A. Cowan, and S. Moore. The attenuation rates of ocean waves in the marginal ice zone. *Journal of Geophysical Research*, 93(C6):6799–6818, 1988.

A. Weiss, J. King, T. Lachlan-Cope, and R. Ladkin. On the effective aerodynamic and scalar roughness length of weddell sea ice. *Journal of Geophysical Research - Atmospheres*, 116 (D19119), 2011.

G. Williams and N. Bindoff. Wintertime oceanography of the adélie depression. *Deep Sea Research Part II*, 50(8-9):1373–1392, 2003.

G. Williams, M. Hindell, M. Houssais, T. Tamura, and I. Field. Upper ocean stratification and sea ice growth rates during the summer-fall transition, as revealed by elephant seal foraging in the adélie depression, east antarctica. *Ocean Science*, 7:185–202, 2011a.

G. Williams, A. Meijers, A. Poole, P. Mathiot, T. Tamura, and A. Klocker. Late winter oceanography off the sabrina and banzare coast (117-1281e), east antarctica. *Deep Sea Research Part II*, 58:1194–1210, 2011b.

A. Wong and S. Riser. Profiling float observations of the upper ocean under sea ice off the wilkes land coast of antarctica. *Journal of Physical Oceanography*, 41:1102–1115, 2011.

A. Worby and J. Comiso. Studies of the antarctic sea ice edge and ice extent from satellite and ship observations. *Remote Sensing of Environment*, 92:98–111, 2004.

A. Worby and X. Wu. East antarctic sea ice: observations and modelling. *Annals of Glaciology*, 27:427–432, 1998.

A. Worby, M. Jeffries, W. Weeks, K. Morris, and R. Jaña. The thickness distribution of sea ice and snow cover during late winter in the bellingshausen and amundsen seas, antarctica. *Journal of Geophysical Research*, 101(C12):28441–28455, 1996.

A. Worby, C. Geiger, M. Paget, M. Van Woert, S. Ackley, and T. DeLiberty. Thickness distribution of antarctic sea ice. *Journal of Geophysical Research*, 113(C05S92), 2008.

H. Xie, S. Ackley, D. Yi, H. Zwally, P. Wagner, B. Weissling, M. Lewis, and K. Ye. Sea-ice thickness distribution of the bellingshausen sea from surface measurements and icesat altimetry. *Deep Sea Research Part II*, 58, 2010.

J. Younger. Connectivity and interglacial refugia of east antarctic weddell seals. Honours, IASOS, 2010.

J. Zillman. *A study of some aspects of the radiation and heat budgets of the southern hemisphere oceans*. Australian Government Publishing Service, Canberra, 1972.

H. Zwally, J. Comiso, C. Parkinson, W. Campbell, F. Carsey, and P. Gloersen. Antarctic sea ice, 1973-1976: satellite passive-microwave observations. Technical report, NASA, 1983.

H. Zwally, J. Comiso, C. Parkinson, D. Cavalieri, and P. Gloersen. Variability of antarctic sea ice 1979-1998. *Journal of Geophysical Research - Oceans*, 107(C5), 2002.

A. Model Sensitivity

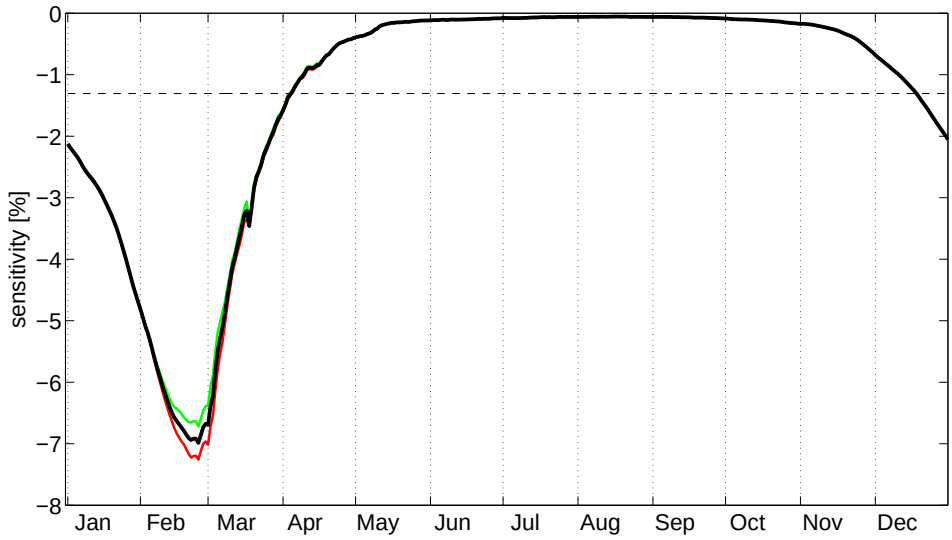

Figure A.1: Change in total ice area for a 1% increase in short-wave radiation in 1998

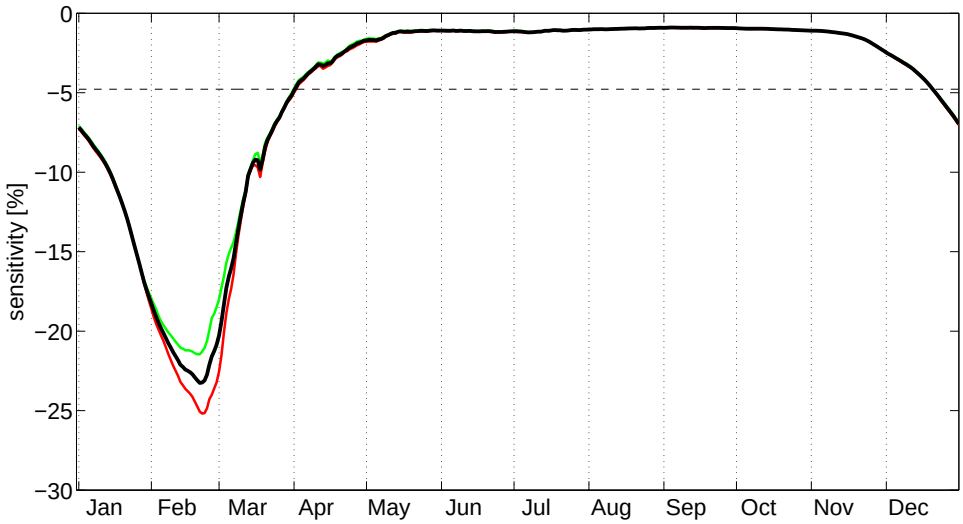

Figure A.2: Change in total ice area for a 1% increase in long-wave radiation in 1998

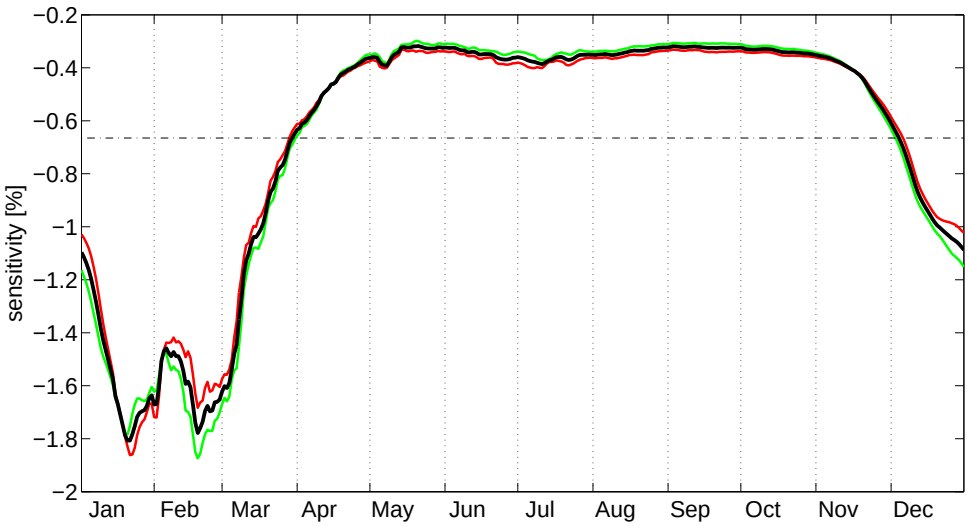

Figure A.3: Change in total ice area for a 1% increase in humidity in 1998

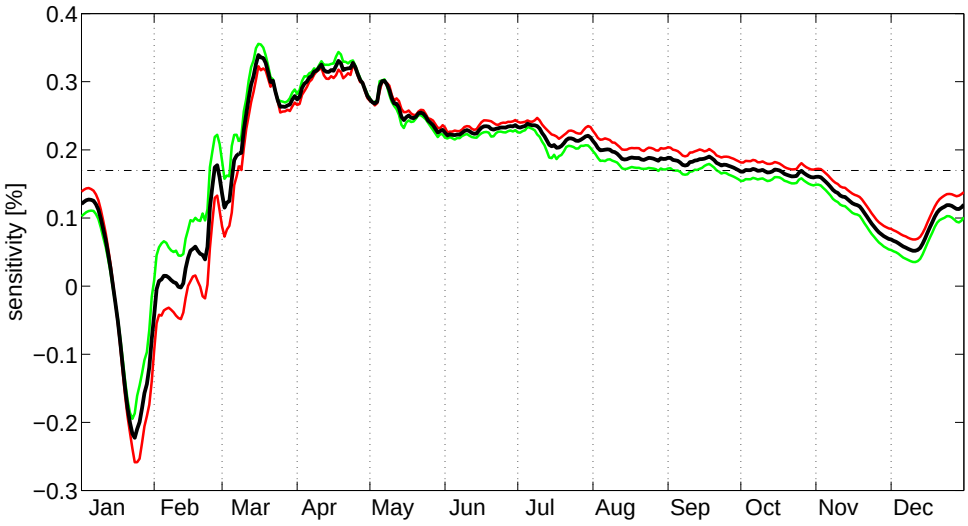

Figure A.4: Change in total ice area for a 1% increase in wind strength in 1998

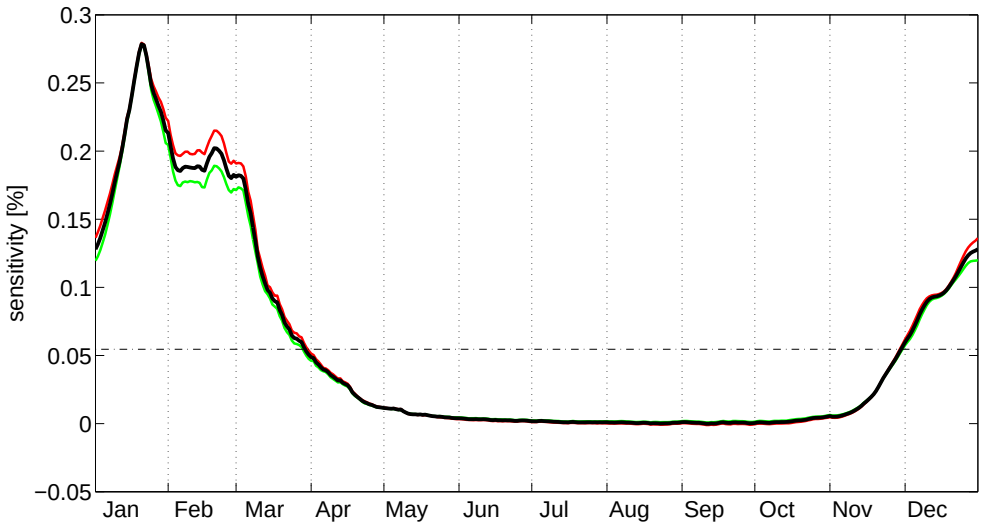

Figure A.5: Change in total ice area for a 1% increase in precipitation in 1998

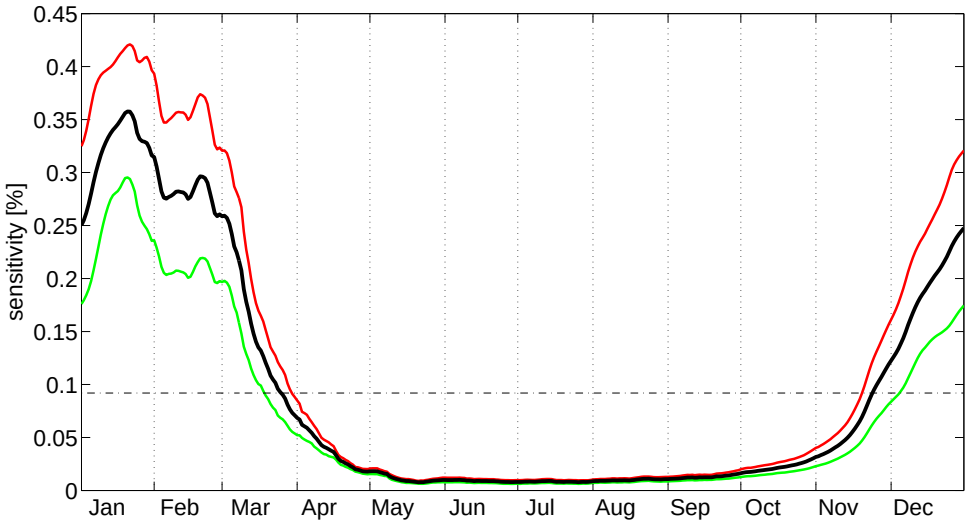

Figure A.6: Change in total ice area for a 1% increase in snow thermal conductivity in 1998

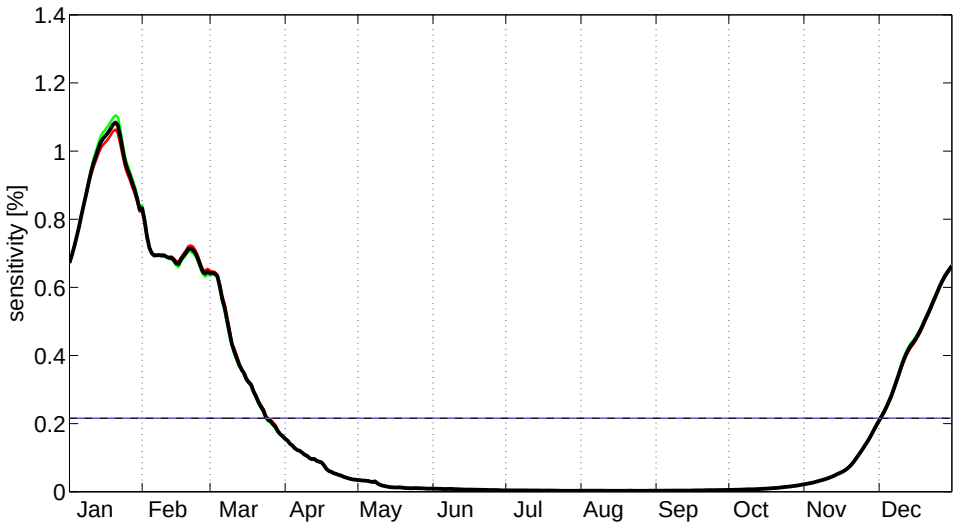

(a)

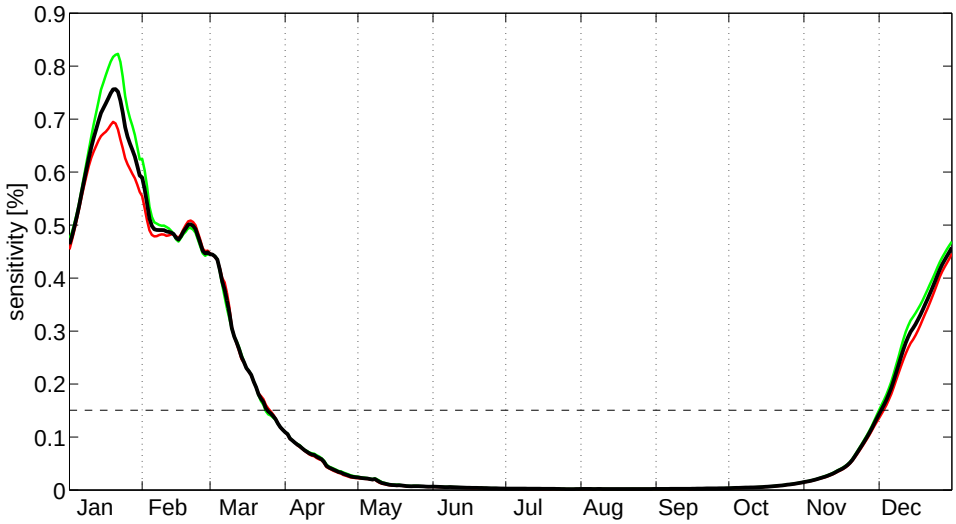

(b)

Figure A.7: Change in total ice area for a 1% increase in the snow albedo (a) visible, (b) infrared

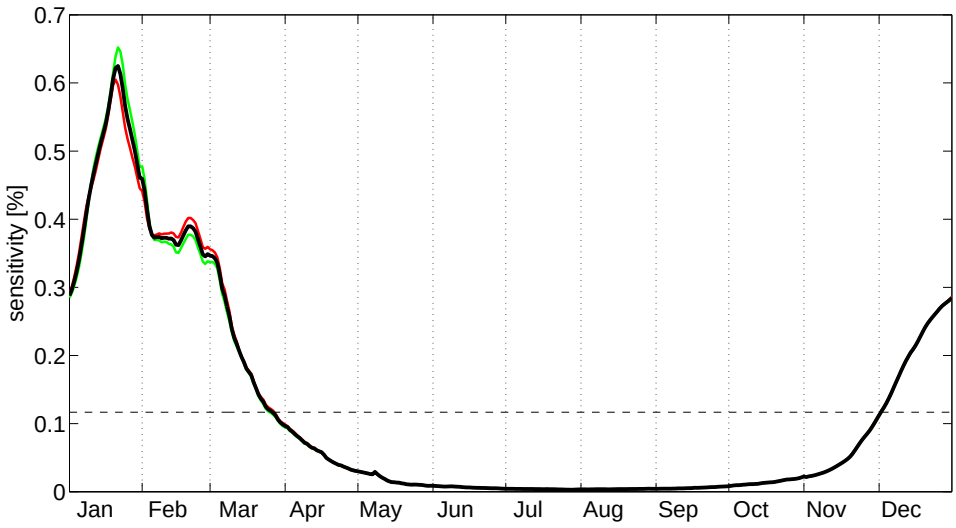

(a)

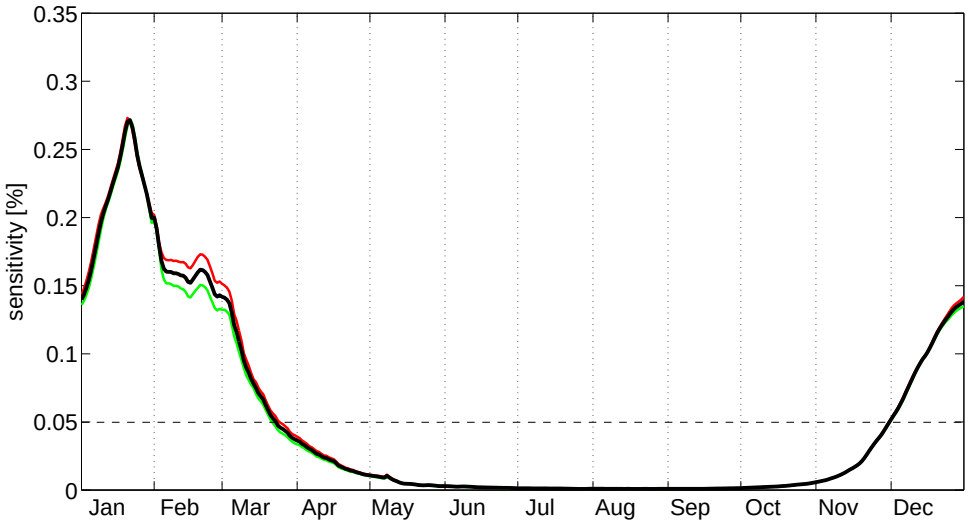

(b)

Figure A.8: Change in total ice area for a 1% increase in the ice albedo (a) visible, (b) infrared

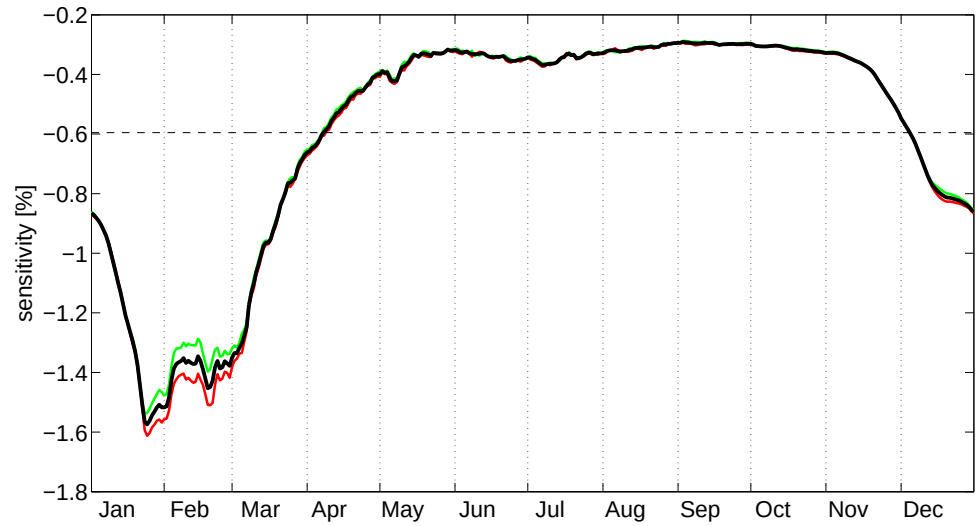

Figure A.9: Change in total ice area for a 1% increase in sea surface salinity in 1998

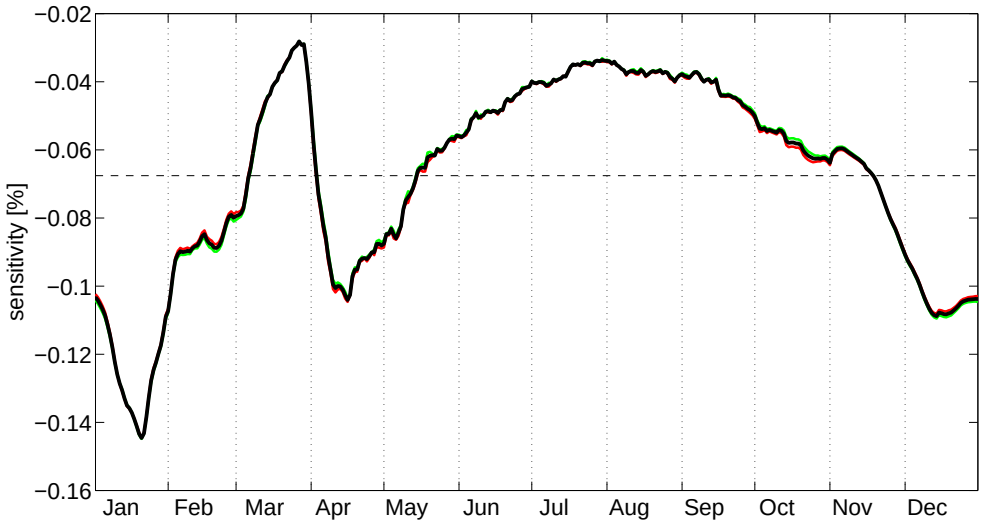

Figure A.10: Change in total ice area for a 1% increase in deep ocean heat in 1998

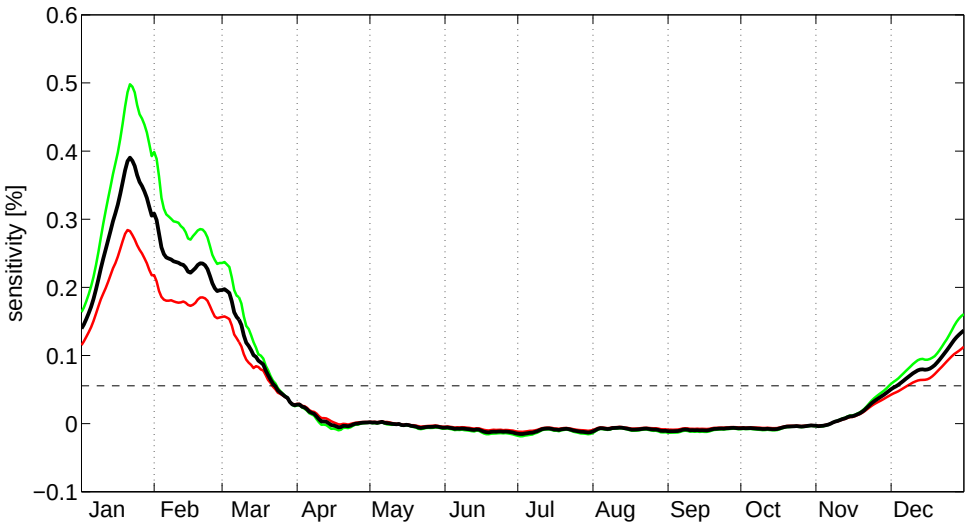

Figure A.11: Change in total ice area for a 1% increase in ice-ocean drag coefficient in 1998

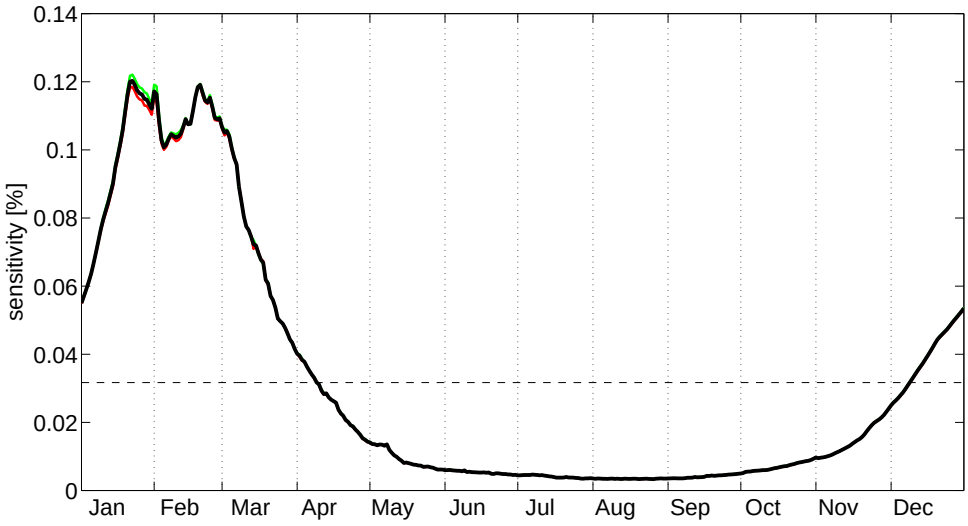

Figure A.12: Change in total ice area for a 1% increase in ocean albedo in 1998

B. Ice_Tracks High Resolution Survey

The VIB tracks are colour and thickness coded by month. The code is:

Jan: black thin
Feb: red thin
Mar: green thin
Apr: dark blue thin
May: light blue thin
Jun: cyan thin
Jul: black thick
Aug: red thick
Sep: green thick
Oct: dark blue thick
Nov: light blue thick
Dec: cyan thick

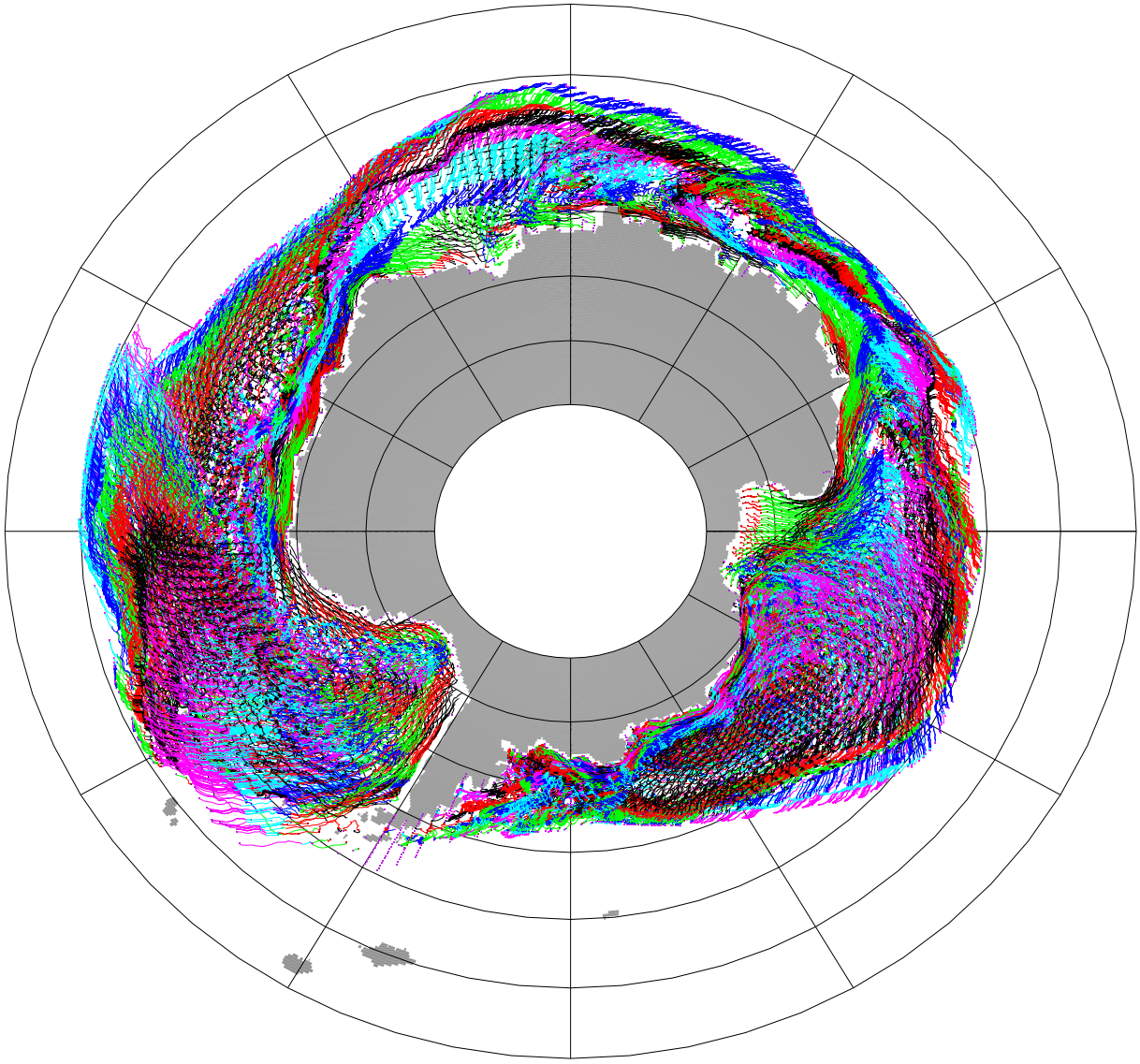

Figure B.1: All VIBs released at 2° longitudinal resolution on 1 January 1998

C. Ice_Tracks Output Fields

Output fields for "ice_tracks":

1. latts - bouy latitude at time step (deg)
2. lonts - bouy longitude at time step (deg)
3. totdist - distance moved in time step (m)
4. ispeed - total speed (m/s)
5. nspeed - speed north (m/s)
6. espeed - speed east (m/s)
7. indxi - grid cell index i where the VIB is located
8. indxj - grid cell index j where the VIB is located
9. aiij - ice conc in grid cell grid cell i,j ()
10. hiij - ice thickness in grid cell i,j (m)
11. snij - snow thickness in grid cell i,j (m)
12. mbij - bottom melt in grid cell i,j (cm/day)
13. mlij - lateral melt in grid cell i,j (cm/day)
14. mtij - top melt in grid cell i,j (cm/day)
15. conij - congel growth in grid cell i,j (cm/day)
16. fraij - frazil growth in grid cell i,j (cm/day)
17. siij - snow-ice growth in grid cell i,j (cm/day)
18. rdgij - ice area ridging frac in grid cell i,j (%day)
19. opnij - lead opening fraction in grid cell i,j (%day)
20. divij - divergance strain rate in grid cell i,j (%day)
21. shrij - shear strain rate in grid cell i,j (%day)

22. fswabij - fsw absorbed in grid cell i,j (W/m^2)
23. sstij - sst in grid cell i,j (C)
24. tairij - air temp in grid cell i,j (C)
25. sairxij - x-axis stress from atmosphere in grid cell i,j (N/m^2)
26. sairyij - y-axis stress from atmosphere in grid cell i,j (N/m^2)
27. scorxij - x-axis stress from coriolisv (N/m^2)
28. scoryij - y-axis stress from coriolis in grid cell i,j (N/m^2)
29. sintxij - x-axis stress from internal forcesv (N/m^2)
30. sintyij - y-axis stress from internal forces in grid cell i,j (N/m^2)
31. socnxij - x-axis stress from ocean in grid cell i,j (N/m^2)
32. socnyij - y-axis stress from ocean in grid cell i,j (N/m^2)
33. stltxij - x-axis stress from sea surface tilt in grid cell i,j (N/m^2)
34. stltyij - y-axis stress from sea surface tilt in grid cell i,j (N/m^2)
35. snetxij - x-axis net stress from all in grid cell i,j (N/m^2)
36. snetyij - y-axis net stress from all in grid cell i,j (N/m^2)
37. uairij - wind in u-direction in grid cell i,j (m/s)
38. vairij - wind in v-direction in grid cell i,j (m/s)
39. uocnij - currents in u-direction in grid cell i,j (m/s)
40. vocnij - currents in v-direction in grid cell i,j (m/s)
41. sfpij - air preasure in grid cell i,j (Pa)

D. Monthly Average Air Temperature

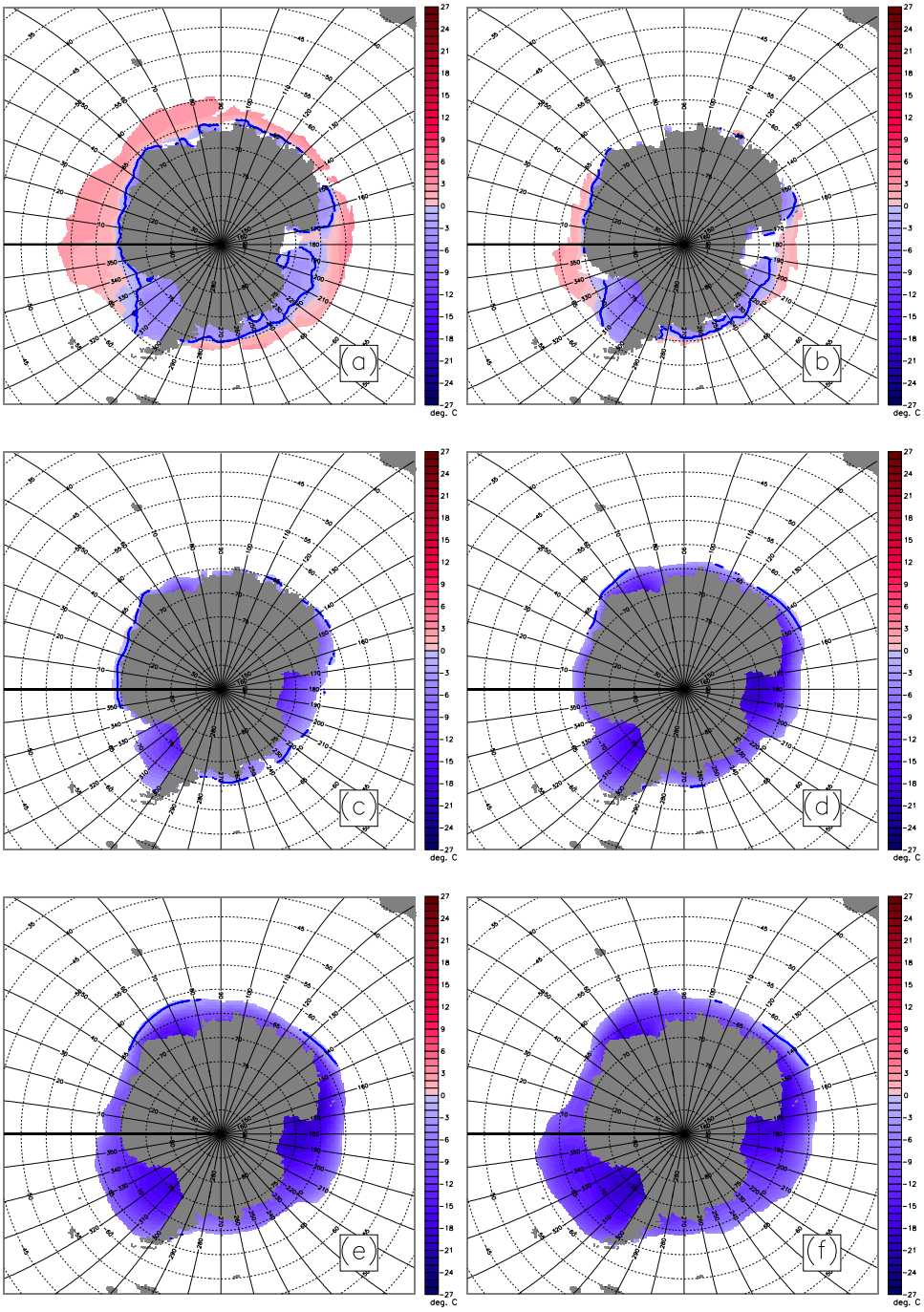

Figure D.1: Seasonal change of the 1998 to 2008 average air temperature in the sea ice zone: (a) January; (b) February; (c) March; (d) April; (e) May; (f) June.

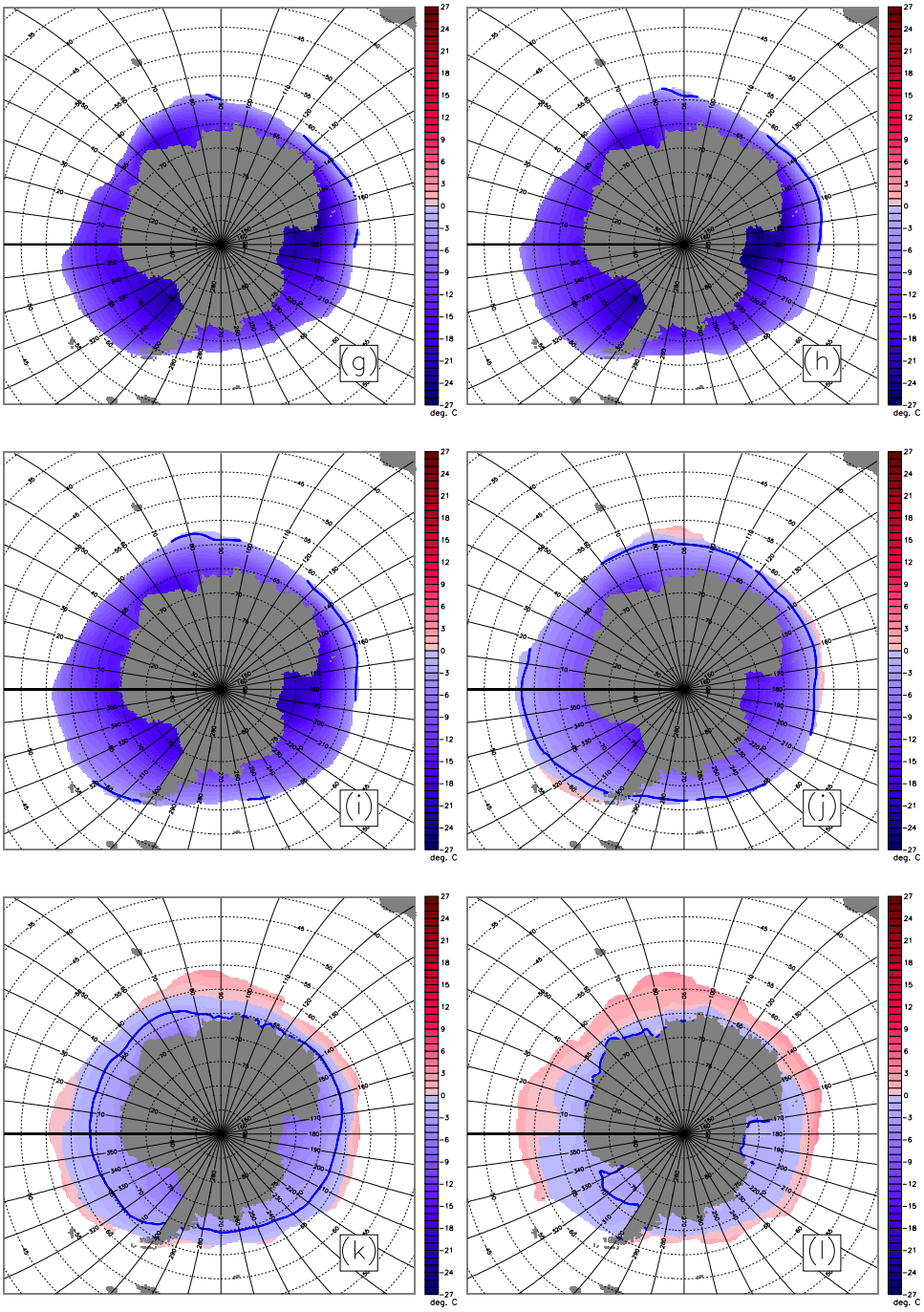

Figure D.1: Seasonal change of the 1998 to 2008 average air temperature in the sea ice zone: (g) July; (h) August; (i) September; (j) October; (k) November; (l) December.

E. Monthly Average Wind Speeds

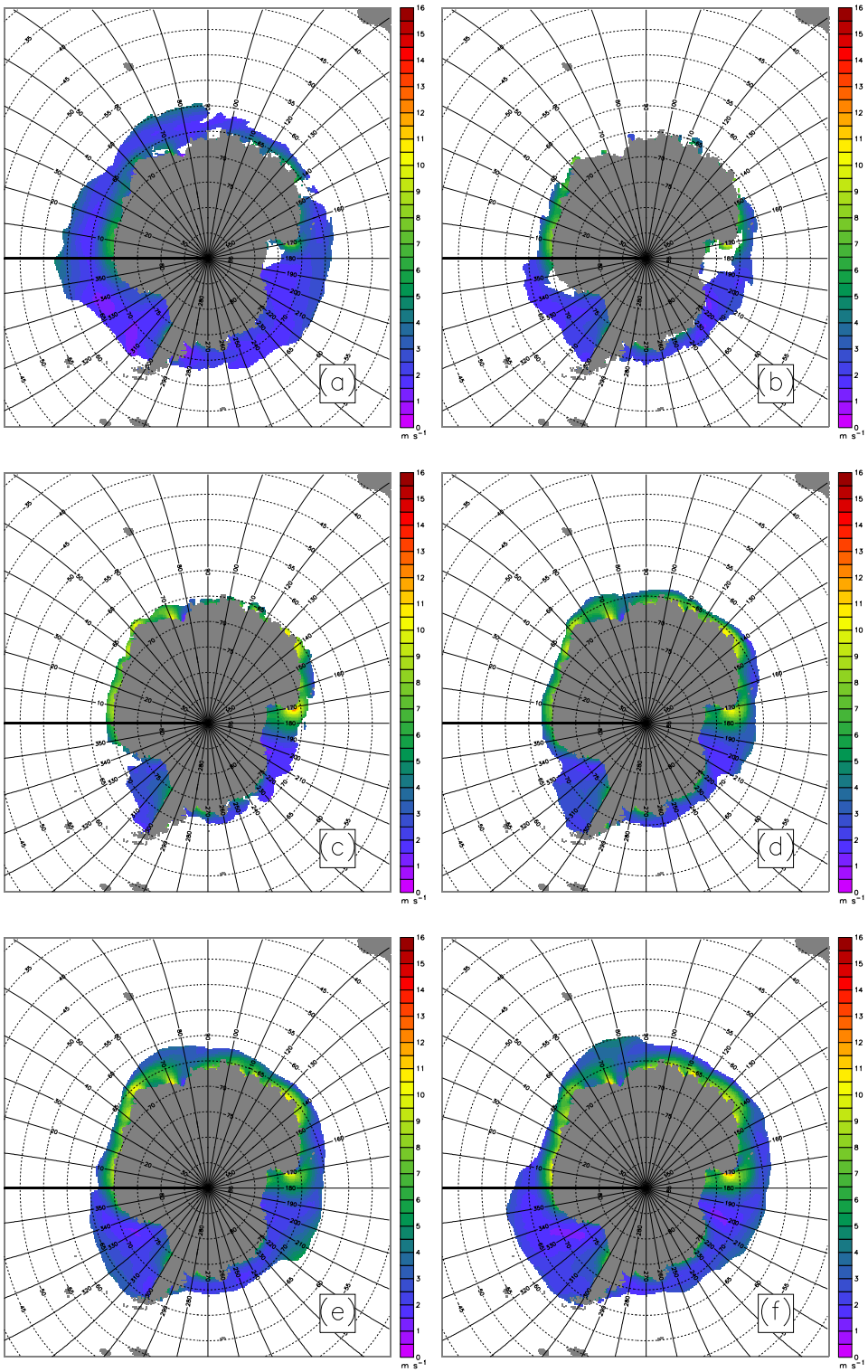

Figure E.1: Seasonal change of the 1998 to 2008 average wind speed in the sea ice zone: (a) January; (b) February; (c) March; (d) April; (e) May; (f) June.

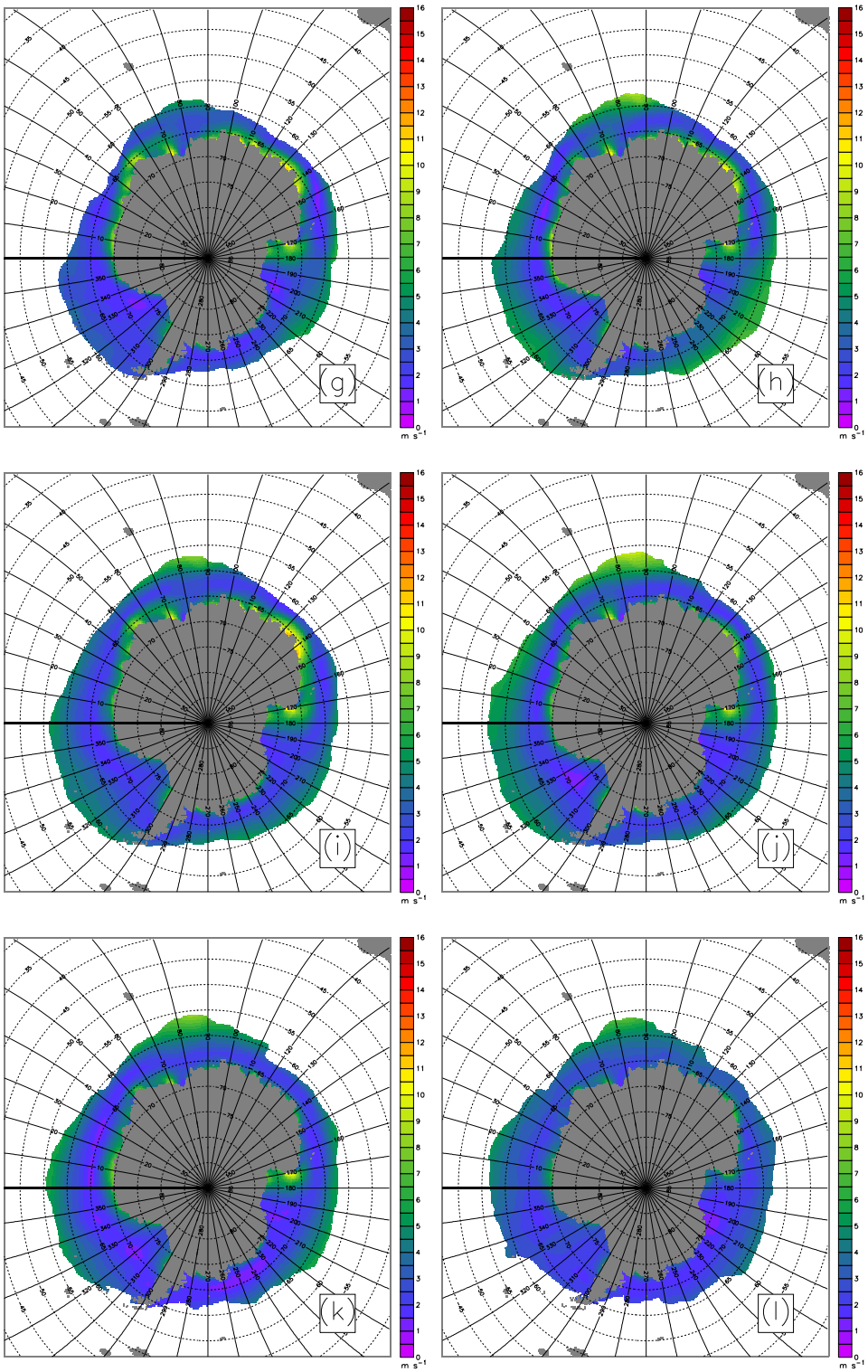

Figure E.1: Seasonal change of the 1998 to 2008 average wind speed in the sea ice zone: (g) July; (h) August; (i) September; (j) October; (k) November; (l) December.

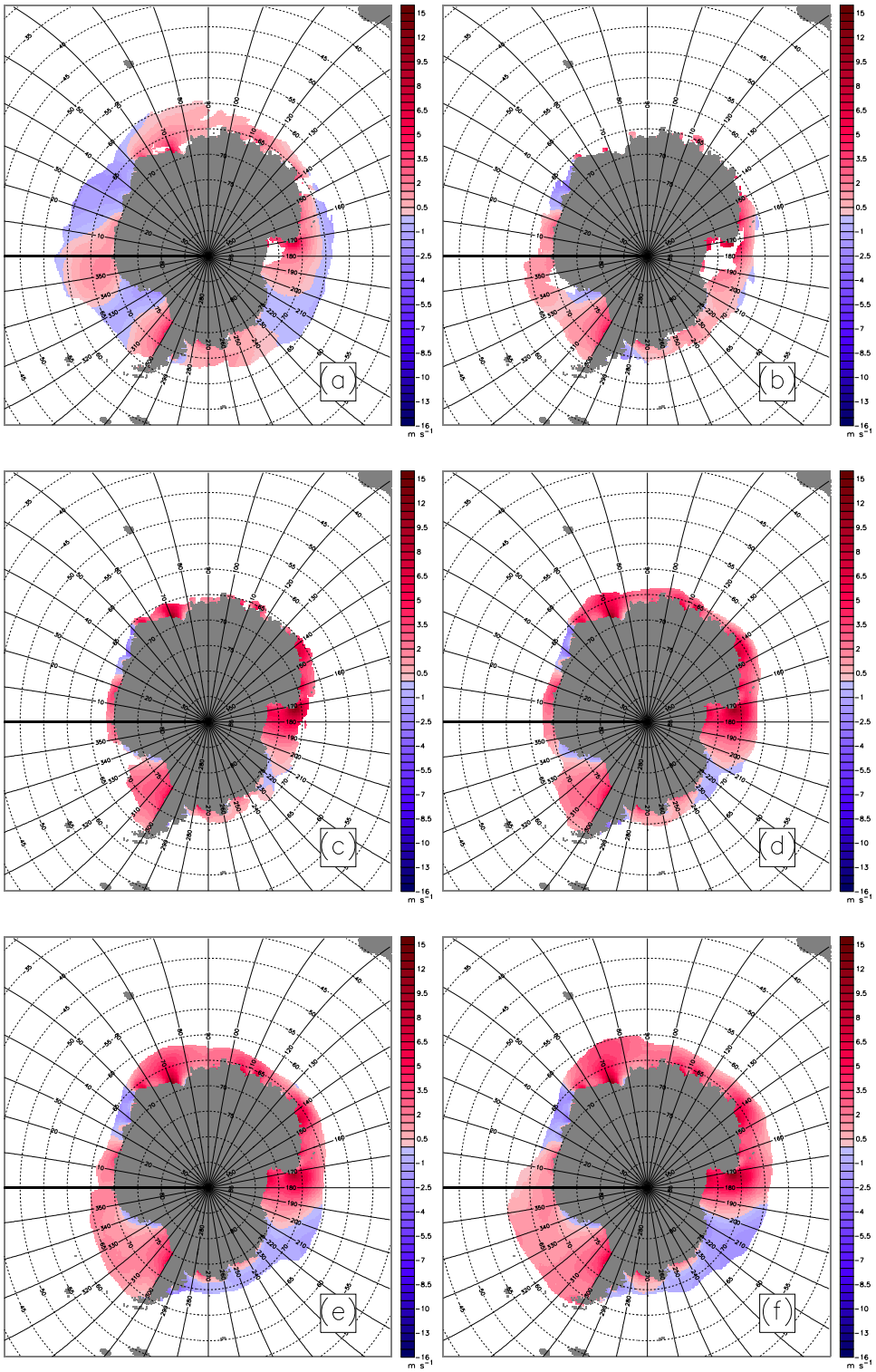

Figure E.2: Seasonal change of the 1998 to 2008 average southerly wind speed in the sea ice zone: (a) January; (b) February; (c) March; (d) April; (e) May; (f) June.

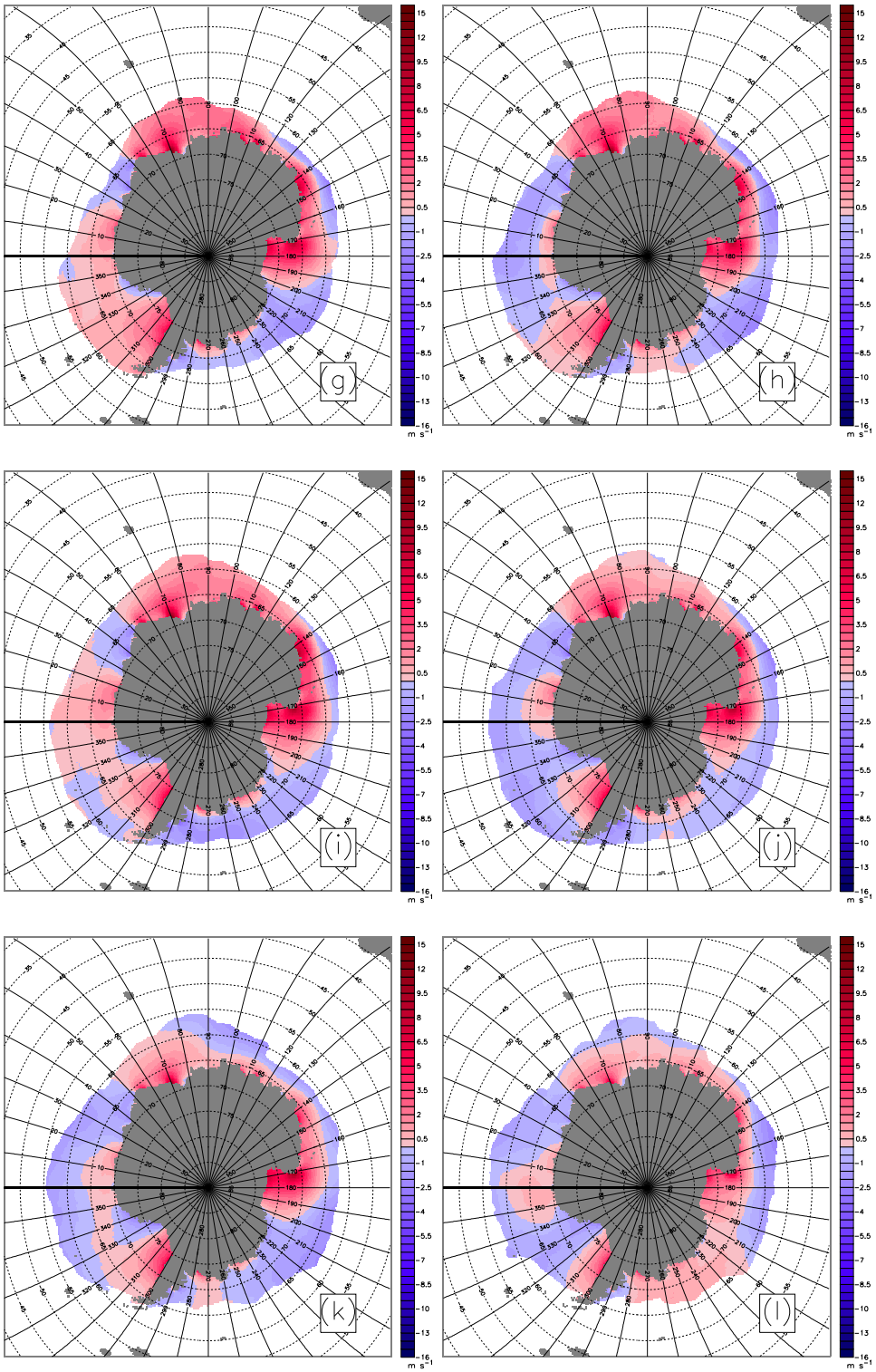

Figure E.2: Seasonal change of the 1998 to 2008 average southerly wind speed in the sea ice zone: (g) July; (h) August; (i) September; (j) October; (k) November; (l) December.

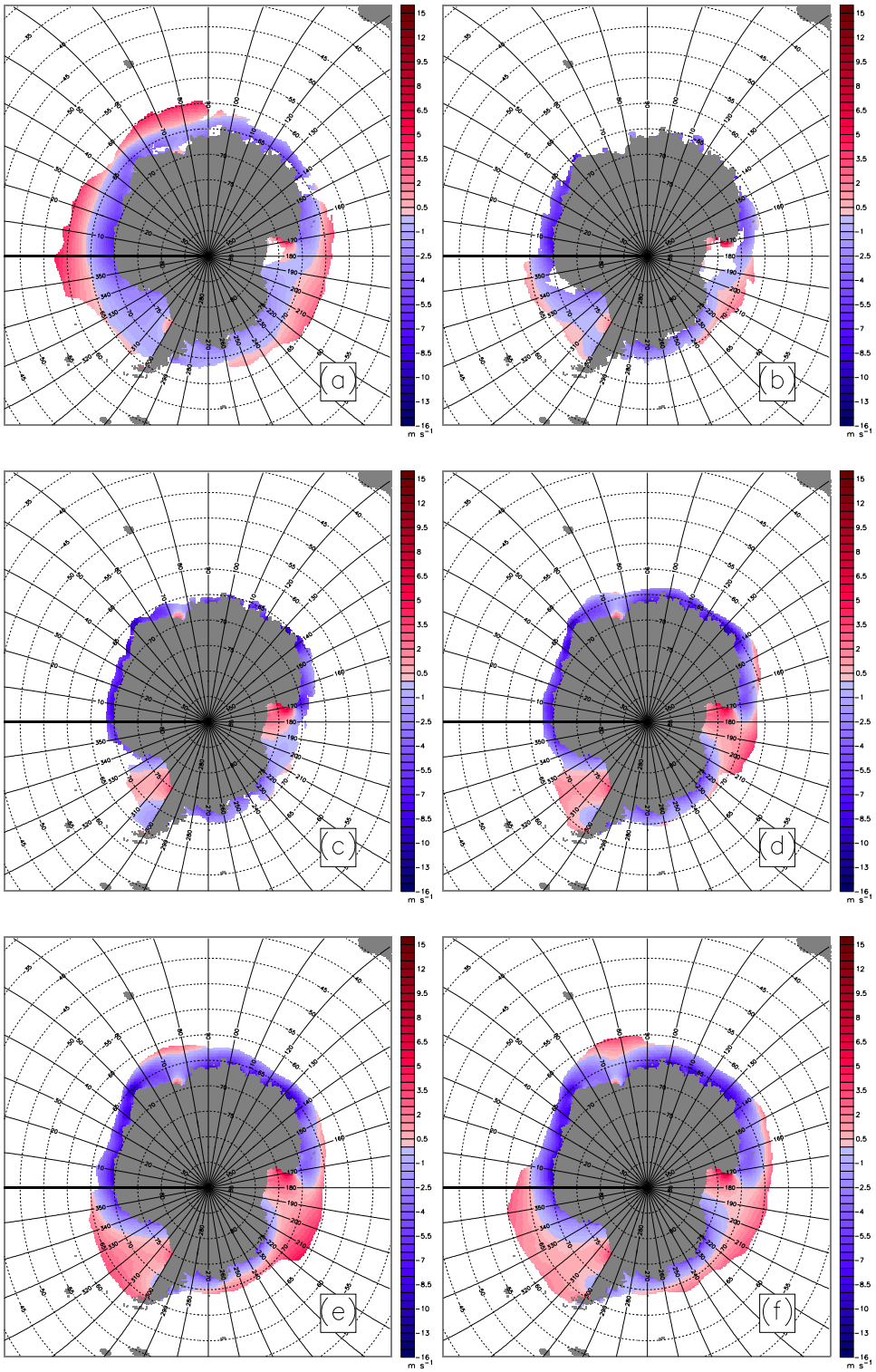

Figure E.3: Seasonal change of the 1998 to 2008 average westerly wind speed in the sea ice zone: (a) January; (b) February; (c) March; (d) April; (e) May; (f) June.

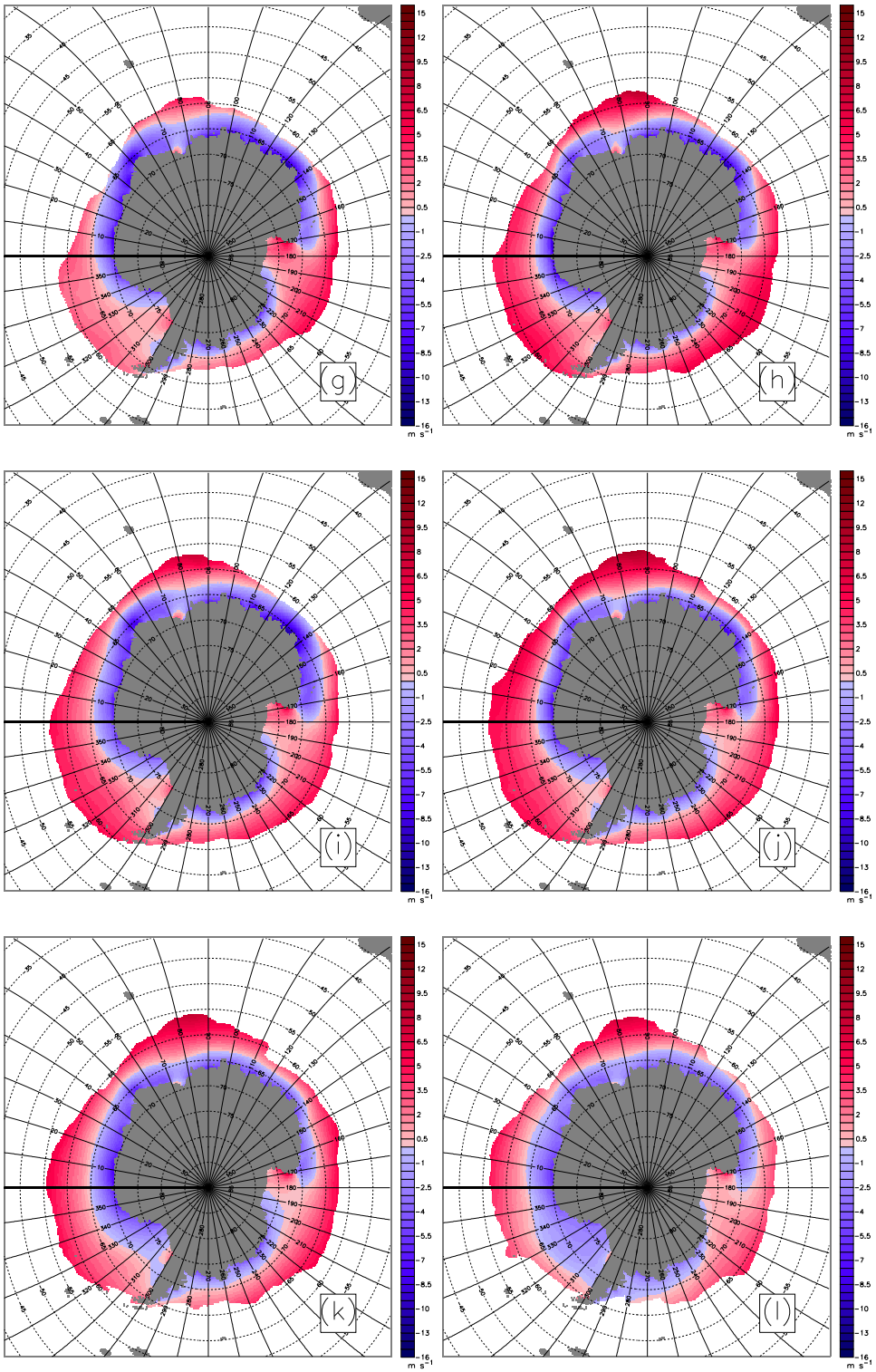

Figure E.3: Seasonal change of the 1998 to 2008 average westerly wind speed in the sea ice zone: (g) July; (h) August; (i) September; (j) October; (k) November; (l) December.